



UNIVERSIDADE FEDERAL DE SANTA CATARINA
CENTRO TECNOLÓGICO
PROGRAMA DE PÓS-GRADUAÇÃO EM ENGENHARIA MECÂNICA

Wagner de Barros Rupp Simioni

**Constitutive parameter identification based on non-homogeneous uniaxial
compression tests of PLGA**

Florianópolis
2019

Wagner de Barros Rupp Simioni

**Constitutive parameter identification based on non-homogeneous uniaxial
compression tests of PLGA**

Dissertação submetida ao Programa de Pós-Graduação em Engenharia Mecânica da Universidade Federal de Santa Catarina para a obtenção do título de mestre em engenharia mecânica.

Orientador: Prof. Eduardo Alberto Fancello, Dsc.

Coorientador: Paulo Bastos de Castro, Dr. Eng.

Ficha de identificação da obra elaborada pelo autor,
através do Programa de Geração Automática da Biblioteca Universitária da UFSC.

Simioni, Wagner de Barros Rupp
Constitutive parameter identification based on non
homogeneous uniaxial compression tests of PLGA / Wagner de
Barros Rupp Simioni ; orientador, Eduardo Alberto
Fancello, coorientador, Paulo Bastos de Castro, 2019.
113 p.

Dissertação (mestrado) - Universidade Federal de Santa
Catarina, Centro Tecnológico, Programa de Pós-Graduação em
Engenharia Mecânica, Florianópolis, 2019.

Inclui referências.

1. Engenharia Mecânica. 2. Identificação de parâmetros. 3.
Polímeros bioabsorvíveis. 4. Viscoplasticidade. 5. Ensaios
não homogêneos. I. Fancello, Eduardo Alberto. II. de
Castro, Paulo Bastos. III. Universidade Federal de Santa
Catarina. Programa de Pós-Graduação em Engenharia Mecânica.
IV. Título.

Wagner de Barros Rupp Simioni

**Constitutive parameter identification based on non-homogeneous uniaxial
compression tests of PLGA**

O presente trabalho em nível de mestrado foi avaliado e aprovado por banca examinadora composta pelos seguintes membros:

Prof. Miguel Vaz Júnior, Dr.
Universidade do Estado de Santa Catarina

Prof. Rafael Holdorf Lopez, Dr.
Universidade Federal de Santa Catarina

Certificamos que esta é a **versão original e final** do trabalho de conclusão que foi julgado adequado para obtenção do título de mestre em engenharia mecânica.

Prof. Jonny Carlos Da Silva, Dr.Eng.
Coordenador do Programa

Prof. Eduardo Alberto Fancello, Dsc.
Orientador:

Florianópolis, 8 de agosto de 2019.

À minha família.

AGRADECIMENTOS

Gostaria de agradecer ao meu orientador Prof. Dsc. Eduardo Alberto Fancello e coorientador Dr.Eng. Paulo Bastos de Castro pela orientação e valorosas contribuições à minha formação profissional e pessoal.

Agradeço também aos professores membros da banca por aceitarem participar da avaliação deste trabalho e por suas engrandecedoras contribuições e sugestões.

Agradeço aos colegas de laboratório do Grupo de Análise e Projeto Mecânico (GRANTE) pela amizade, pelas discussões e os momentos compartilhados ao longo dos últimos anos. Foram fundamentais para a elaboração e conclusão deste trabalho.

Sou grato especialmente à minha mãe Rita e aos meus irmãos Marcelo e Laís pelo suporte e apoio incondicional.

Por fim, agradeço ao Conselho Nacional de Desenvolvimento Científico e Tecnológico (CNPq) pelo suporte financeiro concedido por meio de bolsa de estudos.

*"With four parameters I can fit an elephant,
and with five I can make him wiggle his trunk!"
John von Neumann*

RESUMO

Materiais poliméricos bioabsorvíveis possuem propriedades físico-químicas atrativas para serem empregados em aplicações médicas. Desta forma, a proposição de modelos constitutivos capazes de reproduzir o comportamento mecânico desses materiais, bem como a caracterização de propriedades e parâmetros constitutivos tornam-se essenciais no projeto de componentes mecânicos e implantes seguros. A identificação de parâmetros constitutivos, por sua vez, permite compatibilizar resultados de ensaios laboratoriais e modelos computacionais à realidade observada nas mais diversas condições de aplicação de um produto. Em geral, testes são projetados para que propriedades intrínsecas do material sejam facilmente extraídas, idealmente sem dependência da geometria do corpo de prova, contudo isso nem sempre é viável. Por exemplo, sob condições usuais, testes de compressão do polímero bioabsorvível PLGA 85:15 apresentam instabilidades que tornam o processo de caracterização irreprodutíveis. Uma alternativa para se obter resultados consistentes desse material sobre compressão é através da realização de testes de compressão não homogêneos, com a presença de barrilamento. Isso, porém, impacta no processo de identificação de parâmetros, elevando significativamente a complexidade de ferramentas computacionais necessárias e o tempo necessário para o processo. Dentro desse contexto, este trabalho apresenta procedimentos para identificação de parâmetros constitutivos considerando ensaios de compressão não-homogêneos do material PLGA 85:15. Esse trabalho se propõe a analisar os procedimentos, visando uma identificação mais eficiente, e apresentar os parâmetros identificados. São considerados quatro procedimentos de identificação baseados em otimização. Os procedimentos fazem uso de algoritmos de otimização heurísticos (Particle Swarm - Nelder-Mead optimization) com hibridização global-local. Em cada procedimento é variado o grau de fidelidade ao experimento, considerando desde simulações numéricas de alta fidelidade utilizando o método de elementos finitos até simulações simplificadas, sem barrilamento, porém de computo mais rápido. Dois modelos constitutivos desenvolvidos anteriormente pelo grupo foram empregados, sendo esses modelos adequados a representação do comportamento elasto-viscoplástico e viscoelástico de materiais poliméricos. Uma análise comparativa entre as propostas é realizada em termos de adequação aos resultados experimentais e ao tempo requerido para realização do procedimento de identificação. Os modelos constitutivos foram capazes de representar o comportamento do material com sucesso. Todos os procedimentos realizados apresentaram respostas semelhantes, porém não idênticas e é observada uma diferença significativa entre procedimentos no tempo requerido para executá-los. Desta forma, o presente trabalho apresenta vantagens e desvantagens de cada método, auxiliando na escolha entre procedimentos.

Palavras-chave: Identificação de parâmetros, polímeros bioabsorvíveis, ensaios não homogêneos, otimização de parâmetros, viscoelasticidade, viscoplasticidade.

RESUMO EXPANDIDO

INTRODUÇÃO

Degradação de materiais e perda de propriedade mecânica são fenômenos usualmente indesejáveis para a maioria das aplicações. Tais fenômenos, no entanto, podem ser vantajosos em implantes. A degradação de materiais poliméricos bioabsorvíveis em substâncias que podem ser metabolizadas por um indivíduo reduzem a necessidade de procedimentos cirúrgicos para remoção do implante. Além disso, a perda de propriedades mecânicas permite uma gradual transferência de carga do implante para tecidos vivos regenerados, se controlada. O polímero poli(ácido lático-co-ácido glicólico) (PLGA) é um polímero biocompatível e bioabsorvível com taxa de degradação ajustável dependendo da razão entre seus copolímeros constituintes e dos esforços mecânicos à que o material é submetido. Testes laboratoriais realizados mostram que, sob compressão não-homogênea, o PLGA mostra um comportamento sensível à taxa de deformação e apresenta amolecimento e encruamento do material dependendo do nível de deformação. No campo de modelagem constitutiva para o PLGA, dois modelos foram considerados promissores para a reprodução do comportamento mecânico complexo desse material: os modelos de Castro (2017) e Farias (2018). Visando um posterior uso destes modelos para a simulação numérica do PLGA, o presente trabalho se dedica ao estudo da identificação de parâmetros constitutivos para os modelos apresentados considerando as complexidades trazidas por testes de compressão não-homogênea.

OBJETIVOS

O objetivo geral desta dissertação é criar uma estrutura de identificação de parâmetros para os modelos de Castro (2017) e Farias (2018) e prover parâmetros constitutivos com base em resultados experimentais já disponíveis na literatura. De forma a concluir o objetivo geral foram traçados os seguintes objetivos específicos:

- Implementar um algoritmo de processamento de imagem para obtenção do perfil radial dos corpos de prova ao longo dos testes, considerando a estrutura de Extensometria Radial por Vídeo (POULAIN; KOHLMAN, et al., 2013).
- Implementar e comparar diferentes procedimentos de identificação de parâmetros constitutivos para testes de compressão não-homogênea.
- Prover e comparar os parâmetros obtidos por cada procedimento de identificação.
- Verificar a adequação dos modelos elasto-viscoplástico apresentado por Castro (2017) e viscoplástico apresentado por Farias (2018) em representar o comportamento mecânico do PLGA.
- Discutir as vantagens e desvantagens de cada estrutura de identificação.

METODOLOGIA

Primeiramente é apresentado uma fundamentação teórica sobre o comportamento mecânico de polímeros, evidenciando a sensibilidade desta classe de materiais à taxa de deformação e temperatura e a existência dos fenômenos de amolecimento e encruamento significativos para diversos polímeros. Na sequência é apresentado o desenvolvimento matemático referente aos modelos constitutivos. Ainda em relação à fundamentação teórica são apresentadas algumas

estruturas já existentes para a identificação de parâmetros em ensaios não-homogêneos, onde o método híbrido de otimização por enxame de partículas e o algoritmo de nelder-mead se destacam. Com base em observações dos resultados experimentais foram elencadas hipóteses em relação ao nível das não-homogeneidades presentes no corpo de prova e quatro métodos de identificação foram elaborados e testados. Todos os métodos tem como meio um procedimento de identificação através de métodos de minimização da distância entre curvas experimentais e simuladas. O primeiro método assume uma baixa significância das não-homogeneidades, realizando o chamado procedimento constitutivo de identificação. O segundo método assume que as não-homogeneidades são significativas e a identificação deve fazer uso de métodos computacionalmente mais caros, baseados no método dos elementos finitos. Os dois métodos restantes são métodos híbridos, propostos de forma a reduzir o tempo de processamento para identificação de parâmetros, e ainda prover parâmetros adequados para a aplicação. Os quatro métodos foram testados tanto para o modelo de Castro (2017) quanto para o modelo de Farias (2018).

RESULTADOS E DISCUSSÃO

Em relação aos dados experimentais, é possível perceber que o comportamento mecânico do PLGA sob compressão difere de outros polímeros, apresentando um amolecimento acentuado e um encruamento suave posteriormente. Os modelos mostraram-se capazes de reproduzir os comportamentos de amolecimento e encruamento. O amolecimento acentuado, entretanto, apresenta um desafio para a modelagem constitutiva sendo susceptível a instabilidades numéricas. Para cada conjunto de parâmetros são mostrados os ajustes entre curvas experimentais e simuladas de força de compressão e de deslocamento transversal do corpo de prova para duas taxas de deformação. Todos os métodos de identificação mostraram-se adequados, com uma diferença significativa no tempo requerido para a identificação. Os parâmetros constitutivos são apresentados e discutidos.

CONSIDERAÇÕES FINAIS

A identificação de parâmetros considerando não-homogeneidades, como a presença de barrilamento no corpo de prova, é uma tarefa significativamente mais complexa do que para ensaios homogêneos. Verificou-se que é possível ainda realizar um procedimento de identificação próximo ao já realizado para ensaios homogêneos, com baixo impacto nos valores dos parâmetros identificados porém com uma redução significativa no tempo de processamento. A hibridização tanto dos algoritmos de otimização quanto dos procedimentos de identificação é considerada como benéfica para o problema tratado. Por fim, as dificuldades encontradas pela abordagens de identificação empregadas são discutidas e são elencadas proposições para trabalhos futuros.

Palavras-chave: Identificação de parâmetros, polímeros bioabsorvíveis, ensaios não homogêneos, otimização de parâmetros, viscoelasticidade, viscoplasticidade.

ABSTRACT

Bioresorbable polymer materials have attractive physicochemical properties, suitable for medical applications. In order to aid in the design process of safe mechanical components, it becomes necessary to characterize these materials and propose sophisticated constitutive models, capable of reproducing the material's mechanical behavior. The identification of constitutive parameters allows to compatibilize laboratory test results and computational models to the reality observed under the most diverse conditions of application of a product. In general, tests are designed so that intrinsic properties of the materials are easily extracted, ideally without dependence on the geometry of the test specimen, however this is not always feasible. For example, under usual conditions, compressive tests of the bioabsorbable polymer PLGA 85:15 exhibit instabilities that make the test results irreproducible. An alternative to obtain consistent results of this material upon compression is through non-homogeneous compression tests, with the presence of barrelling. This, however, impacts on the parameter identification process by significantly increasing the complexity of the computational tools needed and the time required for the process. Considering this context, this work presents procedures for identification of constitutive parameters considering non-homogeneous compression tests of PLGA 85:15. This work proposes to analyze identification procedures, aiming at a more efficient identification, and to present the identified parameters. Four identification procedures based on optimization are considered. The procedures make use of heuristic optimization algorithms (Particle Swarm - Nelder-Mead optimization) with global-local hybridization. In each procedure the degree of fidelity to the experiment is varied, considering from high fidelity numerical simulations, using the finite element method, to simplified simulations, but with faster computation time. Two constitutive models previously developed by the group were employed, these models are considered adequate to represent the elasto-viscoplastic and viscoelastic behavior of polymeric materials. A comparative analysis between proposals is carried out in terms of adequacy to the experimental results and to the time required to carry out the identification procedure. The constitutive models were able to represent the behavior of the material successfully. All procedures presented similar but non-identical responses and a significant difference in time required to execute the procedure is observed between them. In this way, the present work presents advantages and disadvantages of each method, aiding in the choice between procedures.

Key words: Parameter identification. Bioresorbable polymers. Non-homogeneous compression. Optimization.

LIST OF FIGURES

Figure 1 – Various stress-strain curves of commonly used polymers. Adapted from (GSELL et al., 1992).	32
Figure 2 – Representation of a stress-strain curve with key polymeric behaviors	32
Figure 3 – Compression Tests of PMMA at (a) 100 °C and (b) 25 °C. Adapted from Ames et al. (2009)	33
Figure 4 – Distinct softening behavior for PMMA, PC and PS - Adapted from (MELICK; GOVAERT; MEIJER, 2003b)	34
Figure 5 – PLLA based screws, rods and plates for medical applications. Poly(lactic acid): Synthesis, Structures, Properties, Processing, and Applications , reprinted with permission from John Wiley and Sons.	36
Figure 6 – Test layout	48
Figure 7 – Example of strain localization usually found in lubricated compression tests.	49
Figure 8 – Stages of the test specimen along the compression test - formation of barreling.	49
Figure 9 – Edge detection tool. (a) base image and (b) detected edges. The red markers track the diameter.	50
Figure 10 – Axial displacement measured by testing machine (MTS), LVDT and video. TS 09 - Slow strain rate.	52
Figure 11 – Axial displacement measured by testing machine (MTS), LVDT and video. TS 06 - Medium strain rate.	52
Figure 12 – Axial displacement measured by testing machine (MTS), LVDT and video. TS 01 - Fast strain rate.	53
Figure 13 – Image processing: markers (in red) and the lateral shape approximated by a quadratic function (in blue).	53
Figure 14 – Compressive force along the test. $\dot{\epsilon} = 1.0 \times 10^{-4} \text{ s}^{-1}$	54
Figure 15 – Compressive force along the test. $\dot{\epsilon} = 1.0 \times 10^{-3} \text{ s}^{-1}$	54
Figure 16 – Compressive force along the test. $\dot{\epsilon} = 1.0 \times 10^{-2} \text{ s}^{-1}$	55
Figure 17 – Mean compressive force for each strain rate in terms of displacement. . . .	55
Figure 18 – Transversal displacements at each marker.	57
Figure 19 – Transversal displacements at each marker.	57
Figure 20 – Transversal displacements at each marker.	58
Figure 21 – Volumetric ratio.	58
Figure 22 – Schematic representation of objective function evaluation	63
Figure 23 – Non-homogeneous compression - Finite Element Analysis.	64
Figure 24 – Homogeneous compression - Constitutive Model Analysis.	65
Figure 24 – Schematics the identification identification procedures.	67
Figure 25 – Calibrated FSF model for PMMA and PETg compression tests.	72

Figure 26 – Calibrated CF model for PMMA and PETg compression tests.	73
Figure 27 – FEM-based identification procedure - de Castro-Fancello model.	76
Figure 28 – Constitutive-based identification procedure - de Castro-Fancello model.	77
Figure 29 – Mixed-1 identification procedure - de Castro-Fancello model.	78
Figure 30 – Mixed-2 identification procedure - de Castro-Fancello model.	79
Figure 31 – FEM-based identification procedure - Farias model.	81
Figure 32 – Constitutive-based identification procedure - Farias model.	82
Figure 33 – Mixed-1 identification procedure - Farias model.	83
Figure 34 – Mixed-2 identification procedure - Farias model.	84
Figure 35 – FEM-based identification procedure - de Castro-Fancello model.	89
Figure 36 – Constitutive-based identification procedure - de Castro-Fancello model.	91
Figure 37 – Mixed-1 identification procedure - de Castro-Fancello model.	93
Figure 38 – Mixed-2 identification procedure - de Castro-Fancello model.	95
Figure 39 – FEM-based identification procedure - Farias model.	97
Figure 40 – Constitutive-based identification procedure - Farias model.	99
Figure 41 – Mixed-1 identification procedure - Farias model.	101
Figure 42 – Mixed-2 identification procedure - Farias model.	103

LIST OF TABLES

Table 3 – Approximate resorption times of commercially available lactide and glycolid homopolymers and copolymers. Adapted from Avgoustakis (2005).	36
Table 4 – Elastic constants for each strain rate	59
Table 5 – PSO variable limits for the de CF model.	68
Table 6 – PSO variable limits for the FSF model.	68
Table 7 – Identified parameters for PMMA and PETg for the FSF model	71
Table 8 – Identified parameters for PMMA and PETg for the CF model	71
Table 9 – Identified parameters for PLGA for the CF model	85
Table 10 – Identified parameters for PLGA for the FSF model	85
Table 11 – Time for each identification process (seconds)	86
Table 12 – Time for each identification process (seconds)	86

LIST OF ACRONYMS

ANVISA	Agência Nacional de Vigilância Sanitária
CFM	de Castro and Fancello model
DIC	Digital Image Correlation
FDA	Food and Drug Administration
FEM	Finite Element Method
FEA	Finite Element Analysis
FSFM	Farias, Stainier and Fancello model
GA	Glycolic acid
LA	Lactic acid
LEBm	Laboratório de Engenharia Biomecânica
LVDT	Linear Variable Differential Transformer
NM	Nelder-Mead method
PC	Polycarbonate
PE	Polyethylene
PEEK	Poly(ether ether ketone)
PGA	poly(glycolic acid)
PLA	poly(lactic acid)
PLGA	poly(lactic-co-glycolic acid)
PMMA	Poly(methyl methacrylate)
PP	Polypropylene
PS	Polystyrene
PSO	Particle Swarm Optimization
PTFE	Poly(tetra fluorethylene)
PVC	Polyvinyl chloride
VRE	Video-based Radial Extensometry
VSE	Video-based Surface Extensometry

LIST OF SYMBOLS

Scalars

- α Accumulated plastic strain
 t time
 \mathcal{W} Energy potential
 $\overline{\mathcal{W}}$ Effective energy potential
 W Helmholtz free energy potential
 ϕ^* Dissipative potential
 E Elastic modulus
 μ Shear modulus
 K Bulk modulus
 ν Poisson ratio
 T_g Glass transition temperature

Sets and vectors

- \mathcal{E} Set of state variables
 Z Set of internal variables
 \mathbf{x} Set of constitutive parameters

Tensors

- \mathbf{C} right Cauchy-Green stretch tensor
 \mathbf{F} deformation gradient tensor
 \mathbf{F}^e deformation gradient tensor - Elastic part
 \mathbf{F}^p deformation gradient tensor - Plastic part
 \mathbf{D}^p velocity gradient tensor- Plastic part
 \mathbf{M} velocity gradient tensor direction
 ϵ logarithmic strain tensor
 \mathbf{N} velocity gradient tensor direction
 \mathbf{P} First Piola-Kirchhoff stress tensor
 \mathbf{S} Second Piola-Kirchhoff stress tensor
 σ Cauchy stress tensor

de Castro-Fancello model related scalars

- W^e Isochoric-elastic energy potential
 U^e volumetric-elastic energy potential
 W^p Isochoric-plastic energy potential
 ϕ_{vp}^* Dissipative potential - viscoplastic contribution
 ϕ_{dp}^* Dissipative potential - plastic damage contribution
 ϕ_{vh}^* Dissipative potential - hydrolytic damage contribution
 d^p plastic damage
 d^h hydrolytic damage

d	total damage
μ	Shear modulus - de Castro-Fancello model
K	Bulk modulus- de Castro-Fancello model
H	Isotropic hardening modulus - CF model
n	Isotropic hardening exponent - CF model
σ_{y0}	Initial stress yield - CF model
c	viscoelastic compatibility modulus - CF model
η	viscoelastic sensibility modulus - CF model
S_0	Plastic resistance function parameter 1
S_{cv}	Plastic resistance function parameter 2
S_b	Plastic resistance function parameter 3
S_z	Plastic resistance function parameter 4
S_g	Plastic resistance function parameter 5

Farias, Stainier and Fancello model related scalars

H	Hencky energy potential
U	volumetric energy potential
L	Gent energy potential
ϕ^*	Dissipative potential
G	Shear modulus - FSF model
K	Bulk modulus- FSF model
λ	Isotropic hardening modulus - FSF model
μ	Isotropic hardening exponent - FSF model
m	viscoelastic sensibility modulus - FSF model
S_0	Plastic resistance function parameter 1
S_{cv}	Plastic resistance function parameter 2
S_b	Plastic resistance function parameter 3
S_z	Plastic resistance function parameter 4
S_g	Plastic resistance function parameter 5

Algorithmic parameters

$\phi_{cognitive}$	PSO cognitive parameter
ϕ_{social}	PSO social parameter
I_n	PSO Inertia factor
p^{IB}	PSO particle individual best position
p^{GB}	PSO Global best position

CONTENTS

1	INTRODUCTION	27
1.1	OBJECTIVES	28
1.2	STRUCTURE OF THE DISSERTATION	29
2	THEORETICAL FRAMEWORK	31
2.1	POLYMERS	31
2.1.1	Mechanical behavior of polymers	31
2.1.2	PLGA	35
2.2	CONSTITUTIVE MODELS	37
2.2.1	de Castro and Fancello (2017) model	38
2.2.2	Farias, Stainier and Fancello (2019) model	41
2.3	PARAMETER IDENTIFICATION	42
2.3.1	Gradient-based and gradient-free methods	44
2.3.2	Particle Swarm Optimization	45
2.3.3	Nelder-Mead Method	46
3	EXPERIMENTAL DATA AND ANALYSIS METHODS	47
3.1	COMPRESSION TEST	47
3.1.1	Test specimen	47
3.1.2	Test settings	47
3.2	IMAGE PROCESSING	48
3.2.1	Post-processing	50
3.2.1.1	Profile and volume	51
3.3	EXPERIMENTAL RESULTS	51
3.3.1	Compressive force	51
3.3.2	Transversal Displacements	51
3.3.3	Volume change	56
3.3.4	Homogeneous range	56
3.3.5	Elastic constants	56
4	IDENTIFICATION PROCEDURES	61
4.1	OBJECTIVE FUNCTION	61
4.2	IDENTIFICATION PROCEDURES	62
4.2.1	FEM-based identification procedure	62
4.2.2	Constitutive-based identification procedure	62
4.2.3	Mixed-1 identification procedure	64
4.2.3.1	Mixed-2 identification procedure	64
4.2.4	Defining an initial search space	65
4.2.5	Sampling the search space	68
4.3	NUMERICAL SIMULATION	69

4.3.1	Algorithm	69
4.3.1.1	Handling simulation failure	69
4.3.2	Validation	70
5	IDENTIFICATION RESULTS	75
5.1	CF MODEL	75
5.2	FSF MODEL	80
5.3	COMPLEMENTARY RESULTS	87
5.4	CF MODEL	88
5.5	FSFM MODEL	96
5.6	DISCUSSION	104
6	CONCLUSION	107

1 INTRODUCTION

Polymers are present in everyday life, from industrial applications to the common household. Some polymeric materials are biocompatible, a characteristic that permits the usage of this class of materials on intra-corporeal medical devices. A subgroup of biocompatible materials, the bioresorbable polymers are potential substitutes to metallic and ceramic implants due to their degradation and metabolic characteristics, removing the necessity of a subsequent medical procedure to remove such implant. The gradual transference of loads from an implant to a regenerated living tissue could in fact lead to a better healing process. To design safe devices it becomes increasingly necessary to understand the material behavior of its constituents.

Polymers can have a wide range of thermo-mechanical properties depending on its monomers and processing conditions during the manufacturing process. They display an intricate macro-mechanical responses such as material hardening, softening and rate sensitivity. Material degradation and loss of mechanical properties is present in all materials, but this process could be an advantage to bioresorbable materials if controlled. The poly(lactic-co-glycolic acid) polymer (PLGA) is a biocompatible and bioresorbable polymer that degrades in contact with water in a process called hydrolysis, producing two substances: lactic acid and glycolic acid. These substances occur naturally in the body and can be metabolized with minimal systemic toxicity. The hydrolytic degradation rate can be tailored depending on the ratio of its copolymers and can be affected by mechanical loading. As a substance, PLGA has been approved by both the United States Food and Drug Administration (FDA) and the Brazilian Health Regulatory Agency (Anvisa) and is already employed as a drug delivery system, orthopedic plates and screws. A better comprehension of the mechanical behavior of this material could aid in the development of more precise and reliable applications.

To simulate the complex mechanical behavior presented by degradable polymers many authors have proposed sophisticated constitutive models. The works of Castro (2017), Fuck (2018) and Farias (2018) present constitutive modeling for glassy polymers which could be able to represent PLGA's mechanical response. As an initial step on characterization of this material, compression tests of PLGA were performed by de Castro (CASTRO; SALMORIA, et al., 2019), where a series of compressive tests under three different strain rates were performed. It was verified that a homogeneous compression test was difficult to perform with this material, reason for which controlled non-homogeneous compression test may provide more reproducible results.

Non-homogeneous testing adds another layer of complexity to extract intrinsic material behavior. In homogeneous testing it is straightforward to translate global responses of force and displacement to local responses of stress and strain. However, when homogeneity cannot be assumed, as it happens in necking for tensile tests and barreling for compressive tests, not all points of the test specimen are in the same stress/strain state. This is troublesome to correctly identify parameters for the constitutive models.

The standard process in identification of the constitutive parameters involves experimental testing and curve fitting procedures so that the mathematical model reproduces experimental results. Curve fitting procedures can be performed through optimization, which means searching for a set of parameters that better reproduces experimental results through minimization of the error between experimental results and the numerical simulation of these results.

In the case of non-homogeneous tests, the curve fitting procedure will involve the simulation of this non-homogeneous stress/strain distribution, often utilizing simulations through the Finite Element Method (FEM). Non-homogeneous identification procedures have been performed to identify elasto-plastic parameters of low carbon steel (WANG et al., 2017) and viscoplastic parameters of PMMA (ABDEL-WAHAB; ATAYA; SILBERSCHMIDT, 2016), to name a few. Finite Element Analysis (FEA) can be time consuming and performing an iterative procedure as curve fitting using FEA could be prohibitively long. Poulain, Benzerga, and Goldberg (2014) performed parameter identification on epoxy resin EPON 826 subjected to barreling based on the mean axial stress of tests specimen, i.e. using a homogenized approach to the non-homogeneous field. Although the latter provides a simple identification procedure, it is not clear how much this affects on the final set of identified parameters.

The present work will focus on evaluating identification procedures and optimization frameworks for non-homogeneous compression tests based on experimental results of PLGA 85:15 provided by Castro (2017), refraining, at this stage, from mechanical and hydrolytic damage and thermal effects.

1.1 OBJECTIVES

The objective is to provide constitutive parameters using the existent test results and create an identification framework for future tests considering, for example, hydrolytic degradation effects. Considering the context stated earlier, the specific objectives of this work are:

- Implement an image processing algorithm to obtain the radial profile of the test specimens during the tests, considering the Video Radial Extensometry framework (POULAIN; KOHLMAN, et al., 2013).
- Implement and compare different identification procedures for non-homogeneous compressive tests.
- Provide and compare constitutive parameters for each identification procedure.
- Verify the suitability of the elasto-viscoplastic constitutive model presented by Castro (2017) and the viscoplastic constitutive model presented by Farias (2018) to represent the mechanical behavior of PLGA.
- Discuss the advantages and disadvantages of each identification framework.

1.2 STRUCTURE OF THE DISSERTATION

Chapter 2 presents the theoretical framework for this dissertation. First, the common macro-mechanical aspects of polymers are present and followed by an introduction to the specificities of PLGA. Secondly, two constitutive models for glassy polymers are presented, de Castro and Fancello model and the Farias, Stanier and Fancello model. Lastly, the general idea of parameter identification through optimization algorithms is described. Two optimization algorithms are presented and their advantages and disadvantages are discussed.

For completion, in Chapter 3, the compression tests are briefly described. An image processing algorithm is presented and the methodology to process the acquired data is detailed. The result from the compression tests and the data obtained from the image processing algorithm are shown. This results are the basis for the identification procedures presentend in Chapter 4.

Chapter 4 is where the identification procedures are presented and detailed, showing key differences between approaches. The results of each approach are presented in Chapter 5 and discussed. Concluding remarks are presented in Chapter 6 and some propositions for future works are suggested.

2 THEORETICAL FRAMEWORK

2.1 POLYMERS

2.1.1 Mechanical behavior of polymers

Polymers are a class of materials characterized by the repetition of units, base constituents which through the process of polymerization form long chains. Polymers exhibit an intricate mechanical response. Their behavior is sensitive to the level of strain, strain rate, hydrostatic stress and temperature (ARRUDA; BOYCE; JAYACHANDRAN, 1995). These macromechanic material behaviors are influenced by chain mobility, which can be affected by the chemical affinity between chains, physical structure of the chain (linear or ramified) and organization of chains (amorphous or semi-crystalline).

Amorphous regions are characterized by a complete disorder in the polymeric network, while the crystalline region is marked by rigidly organized arrangement of the molecular structure and these two regions can be present simultaneously in a polymeric material. Amorphous regions are often associated with a freer mobility between chains and a more sparse configuration. Whereas the crystalline region is marked by an increased rigidity and a tightly packed matter. The index of crystallinity is a volumetric ratio between amorphous and crystalline regions. This index can be used qualitatively to predict some expected mechanical behavior of polymers such as density, stiffness and permeability.

Amorphous and crystalline regions also behave differently depending on the temperature level, presenting very distinct mechanical responses. The responses vary from a rubbery condition to ductile, to brittle. The transition from rubbery to ductile (and vice versa) is named glass transition, which is defined by the so-called glass transition temperature (T_g). This transition is associated to changes in the amorphous region and happens in a relatively narrow temperature range. For temperatures far below the T_g a brittle behavior is observed, with increasing temperatures there is a loss in stiffness and resistance of material, which behaves in a more ductile fashion. Over the T_g the polymer is rubbery, offering increasingly less resistance to strain.

From the macromechanical point of view, Gsell et al. (1992) performed a series of tensile tests on various polymers. The material samples were tested for large strains, above the necking point, and the true stress was assessed by video-controlling of the sample profile (see Figure 1). These tests were performed at 25°C, a temperature above the T_g for poly(tetra fluoroethylene) (PTFE), polyethylene (PE) and polypropylene (PP) and below the T_g for polyvinyl chloride (PVC), polycarbonate (PC), polyamide 6 (PA6) and poly(ether ether ketone) (PEEK). From these curves some key behaviors that polymers exhibit at varied degrees can be observed. With increasing strains there is the development of a linear region, followed by an increasingly nonlinear region after which the material yields. There is a subsequent loss in resistance capability, known as material softening. For larger strains hardening is observed. Figure 2 displays

a simplified schematic of these characteristics.

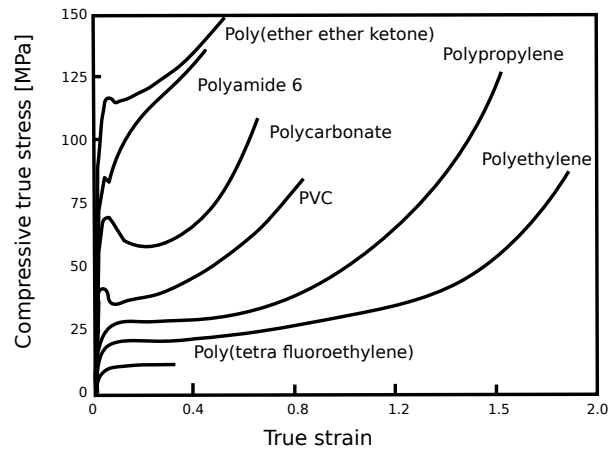


Figure 1 – Various stress-strain curves of commonly used polymers. Adapted from (GSELL et al., 1992).

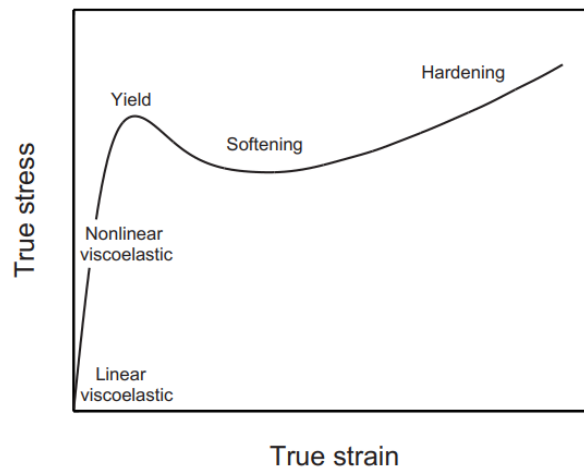
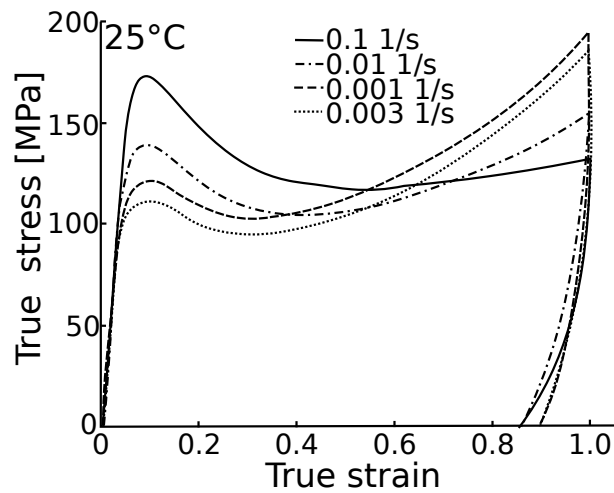


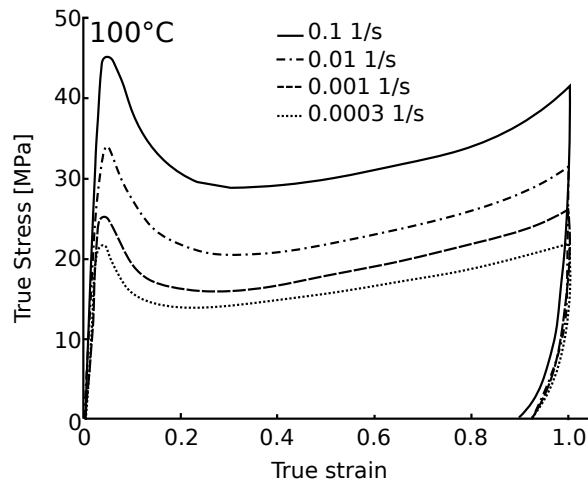
Figure 2 – Representation of a stress-strain curve with key polymeric behaviors

An overall decrease in stress can be expected with increase in temperature. In opposition, an increase in strain rate tends to increase peak stress, softening and hardening. Ames et al. (2009) analyzed the coupled thermo-mechanical effects in PMMA for a wide range of temperatures and strain rates. For low temperatures in comparison to T_g (here 115°C), the increase in strain rate could exhibit a decrease in rate of strain hardening (see Figure 3). This unexpected effect has been attributed by the authors to a near adiabatic heating induced at high strain rates. Arruda, Boyce, and Jayachandran (1995) verified temperature increase in the test specimens due to plastic work and observed that material softening had both strain as well as thermal softening contributions.

A series of studies on the origins and effects of polymer softening and hardening are available in the literature (MELICK; GOVAERT; RASS, et al., 2003)(MELICK; GOVAERT; MEIJER, 2003a)(MELICK; GOVAERT; MEIJER, 2003b). While the origins of hardening of



(a) 25°C



(b) 100°C

Figure 3 – Compression Tests of PMMA at (a) 100 °C and (b) 25 °C. Adapted from Ames et al. (2009)

polymeric materials can be linked to the increase of the polymeric network density (MELICK; GOVAERT; MEIJER, 2003b), the physical mechanisms that originate softening are not sufficiently comprehended. Yet, some studies were performed on how to increase or decrease softening and hardening levels. For example Melick, Govaert, and Meijer (2003a) studied the influence of thermo-mechanical history during manufacturing conditions on yield stress and the drop in resistance. Specimens that were annealed displayed a significant increase in peak stress and softening in comparison to quenched ones, while the hardening showed no difference between processes. Another study revealed that mechanical aging and rejuvenating time also altered the peak stress significantly: 48 hours aged PS showed an increase of 20 MPa in peak stress in tensile test in comparison to 10 min aging (MELICK; GOVAERT; RASS, et al., 2003).

Other relevant observation is that softening is often more noticeable under compression

than in tension. Significant strain localization is expected due to softening and contributes to initiation of crazing and shear banding (MELICK; GOVAERT; RASS, et al., 2003). In most polymers where softening is observed, it is common to observe 20% difference in strain from the stress peak to valley. A somewhat less common behavior is a substantial softening in a short strain range followed by modest hardening. Figure 4 shows the difference of compressive behavior between PMMA, PC and PS, where PS presents a much steeper softening than PMMA and PC. There are many material models for gradual softening and hardening in the literature, but none has been found applied to steep softening conditions as presented for PS.

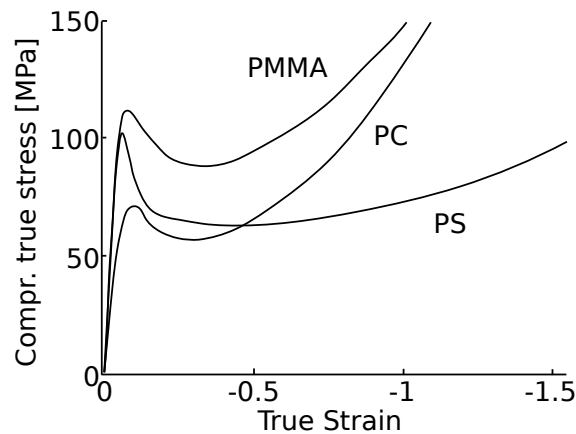


Figure 4 – Distinct softening behavior for PMMA, PC and PS - Adapted from (MELICK; GOVAERT; MEIJER, 2003b)

Since softening might induce strong localizations, non-homogeneous testing might be unavoidable. Non-homogeneous testing is complex since the response is not only the inherent material behavior, but a intricate relationship between material, specimen geometry and localization effects. These effects are not easily decoupled. How to assess non-homogeneity in tests is still today a subject of study, both from the measurement standpoint but from the identification viewpoint as well.

Poulain, Kohlman, et al. (2013) studied the determination of true stress using three different video-based extensometry methods: Video-based Surface Extensometry (VSE), Video-based Radial Extensometry (VRE) and Digital Image Correlation (DIC). The full strain field provided by DIC methodology was used as basis to compare the simpler methodologies of VRE and VSE. The former tracked markers in the gauge section and the latter tracked the radial profile of the specimen. Though DIC is a powerful tool for strain evaluation, for practical purposes of stress-strain measurements the VRE method displayed small differences to DIC even when strong localizations occur, whereas VSE delivers less accurate determination.

Jerabek, Major, and Lang (2010) tested PP samples to assess the small and large strain behavior under compression including barreling of cylindrical specimens along the test. Transversal strain were measured by video based extensometry as well. The authors studied methods for uniaxial compression tests including changes in specimen geometry and friction

reduction methods to reduce barreling. While the barreling decreased in some of the methods, asymmetries in the shape of the specimens appeared. The tests revealed that in the small strains regime the specimens displayed rather a homogeneous lateral deformation with significant loss in volume. Yielding was accompanied by differences in lateral strains along the specimens length, i.e., beginning of visible inhomogeneities.

From the viewpoint of constitutive modeling and parameter identification of polymeric materials, in Poulain, Benzerga, and Goldberg (2014) subsequent work, the authors used the VRE method to extract intrinsic material behavior of EPON 862 and calibrate a proposed elasto-viscoplastic model with these stress-strain curves. Another methodology used by researchers is to calibrate models using finite element simulation in order to reproduce the reaction forces measured by testing machines instead of transforming the measured force to local measurements of stress and strain, as it is usually done. Abdel-Wahab, Ataya, and Silberschmidt (2016) recreated uniaxial tensile tests and three-point bending tests in FE simulations and used optimization procedures to extract strain rate and temperature behavior of PMMA.

In this section, the class of polymeric materials has been briefly discussed from the mechanical behavior standpoint. In the next section, the focus is shifted to one member of this class, PLGA 85:15, and some of its idiosyncrasies that make this a promising material for medical applications.

2.1.2 PLGA

Polymeric degradation into biocompatible substances is of major interest for the design of medical implants and drug delivery systems. In these cases the degradation rate is important in order to ensure the effectiveness of these applications and guarantee, for example, that the drug will be delivered at the correct rate or the medical implant will not fail prematurely.

Lactic acid (LA) and glycolic acid (GA) are substances naturally present in the human body and can be metabolized by it. Through polymerization processes these substances can form poly(lactic acid) (PLA) and poly(glycolic acid) (PGA), polymers that in the presence of water degrade back into their constituent monomers through a process called hydrolysis.

Degradation can be accelerated by several factor including molecular weight, pH and mechanical loading (MILLER; WILLIAMS, 1984). The speed of degradation varies with crystallinity. Amorphous regions allow more permeability and contact between water and the material molecules than crystalline regions (ONG; YUN; WHITE, 2015). PGA is more hydrophilic than PLA because of its lower index of crystallinity thus degrading faster.

The degradation rate and mechanical properties can be, to an extent, tailored by polymerization of lactic acid and glycolic acid together, synthesizing the copolymer poly(lactico-glycolide) (PLGA). From the design point of view, PLGA might be preferred due to a superior control in the degradation properties by controlling the LA to GA ratio. Moreover, it can be processed more easily to a wider range of shapes and sizes and can encapsulate varied sizes of biomolecules (GENTILE et al., 2014). Approximate resorption times, as provided by

suppliers Boehringer Ingelheim and Alkermes, are displayed in Table 3.

Polymer	Biodegradation time (months)
L-PLA	>24
DL-PLA	12-16
PGA	6-12
DL-PLGA(85:15)	5-6
DL-PLGA(75:25)	4-5
DL-PLGA(50:50)	1-2
DL-PLGA(50:50)H	<1

Table 3 – Approximate resorption times of commercially available lactide and glycolid homopolymers and copolymers. Adapted from Avgoustakis (2005).

PLGA is a bioresorbable and biocompatible polymer, which means that PLGA, once degraded, it can be processed and removed by cellular activity without major toxicity, either local or systemic. PLGA is a FDA and ANVISA approved substance and is considered safe for intra-corporeal usage. Much of the research of PLGA is dedicated to its chemical properties and its ability to be a drug carrier substance. However, in the past decade, the material was considered a promising substitute for medical implants such as screws, suture anchors, craniofacial plates and stents. Examples of polymeric implants, in this case poly(lactic acid) or PLLA, can be seen in Figure 5. In these cases, it is critical to have a suitable strength to perform their biomechanical functions.



(a)

Figure 5 – PLLA based screws, rods and plates for medical applications. Poly(lactic acid): Synthesis, Structures, Properties, Processing, and Applications , reprinted with permission from John Wiley and Sons.

A series of tests in PLGA 85:15 craniofacial plates, injection-molded in different temperatures, was recently performed and reported by Melo et al. (2017). One of the results was the influence of the processing conditions on the T_g . The T_g varied from 52 to 56 °C, result which is corroborated by other authors. This implies that for clinical applications, i.e. at the

average human body temperature, the polymer is in the glassy state. The craniofacial plates were tested in 3-point bending tests in several stages of hydrolytic degradation. The plates remained 0, 15, 30, 60 and 120 days under aqueous solution after which the flexural stiffness and elongation at break were measured. Initially, the flexural stiffness ranged from 1.9 to 2.2 GPa and maintained similar values up to 15 days, after which a significant loss in stiffness takes place until structural collapse in 120 days. Crystallinity and molar mass fractions, which are dependent both due to chemical composition and processing conditions, were considered of major influence on degradation rate.

From the mechanical modeling standpoint, hydrolytic degradation coupled with mechanical loading has been assessed by Castro (2017) by enhancing a visco-plastic constitutive models to be sensible to hydrolytic damage. A similar procedure has been done by Fuck (2018) by employing hydrolytic damage to the visco-elastic model presented by Farias (2018). These models were deemed appropriate to reproduce the mechanical behavior of glassy polymers, including the characteristics softening and hardening behaviors. It is left to be observed how well suited they are to reproduce PLGA's response to mechanical loading, which is one of the main objectives of this dissertation. The available data on PLGA's response under compression does not include hydrolytic degradation and, for this reason, the undamaged form of the Castro (2017) model and Farias (2018) model were chosen for this task, on the expectancy that more data becomes available in the future. On the next Section these two models are briefly described.

2.2 CONSTITUTIVE MODELS

The variational constitutive updates framework provides a methodology to obtain the update of the thermodynamic state for a given process. This methodology is based on the works of Ortiz and Stainier (1999) and is the framework on which Farias (2018) and Castro (2017) fundament their models. The framework is briefly outlined in this section and the constitutive models presented afterwards.

Let \mathcal{E} be a set of independent state variables which fully describe a thermodynamic state. For a given purely kinematic process, \mathcal{E} can be described by a deformation gradient \mathbf{F} and a set of internal variables

$$\mathcal{E} = \{\mathbf{F}, Z\}. \quad (1)$$

The framework postulates the existence of an energy potential $\dot{\mathcal{W}}$ associated with the thermodynamic process comprised by the rate of the Helmholtz free energy potential \dot{W} and a dissipative potential ϕ^* , that is,

$$\dot{\mathcal{W}} = \dot{W}(\mathcal{E}) + \phi^*(\mathcal{E}), \quad (2)$$

and that the evolution laws of internal variables \dot{Z}^* from one state to the next can be recovered

via the minimization of this thermodynamic potential with respect to \dot{Z} ,

$$\dot{Z}^* = \arg \min_{\dot{Z}} \dot{W}. \quad (3)$$

For computational applicability, the potential \mathcal{W} and \dot{Z} are often approximated using an incremental (inc) form, i.e., in a discrete time interval from the instant n to $n + 1$. That is, given the set of independent state variables at the instant n , \mathcal{E}_n , the updated set of state variables at the next instant, \mathcal{E}_{n+1} can be solved by

$$\frac{Z_{n+1} - Z_n}{\Delta t} = \arg \min_{Z_{n+1}} \mathcal{W}_{inc}, \quad (4)$$

where

$$\mathcal{W}_{inc} = W(\mathcal{E}_{n+1}) - W(\mathcal{E}_n) + \Delta t \phi^*(\mathcal{E}_{n+1}) \quad (5)$$

The energy potential at the updated state is commonly known as the effective energy potential \bar{W} . Once the updated state \mathcal{E}_{n+1} is completely defined, the first Piola-Kirchhoff stress tensor can be calculated by the usual relationship

$$\mathbf{P}_{n+1} = \frac{\partial \bar{W}}{\partial \mathbf{F}_{n+1}} \quad (6)$$

2.2.1 de Castro and Fancello (2017) model

Following the variational framework previously presented, the model proposed in Castro and Fancello (2017), henceforth named CF model, considers the following set of state variables:

$$\mathcal{E} = \{\mathbf{F}, \mathbf{F}^p, \alpha, d^p, d^h\}, \quad (7)$$

where \mathbf{F} is the deformation tensor, \mathbf{F}^p is the plastic deformation tensor (considering the multiplicative decomposition $\mathbf{F} = \mathbf{F}^e \mathbf{F}^p$), α is a scalar internal variable associated with the accumulated plastic strain. The internal variables d^p and d^h have a scalar nature and are associated with the ductile damage and the hydrolytic degradation, respectively.

The incremental form of Helmholtz free energy potential W is chosen to have the contributions of an isochoric-elastic potential W^e , a volumetric-elastic potential U^e and an isochoric-plastic potential W^p , all of them being linearly related to the total damage $d = d^h + d^p$:

$$W = (1 - d)[W^e + U^e + W^p], \quad (8)$$

and

$$W^e = \mu \epsilon_{n+1}^e, \quad (9)$$

$$U^e = \frac{1}{2} K (\ln J)^2, \quad (10)$$

$$W^p = H \left[\frac{e^{n\alpha_{n+1}} - 1}{n} - \alpha_{n+1} \right]. \quad (11)$$

where ϵ_{n+1}^e is the elastic logarithmic strain tensor, $J = \det(\mathbf{C}_{n+1})$, and μ , H , K , n are constitutive parameters, namely, μ is the shear modulus, K is the bulk modulus, H is the isotropic hardening modulus and n is the isotropic hardening exponent.

The dissipative potential consists of the contribution of a visco-plastic dissipation function ϕ_{vp}^* , a dissipation function associated to the ductile damage ϕ_{dp}^* and another associated to the hydrolytic degradation ϕ_{dh}^* .

$$\phi^* = \phi_{vp}^* + \phi_{dp}^* + \phi_{dh}^* \quad (12)$$

The viscoplastic dissipation function is defined as

$$\phi_{vp}^* = (1 - d_{n+1})\sigma_Y \dot{\alpha} + \frac{c\mathcal{F}_A(\alpha_{n+1})}{\eta + 1} \left(\frac{\dot{\alpha}}{c}\right)^{\eta+1}, \quad (13)$$

where σ_Y is the initial yield stress and the $\mathcal{F}_A(\alpha)$ function is chosen to have the form:

$$\mathcal{F}_A(\alpha_{n+1}) = s_\infty + e^{-s_z \alpha_{n+1}} [(s_0 - s_\infty) \cosh(s_b \alpha_{n+1}) + s_g \sinh(s_b \alpha_{n+1})]. \quad (14)$$

This pseudo-potential is based on the Perzyna's model, including the $\mathcal{F}_A(\alpha)$ function known as plastic resistance function associated with hardening, softening and viscoplastic saturation of the material.

The ductile damage dissipation function is given by

$$\phi_{dp}^* = Y_{n+1} \dot{d}^p, \quad (15)$$

where Y is the thermodynamic force associated with damage,

$$Y = -\frac{\partial W}{\partial d} = -\frac{\partial W}{\partial d^p} = -\frac{\partial W}{\partial d^h} = W^e + U^e + W^p. \quad (16)$$

and, lastly, the hydrolytic degradation dissipation function is given by

$$\phi_{dh}^* = \frac{R}{2(1 - d_{n+\theta})(Y_{n+\gamma} + g)^{m-1}} (\dot{d}^h)^2 - g \dot{d}^h \quad (17)$$

where R , g and m are parameters related to the hydrolytic behavior. To compute these equations, some approximations and parametrizations are made. The time derivatives of the internal variables are approximated by:

$$\dot{\alpha} = \frac{\alpha_{n+1} - \alpha_n}{\Delta t}, \quad (18)$$

$$\dot{d}^h = \frac{d_{n+1}^h - d_n^h}{\Delta t}, \quad (19)$$

and

$$\dot{d}^p = \frac{d_{n+1}^p - d_n^p}{\Delta t}. \quad (20)$$

The evolution of the plastic damage \dot{d}^p is parametrized in terms of α and the thermodynamic force Y :

$$\dot{d}^p = \dot{\alpha} \frac{1}{N} Y^S \quad (21)$$

where S and N are ductile damage parameters.

\mathbf{F}^p can be calculated by means of the exponential mapping

$$\mathbf{F}_{n+1}^p = \exp(\Delta t \mathbf{D}_{n+1}^p) \quad (22)$$

and an important parametrization is made to the plastic velocity gradient, decomposing it into an amplitude $\dot{\alpha}$ and direction \mathbf{M} ,

$$\mathbf{D}^p = \dot{\alpha} \mathbf{M}_{n+1}. \quad (23)$$

Having defined the Helmholtz free energy potential and the dissipation potential, the effective incremental potential comes from the extremization process

$$\bar{\mathcal{W}} = \inf_{\dot{\alpha}, d^h, d^p} \mathcal{W}. \quad (24)$$

which implies in solving the residuals $r1$, $r2$ and $r3$ as given by the equations

$$r1 = \frac{\partial \mathcal{W}}{\partial \alpha_{n+1}} \quad (25)$$

$$r2 = \frac{\partial \mathcal{W}}{\partial d_{n+1}^h} \quad (26)$$

$$r3 = \frac{\partial \mathcal{W}}{\partial \mathbf{M}_{n+1}} \quad (27)$$

Equation (2.27) can be solved analytically resulting in the direction tensor \mathbf{M} as given by

$$\mathbf{M} = \sqrt{\frac{3}{2}} \frac{\ln \mathbf{C}_{n+1}^{pr}}{\|\ln \mathbf{C}_{n+1}^{pr}\|} \quad (28)$$

where \mathbf{C}_{n+1}^{pr} is a predictor for the isochoric right Cauchy-Green deformation tensor given by

$$\mathbf{C}_{n+1}^{pr} = (\mathbf{F}_n^{iso,p})^{-T} \mathbf{C}_{n+1}^{iso} \mathbf{F}_n^p \quad (29)$$

$$\mathbf{C}_{n+1}^{iso} = \mathbf{F}_{n+1}^{isoT} \mathbf{F}_{n+1}^{iso} \quad (30)$$

$$\mathbf{F}_{n+1}^{iso} = J_{n+1}^{-\frac{1}{3}} \mathbf{F}_{n+1} \quad (31)$$

The second Piola-Kirchhoff stress tensor \mathbf{S} can be then computed by:

$$\mathbf{S}_{n+1} = 2 \frac{\partial \bar{\mathcal{W}}}{\partial \mathbf{C}_{n+1}}, \quad (32)$$

or in terms of the Cauchy stress tensor :

$$\boldsymbol{\sigma}_{n+1} = J^{-1} \mathbf{F}_{n+1} \mathbf{S}_{n+1} \mathbf{F}_{n+1}^T. \quad (33)$$

In order to be completely defined, this model requires the identification of 17 material parameters. However, in this work, damage will be neglected, i.e., it is imposed that $d_{n+1}^h = d_{n+1}^p = d_{n+1} = 0$. Thus, the following set \mathbf{x} of 12 constitutive parameters should be identified:

$$\mathbf{x}_{CFM} = \{\mu, K, H, n, c, \eta, \sigma_{y0}, S0, Scv, Sb, Sz, Sg\}. \quad (34)$$

2.2.2 Farias, Stainier and Fancello (2019) model

Farias, Stainier, and Fancello (2019) model, henceforth named FSFM, considers the following set of state variables:

$$\mathcal{E} = \{\mathbf{F}, \mathbf{F}^p, \alpha\} \quad (35)$$

where \mathbf{F} is the deformation tensor, \mathbf{F}^p is the plastic deformation tensor (considering the multiplicative decomposition $\mathbf{F} = \mathbf{F}^e \mathbf{F}^p$), α is a scalar internal variable associated with the accumulated strain.

The incremental form of Helmholtz free energy potential W is chosen to have the contributions of an volumetric energy potential U , the Gent energy potential L related to polymeric chain locking, and an Hencky distortional energy potential H

$$H = G \|\boldsymbol{\epsilon}_{n+1}^e\|^2 \quad (36)$$

$$U = \frac{1}{2} K (\ln J)^2, \quad (37)$$

$$L = -\frac{\lambda \mu}{2} \ln \left[\frac{\lambda + 3 - \text{tr}(\mathbf{C}_{n+1}^{iso})}{\lambda} \right] \quad (38)$$

where G, K, λ and μ are material parameters, $\boldsymbol{\epsilon}_{n+1}^e$ is the elastic logarithmic strain tensor and $J = (\det(\mathbf{C}_{n+1}))^{\frac{1}{2}}$. The dissipative potential is chosen as

$$\phi^* = \frac{\mathcal{F}_A(\alpha_{n+1})}{m+1} (\dot{\alpha})^{m+1} \quad (39)$$

where $\mathcal{F}_A(\alpha_{n+1})$ function is chosen to have the form (FARIAS, 2018):

$$\mathcal{F}_A(\alpha_{n+1}) = s_\infty + e^{-s_z \alpha_{n+1}} [(s_0 - s_\infty) \cosh(s_b \alpha_{n+1}) + s_g \sinh(s_b \alpha_{n+1})]. \quad (40)$$

Notice that the undamaged form of the de Castro-Fancello model reduces to this form if $c = 1$, $\sigma_{y0} = 0$ and the equivalence of the parameter m in this model to η in the other.

The evolution of the accumulated plastic strain $\dot{\alpha}$ is approximated as

$$\dot{\alpha} = \frac{\alpha_{n+1} - \alpha_n}{\Delta t}, \quad (41)$$

and \mathbf{F}^p can be calculated by means of the exponential mapping

$$\mathbf{F}_{n+1}^p = \exp(\Delta t \mathbf{D}_{n+1}^p) \quad (42)$$

from which the plastic velocity gradient, decomposing it into an amplitude $\dot{\alpha}$ and direction \mathbf{N}

$$\mathbf{D}_{n+1}^p = \dot{\alpha} \mathbf{N}_{n+1}, \quad (43)$$

Once again, with both the Helmholtz free energy potential and the dissipation potential defined, the effective incremental potential comes from the extremization process

$$\overline{\mathcal{W}} = \inf_{\dot{\alpha}, \mathbf{N}} \mathcal{W}. \quad (44)$$

which implies in solving the residuals $r1$ and $r2$ as given by

$$r1 = \frac{\partial \mathcal{W}}{\partial \alpha_{n+1}} \quad (45)$$

$$r2 = \frac{\partial \mathcal{W}}{\partial \mathbf{N}_{n+1}} \quad (46)$$

Equation (2.44) can be solved analytically resulting in

$$\mathbf{N} = \frac{1}{\sqrt{2}} \frac{\text{dev} \boldsymbol{\epsilon}_{n+1}^{pr}}{\|\text{dev} \boldsymbol{\epsilon}_{n+1}^{pr}\|}, \quad (47)$$

where the predictor state is given by

$$\mathbf{F}_{n+1}^{pr} = \mathbf{F}_{n+1}^{iso} (\mathbf{F}_n^p)^{-1} \quad (48)$$

$$\mathbf{C}_{n+1}^{pr} = (\mathbf{F}_{n+1}^{pr})^T \mathbf{F}_{n+1}^{pr} \quad (49)$$

$$\boldsymbol{\epsilon}_{n+1}^{pr} = \frac{1}{2} \ln \mathbf{C}_{n+1}^{pr}. \quad (50)$$

The first Piola-Kirchhoff stress tensor \mathbf{P} can be then computed by:

$$\mathbf{P}_{n+1} = 2 \frac{\partial \bar{\mathcal{W}}}{\partial \mathbf{P}_{n+1}}, \quad (51)$$

or in terms of the Cauchy stress tensor :

$$\boldsymbol{\sigma}_{n+1} = J^{-1} \mathbf{P}_{n+1} \mathbf{F}_{n+1}^T. \quad (52)$$

In order to utilize this model, a total of 10 material parameters are necessary. The following set \mathbf{x}_{FSFM} of constitutive parameters are required to be identified:

$$\mathbf{x}_{\text{FSFM}} = \{G, K, \lambda, \mu, m, S0, Scv, Sb, Sz, Sg\}. \quad (53)$$

2.3 PARAMETER IDENTIFICATION

The usual problems solved in solid mechanics consists in finding a deformed configuration of a body given its undeformed configuration, material, applied loads and prescribed displacements. This category of problems constitutes what is known as forward problem, or the problem of predicting the effect given a cause. On the other hand, an inverse problem makes use of both cause and effect to infer models and parameters that characterize a system Tarantola (2005).

Inverse problems are ill-posed due to the fact that they often have multiple solutions, i.e., multiple models and combination of parameter values can provide the same output given the same input, meaning that any of these is a valid solution to the mathematical problem but might not reflect the one true physical solution. Some examples of inverse problems in mechanical engineering are the determination of undeformed geometries (shape inverse problem), determination of load history (process inverse problem) and identification of material

properties (constitutive parameter identification inverse problem). This work focuses on the latter.

Early strategies on constitutive parameter identification focuses on finding straight forward curve fitting techniques on phenomenological models. These techniques aim at fitting the material model to experimental response curves making use of geometric properties of the experimental curves such as calculating the slope to determine the elastic modulus for linear-elastic materials or defining the stress yield when it is a clearly defined point in a stress-strain curve. Straightforward procedures, often named calibration procedures, can be used even with more sophisticated non-linear material behavior. Anand and Ames (2006), for example, developed a calibration framework based on several hierarchical steps in order to identify material parameters for PMMA, including hardening and softening related parameters.

The proposition of calibration rules might be difficult to formulate for non-linear models with a high number of parameters or when these parameters are responsible for opposing behaviors. Another difficulty arise in the case of non-homogeneous testing. Each point of the test specimen might be subjected to different load conditions so the link between the measured macroscopic response and material parameter cannot be made directly. In light of this kind of drawback, optimization-based procedures arose as an viable solution to handle sophisticated material models in non-homogeneous testing. These elegant trial-and-error procedures are iterative processes which require simulating the material model in the test conditions (trial) to evaluate a fitness function (error).

To simulate non-homogeneous testing a Finite Element (FE) simulation is commonly used. FE simulations are computationally costly, which renders optimization strategies of non-homogeneous tests time consuming. In order to reduce computational time two main approaches are in development: reduction of simulation time (and the evaluation of the fitness function) and more efficient optimization algorithms.

One branch of research being developed is the usage of surrogate models to reduce the time spent on simulation. A reduced number of FE simulations is used to construct a surrogate model and perform the identification procedure based on that alternative. Li et al. (2016) developed an artificial neural networks model trained with FE simulations for reproducing nanoindentation load response curves and used the trained model in the fitting procedure. Surrogate models do not substitute high fidelity FE simulations as a whole, but can be used to reduce identification time significantly. In the literature searched, however, few comparative studies are present, making it difficult to quantify how much error is introduced when using a surrogate model in identification procedures.

Alternatively, computational time can also be reduced by the usage of more efficient optimization algorithms and procedures that would require fewer evaluations of a fitness function. Vaz Jr. et al. (2015) performed a series of tests including different optimization algorithms in order to provide more efficient parameter identification schemes exploring the advantages and disadvantages of gradient-based, gradient-free and hybrid optimization algorithms in the field

of parameter identification.

2.3.1 Gradient-based and gradient-free methods

Optimization algorithms are categorized in two major groups: gradient-based and gradient-free methods. The gradient-based methods require the derivatives of the objective and constraint functions to conduct the search process. In general these methods require a deep understanding of the mathematical formulation of the problem. If the problem is convex and the derivatives of the objective function are known a priori, or inexpensive to approximate, the usage of gradient-based methods is justified in terms of robustness, reliability and efficiency (ARORA, 2004).

On the other hand, gradient-free methods do not require knowledge of derivatives in the search procedure. Instead, these methods make use of heuristics, a set of rules which guides the iterative process, but with no mathematical proof they will find a solution. Many authors have made analogies to natural systems to come up with different heuristics to optimization algorithms: biology inspired algorithms such as Genetic Algorithm (HOLLAND, 1992) and Particle Swarm Optimization algorithm (EBERHART; KENNEDY, 1995)(KENNEDY; EBERHART, 1995), physics inspired algorithms like Simulated Annealing algorithm (KIRKPATRICK; GELATT JR; P. VECCHI, 1983)(ČERNÝ, 1985) and social cultured inspired such as the Cultural Algorithm (REYNOLDS, 1994). Regardless of the inspiration source and the analogy they use, these methods try to overcome common hindrances of gradient-based algorithms such as stopping at local minima, necessity of continuity and differentiability.

Some drawbacks of gradient-free algorithms are that there is no guarantee a global solution on a search space will be found and, in general, these methods require many more function evaluations than gradient-based methods to achieve a minimum. Performance results for various types of functions were tested and presented by Hansen et al. (2010). There is no consensus on which optimization algorithm is the best. Usually the fitness of algorithms are problem-specific and the choice of which to use depends on the user skill and experience on the expected behavior of the objective function topology.

Some other possibilities are based on hybrid approaches. Such approaches are procedures that use more than one optimization technique. A hybrid approach is usually designed to make use of the strengths of one technique or to reduce its shortcomings, for example, combine exploration abilities of global search methods with convergence rate of local methods. Zhou et al. (2015) distinguished hybridization of methods in three types: hybridization of different search methods, of search and updating methods and of different methods in different search phases. The first combines the methods by including one into the other. The second is that where the updating approach at each iteration is a combination of the techniques. The third one is when two methods are used in sequence, i.e. when one method converges, the other is started from that point on. In this work a hybrid scheme was employed using a Particle Swarm Optimization method (PSO) for global search and the Nelder-Mead method (NM) for local

search by following the procedure described by Vaz Jr. et al. (2015).

2.3.2 Particle Swarm Optimization

The Particle Swarm Optimization is an optimization procedure based on swarm intelligence: each individual searches for a resource independently and signals to the other members of the swarm how good its position is, i.e., the value of the fitness function. Each individual can roam in random directions, it has cognition, i.e. remembers the position they found best, as well as a social aspect of the swarm that is to be drawn to the best of the swarm.

Analogy aside, each individual is a particle that has a position p in the search space and displacement at each iteration, i.e., velocity (usually zero in the start of the process). At every iteration the objective function is calculated at the position of each individual. The best of all positions is recorded, as well as each individual best. At each iteration the particles are displaced to a new position, where the displacement vector is based on the combination of the social aspect (go to the best position of the swarm), the cognition aspect (go to the best position the particle found itself) and a random aspect to increase search variability. An inertia factor is also added, this add an contribution of the older path and reduces mobility slightly at each iteration and induces to a faster convergence of the swarm. Equation (54) shows the j -th component of the velocity vector of the i -th particle:

$$V_{(i,j)} = In \cdot V_{(i,j)} + r_c \cdot \phi_{cognitive} \cdot (p_{(i,j)}^{IB} - p_{(i,j)}) + r_s \cdot \phi_{social} \cdot (p_{(j)}^{GB} - p_{(i,j)}) \quad (54)$$

where p^{IB} is the individual best position, p^{GB} is the global best position, In is the inertia factor, $\phi_{cognitive}$ is the cognitive factor and ϕ_{social} the social factor being r_c and r_s random values from 0 to 1. These factors influence how fast it will converge to the global best or how much the individuals will keep exploring. Best values for In , $\phi_{cognitive}$ and ϕ_{social} , as well as the total number of individuals, seems to be problem specific, and this meta-optimization is beyond the scope of the present work. Thus, the chosen values were $In = 1.0$, $\phi_{cognitive} = \phi_{social} = 2.0$ and the stopping criteria was to be the condition when 95% of the particles were in the same region or when the improvement of the objective function was bellow 5% during 4 consecutive iterations.

One of the main advantages of the PSO is its exploration ability and how it allows escaping from local minima. This, however, requires a high enough number of individuals in order to find the global minimum of the search space, which means evaluating the objective function several times. In this case, the evaluation is time consuming since it requires the simulation of a mechanical system. Thus, a compromise must be made between augmenting the number of particles and the time requirement that it involves.

One less explored particularity of the PSO is that evaluating stage of the algorithm can be parallelized, instead of sequentially evaluating each particle. This reduces significantly the

computational time or allows widening the search space and still remain in an acceptable time frame. The implemented parallel procedure is described in latter sections.

2.3.3 Nelder-Mead Method

The Nelder-Mead method is a simplex-based, gradient-free, local-search optimization method, first described by Nelder and Mead (1965). A $n_d + 1$ dimensional simplex (where n_d is the number of variables to be identified) is positioned in the search space. The position in the search of each vertex is evaluated and the worst of them is selected to move its position.

Four possible movement are available: reflection, expansion, external contraction and internal contraction. The centroid of all but the worst-valued vertex is calculated. The worst vertex is reflected in relation to this centroid and the objective function evaluated (reflection). If that movement represents an improvement the vertex is moved in that direction (expansion), otherwise it will contract towards the centroid (external contraction). If none of these movements improve the position, the reflection is discarded and the vertex is moved towards the centroid (internal contraction). Lastly, if none of these operations work then the simplex is shrunk towards the best-valued vertex and a new iteration starts. The adopted convergence criteria is when the simplex shrinks its size tenfold.

3 EXPERIMENTAL DATA AND ANALYSIS METHODS

3.1 COMPRESSION TEST

In this section the process of data acquisition is briefly described. The design and execution of the tests were made by Paulo Bastos de Castro and Bruna Nunes Correa at GRANTE and LEBm. At the time of writing, their work is currently under publishing procedures, where an in-depth description of the experimental procedure will be available at (CASTRO; SALMORIA, et al., 2019). The main contribution of the current work is the data and image processing, described in Section 3.2.

3.1.1 Test specimen

Nine samples of PLGA 85:15 were prepared and tested. Due to elevated costs of this material, the samples were obtained from the material remaining in the sprue region of a mold used in the injection of craniofacial plates. The samples were machined into cylindrical shape (6x6 mm, height/diameter=1) and subsequently polished using a 1500 grit sandpaper.

3.1.2 Test settings

The PLGA samples were compressed in a servo-hydraulic MTS Bionix Machine. The tests were performed at Laboratório de Engenharia Biomecânica (LEBm - UFSC) in a temperature controlled room at 23°C. A special testing device was utilized in order to reduce machine compliance and reduce transversal loads. This compression rig also provides support for a Linear Variable Differential Transformer (LVDT), which enables measurement of the axial displacement of the compression plate instead of the whole crosshead system. The device is presented in detail in (SONNENHOHL, 2015).

The driving displacement was set to 1.8mm, but due to machine compliance the true displacement of the specimens was 1.7mm or approximately 0.333 of compressive true strain, i.e., within the finite strain regime. The test was repeated for three strain rates, resulting in 3 samples for each strain rate. The nominal crosshead speeds were set to 6.0×10^{-1} , 6.0×10^{-2} and 6.0×10^{-4} mm/s, resulting in the nominal (engineering-) strain rate of 1.0×10^{-2} , 1.0×10^{-3} and $1.0 \times 10^{-4} s^{-1}$, respectively.

The compression was filmed using a Point Grey camera (Flea3-SW-14S3C-C). The camera was attached to a magnetic support that was fixed in the test machine base. The samples received backlighting which passed through a paper diffuser in order to enhance contrast between sample and background. This layout can be seen in Figure 6.

Initial testing revealed that the use of lubrication between sample and the surface of the compression device favored the development of unstable strain field configurations on the test specimen and both geometrical and mechanical behavior varied significantly in each test, as shown in Figure 7. Using no lubrication reduced these instabilities and produced more

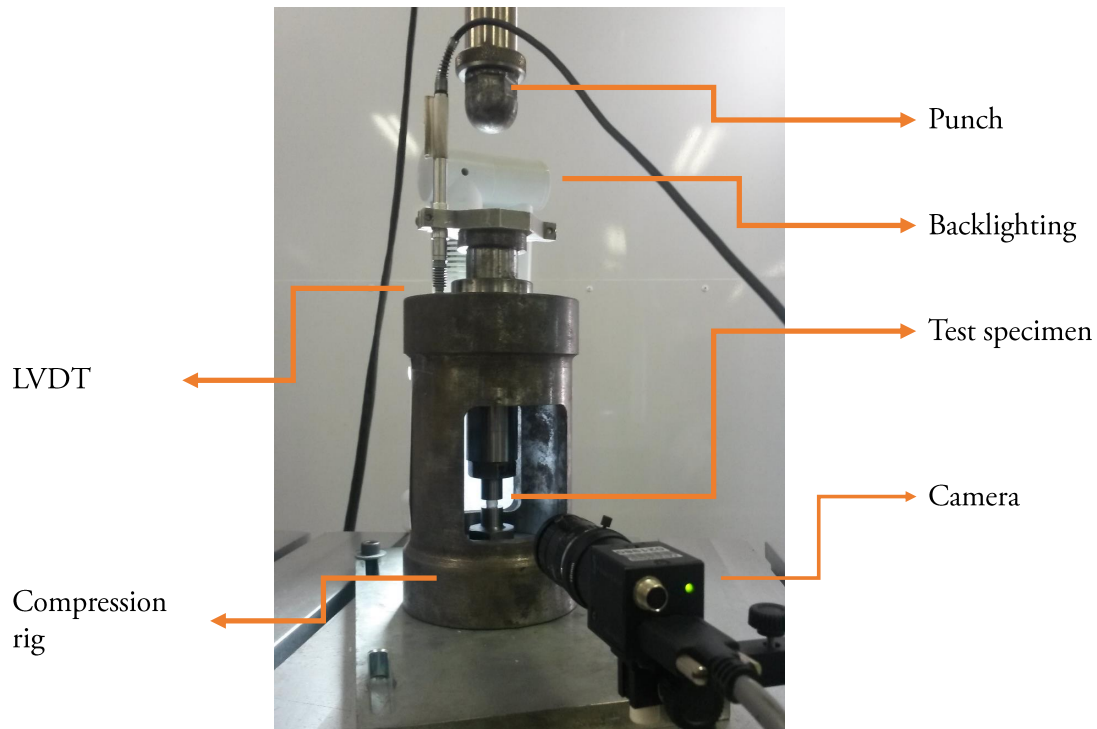


Figure 6 – Test layout

consistent results. However, lack of lubrication caused barreling of the test samples, thus generating a non-homogeneous stress/strain fields throughout the body. Several stages of the test are displayed in Figure 8. The displayed images correspond to a test performed at the slowest strain rate ($1.0 \times 10^{-4} \text{ s}^{-1}$).

3.2 IMAGE PROCESSING

An image processing algorithm was implemented in order to retrieve shape data from the recordings of the test. The main purpose of this algorithm is to measure the transversal displacement of virtual markers positioned on the surface of the specimens along the compression test. The algorithm was implemented in MATLAB making use of the *edge function* from the *Image Processing Toolbox*. This function analyzes figures by locating strong gradients in intensity images and interpreting as edges of different features of the image, returning a black and white binary image, as shown in Figure 9. Each frame of the video was processed using the edge detection. It was also implemented the automatic tracking of relative distance between the upper and lower metallic plates so that the instantaneous height h could be tracked from image data as well. In order to extract instantaneous diameter of the test specimens, five markers were virtually placed at each side along the specimen current height and their transversal

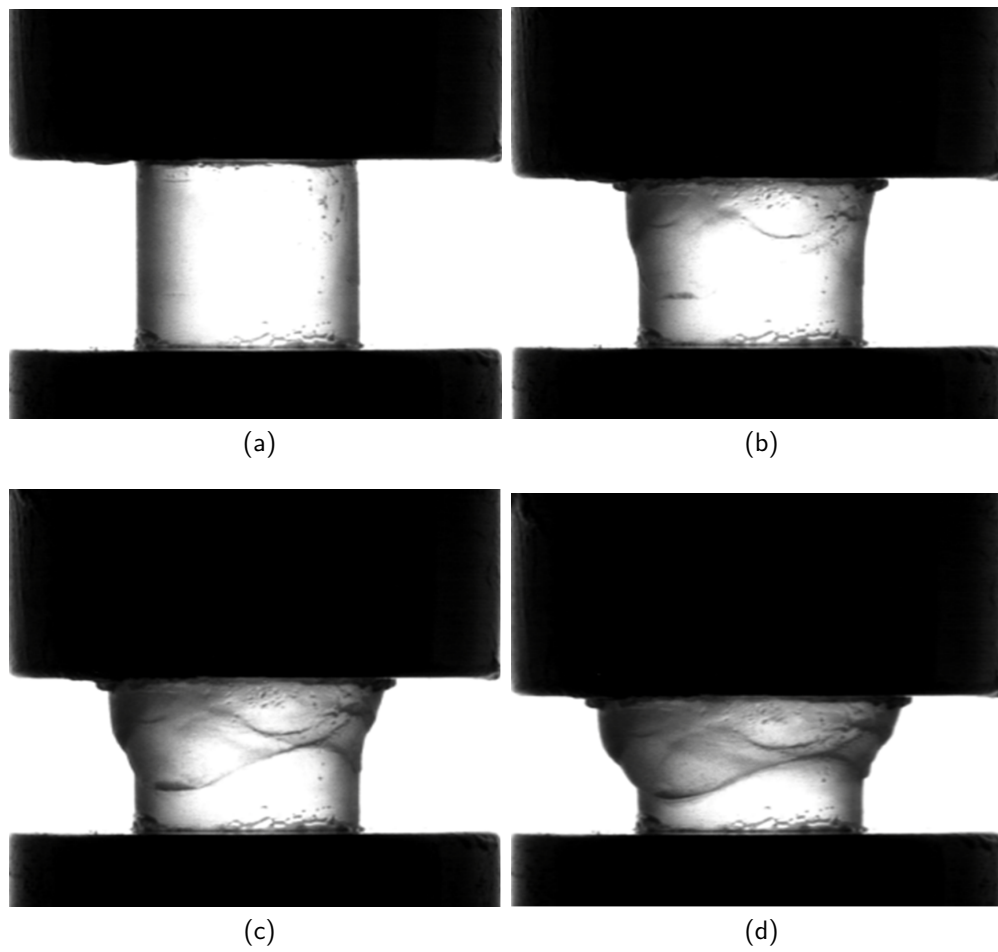


Figure 7 – Example of strain localization usually found in lubricated compression tests.

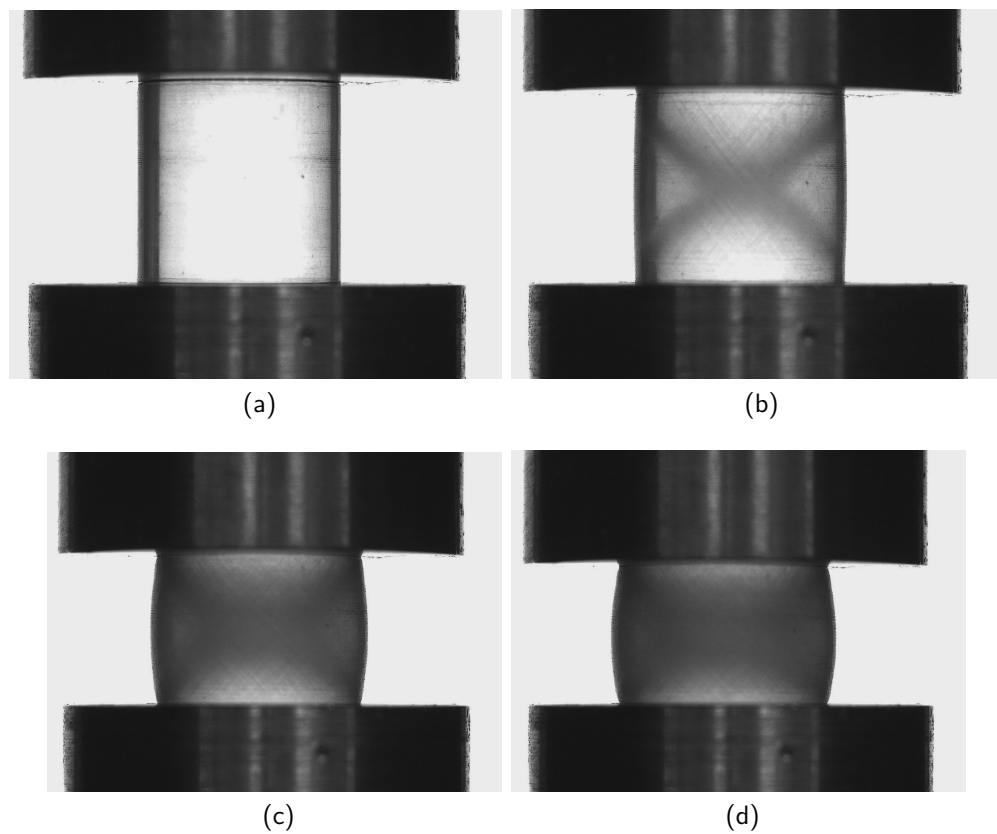


Figure 8 – Stages of the test specimen along the compression test - formation of barreling.

displacements were tracked. The markers always assume their vertical position relative to the current distance between plates ($1/6 h$, $2/6 h$, ...). The region defined by the vertical red lines in Figure 9 is the region where the height was tracked, while the horizontal blue lines define a region where the sample was detected and the region where the edge detection is performed.

One unforeseen problem on the image acquisition was the presence of reflection due to positioning of the camera. This could cause the algorithm to detect slightly taller samples than reality. The reflection effect was compensated digitally.

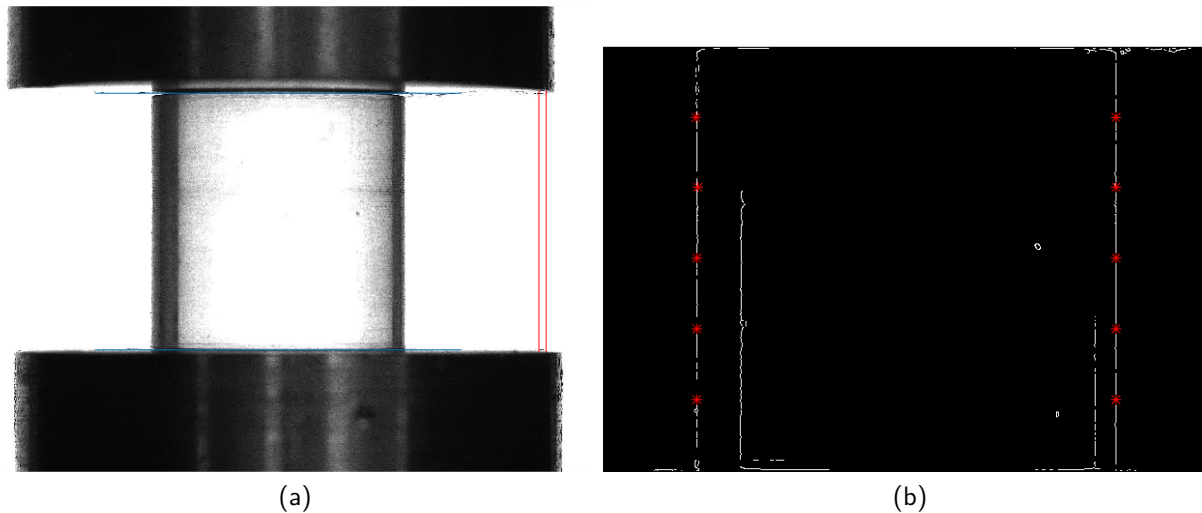


Figure 9 – Edge detection tool. (a) base image and (b) detected edges. The red markers track the diameter.

3.2.1 Post-processing

The data made available by means of three measuring devices (LVDT, camera and testing machine) need to be synchronized since the acquisition time and the data acquisition rate are not necessarily the same for all devices. One distinct event is when the axial displacement reaches its maximum. The data was synchronized by using this event as a reference. The axial displacement captured by the image processing algorithm was compared to the LVDT data in order to determine the spatial resolution, pixels per millimeter, and use this information to convert the radial displacement data to millimeters.

From Figures 10, 11 and 12 it can be observed that exists a difference from 0.1 to 0.2 mm in measurement from the driving displacement set in the testing machine (MTS) and that measured by the LVDT. One probable cause of this difference is the deformation of the testing machine itself. The actual displacement imposed on the test specimens is 1.7 mm, as measured by the LVDT, instead of the nominal 1.8 mm measured by the testing machine (MTS). Regarding the video processing algorithm, it was successful in measuring axial displacement along the test. The error between optical (video) and LVDT measurements observed during unloading is irrelevant to the current procedure and was disregarded.

3.2.1.1 Profile and volume

Although the cylindrical shape was not preserved, it is reasonable to consider the hypothesis of axisymmetry. The horizontal distance between markers can be supposed to be approximately the specimen diameter d , and the crosssectional area as the area of a circle. To calculate the volume, the specimen was supposed to be a solid of revolution. On each side of the specimen, the lateral shape was defined by fitting a quadratic expression, $a(d/2)^2 + b(d/2) + c$, at each frame using the position of the markers, as shown in Figure 13. Parameters at the i -th frame are henceforth denoted by the subscript i , i.e., a_i , b_i and c_i . The volume V was calculated by the integral 55

$$V_i = \pi \int_0^{h_i} (a_i(d/2)^2 + b_i(d/2) + c_i)^2 r, \quad (55)$$

where h_i is the specimens height at the frame. The axial and transversal strain at the k -th marker are defined as shown in Equations (56) and (57)

$$\epsilon_{\text{Axial},i} = \ln\left(\frac{h_i}{h_0}\right), \quad (56)$$

$$\epsilon_{\text{Transversal},i}^k = \ln\left(\frac{A_i^k}{A_0}\right) = 2 \ln\left(\frac{d_i^k}{d_0^k}\right). \quad (57)$$

3.3 EXPERIMENTAL RESULTS

3.3.1 Compressive force

Figures 14, 15 and 16 show the compressive force as measured by the testing machine. The typical toe region in the beginning of compressive tests was compensated following the ASTM standard D 695 (ASTM..., 2015). In the small displacement region, a linear behavior can be observed with low sensitivity to strain rate. From 0.2 mm onwards the strain rate effect is more prominent, also occurring the loss of linearity and a steep softening of the material. The softening is then followed by smooth hardening. All the tests specimens subjected to the highest strain rate presented a secondary loss of resistance in the region between 0.4 to 1.0 mm of axial displacement. For each rate the mean response was calculated and used as basis for the identification procedure. The response for each strain rate is displayed in Figure 17.

3.3.2 Transversal Displacements

The markers were enumerated from 1 to 5 according to its height relative to the base. The diameter along the height was used to calculate the transversal displacement in these five positions. Figures 18, 19 and 20 present the transversal displacement in relation to the axial displacements. All markers exhibit the same transversal displacement for small axial displacements (up to 0.35mm). After that there is a separation in these curves, meaning that

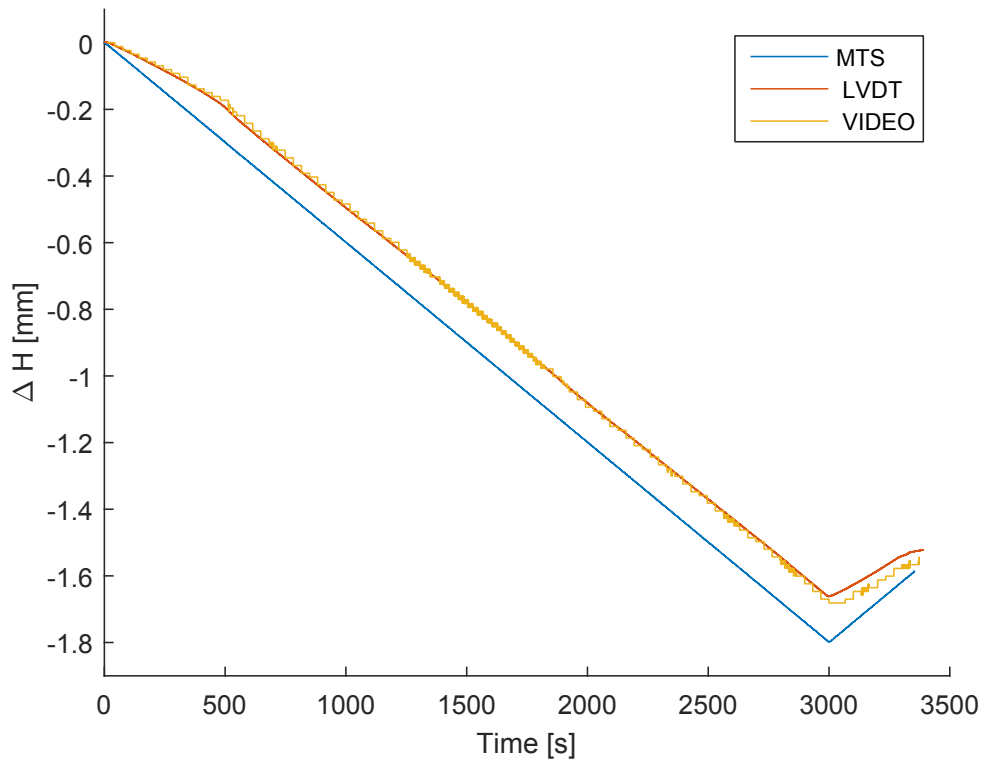


Figure 10 – Axial displacement measured by testing machine (MTS), LVDT and video. TS 09 - Slow strain rate.

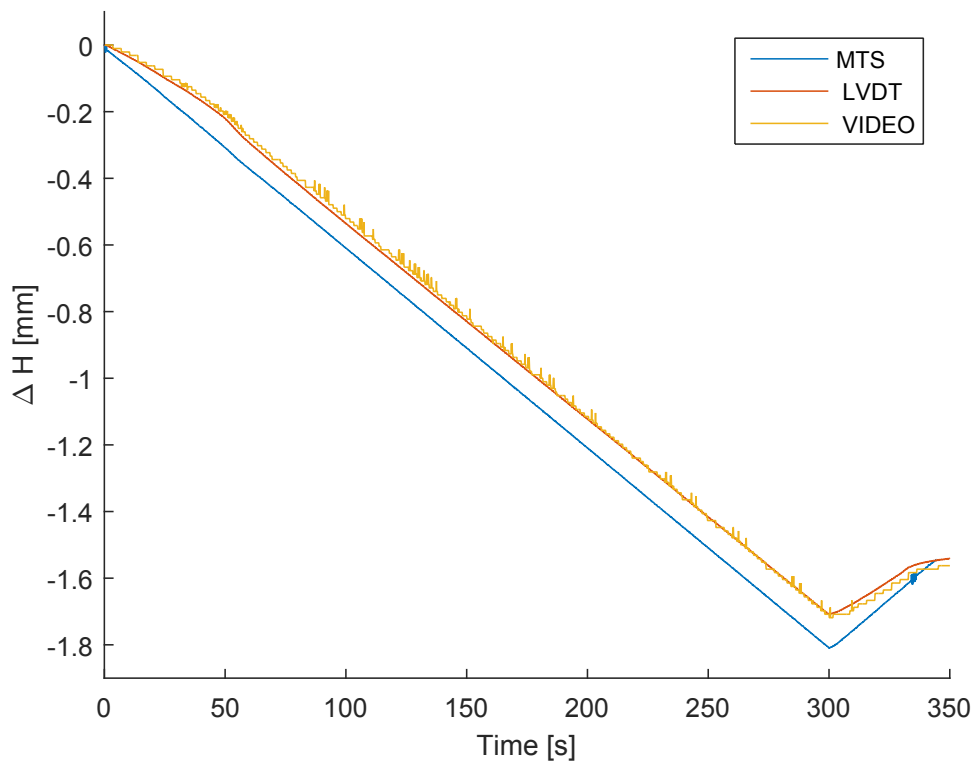


Figure 11 – Axial displacement measured by testing machine (MTS), LVDT and video. TS 06 - Medium strain rate.

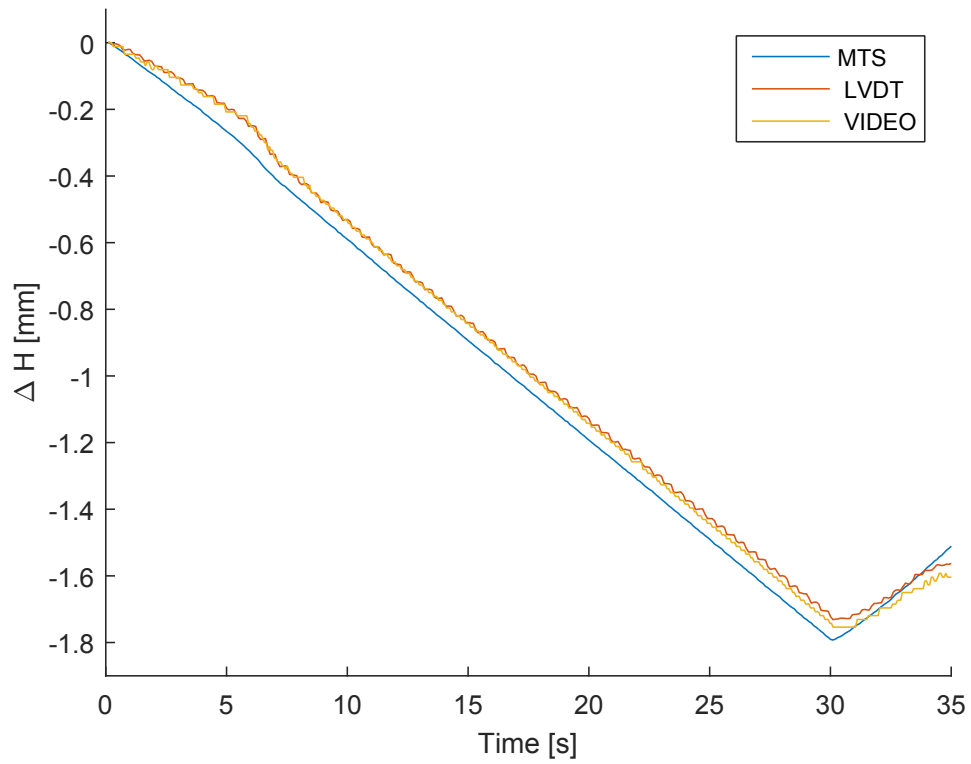


Figure 12 – Axial displacement measured by testing machine (MTS), LVDT and video. TS 01 - Fast strain rate.

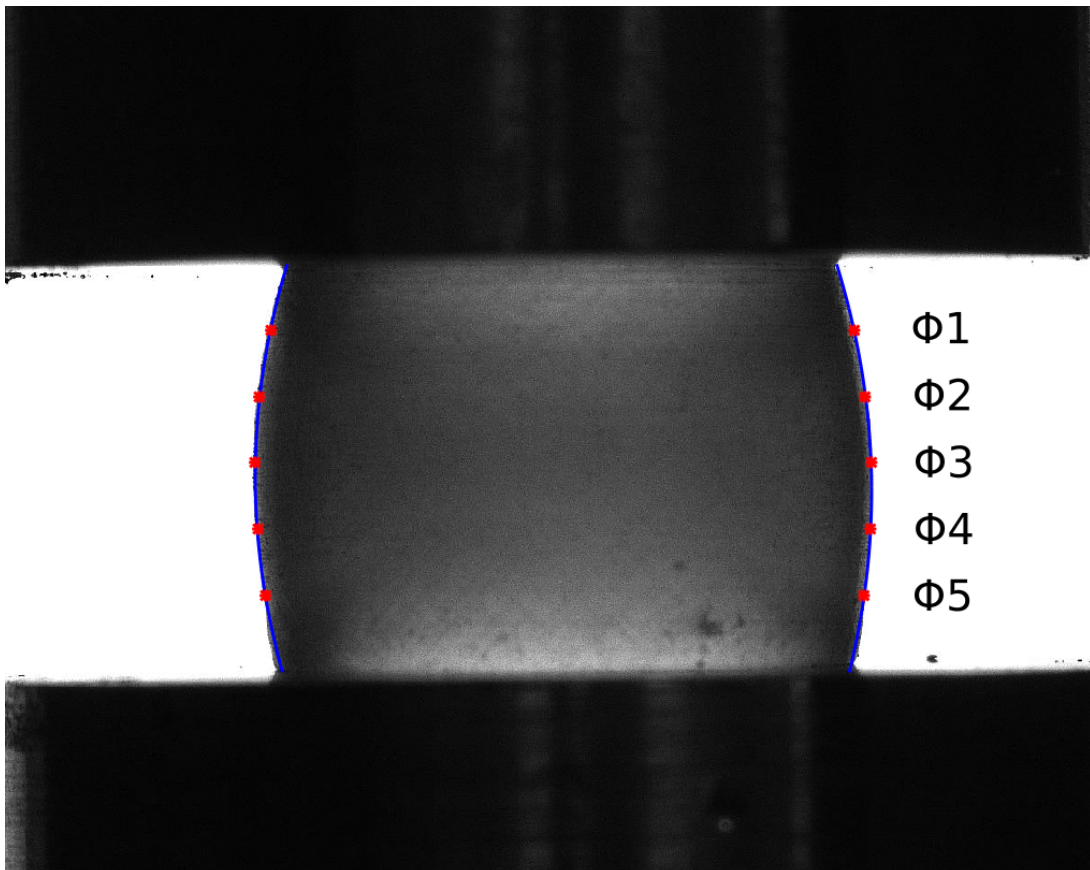


Figure 13 – Image processing: markers (in red) and the lateral shape approximated by a quadratic function (in blue).

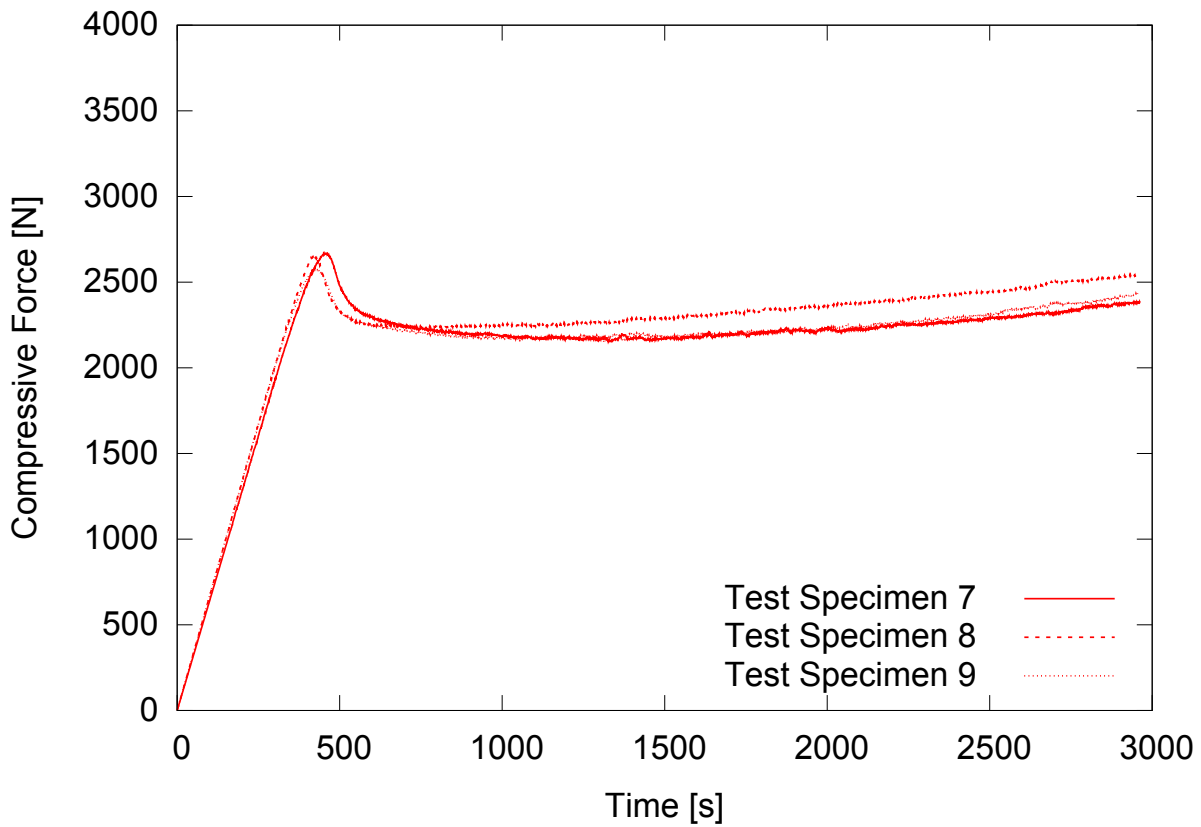


Figure 14 – Compressive force along the test. $\dot{\epsilon} = 1.0 \times 10^{-4} s^{-1}$.

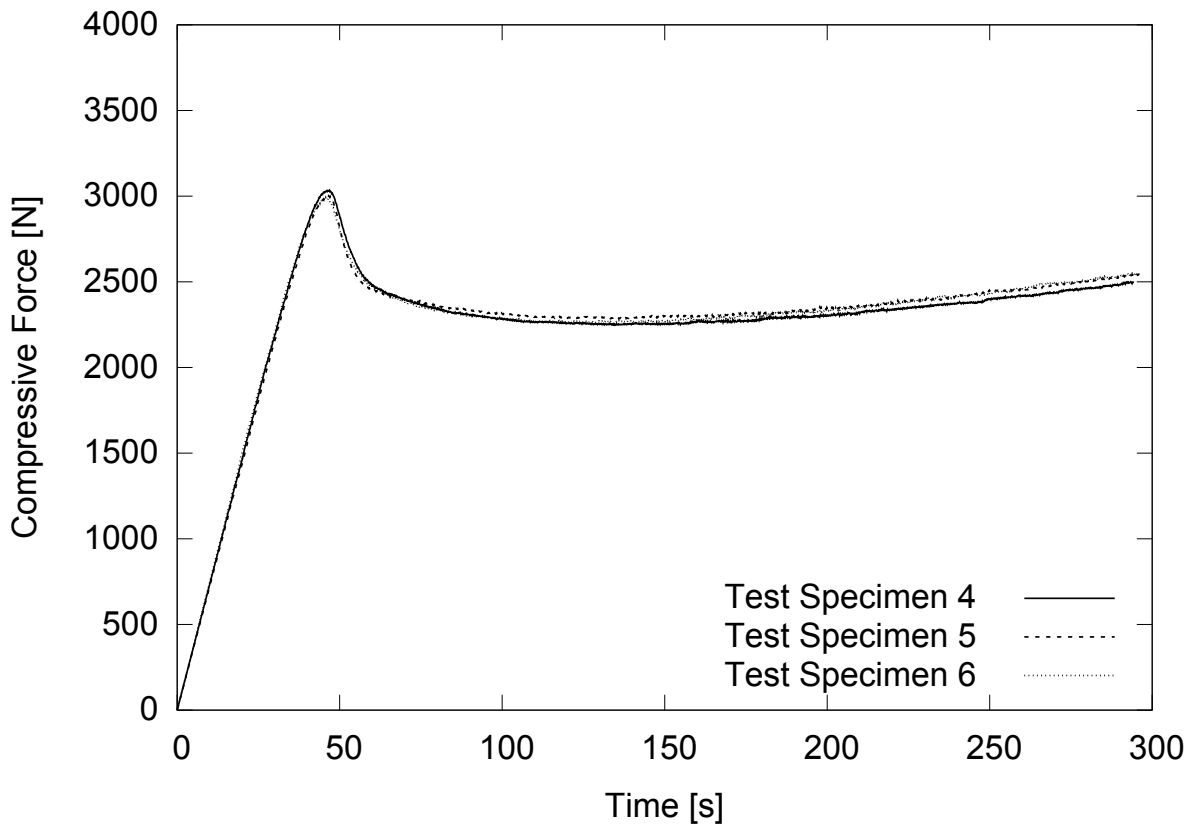


Figure 15 – Compressive force along the test. $\dot{\epsilon} = 1.0 \times 10^{-3} s^{-1}$.

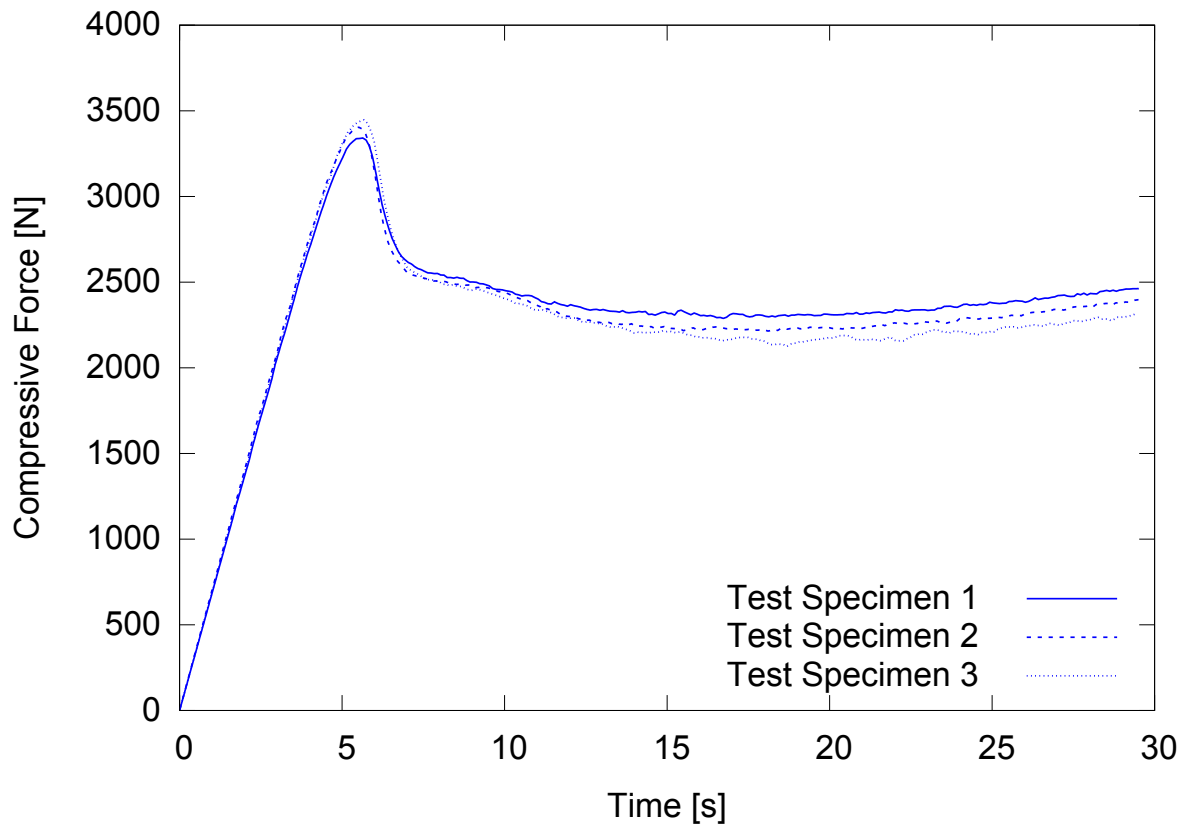


Figure 16 – Compressive force along the test. $\dot{\epsilon} = 1.0 \times 10^{-2} s^{-1}$.

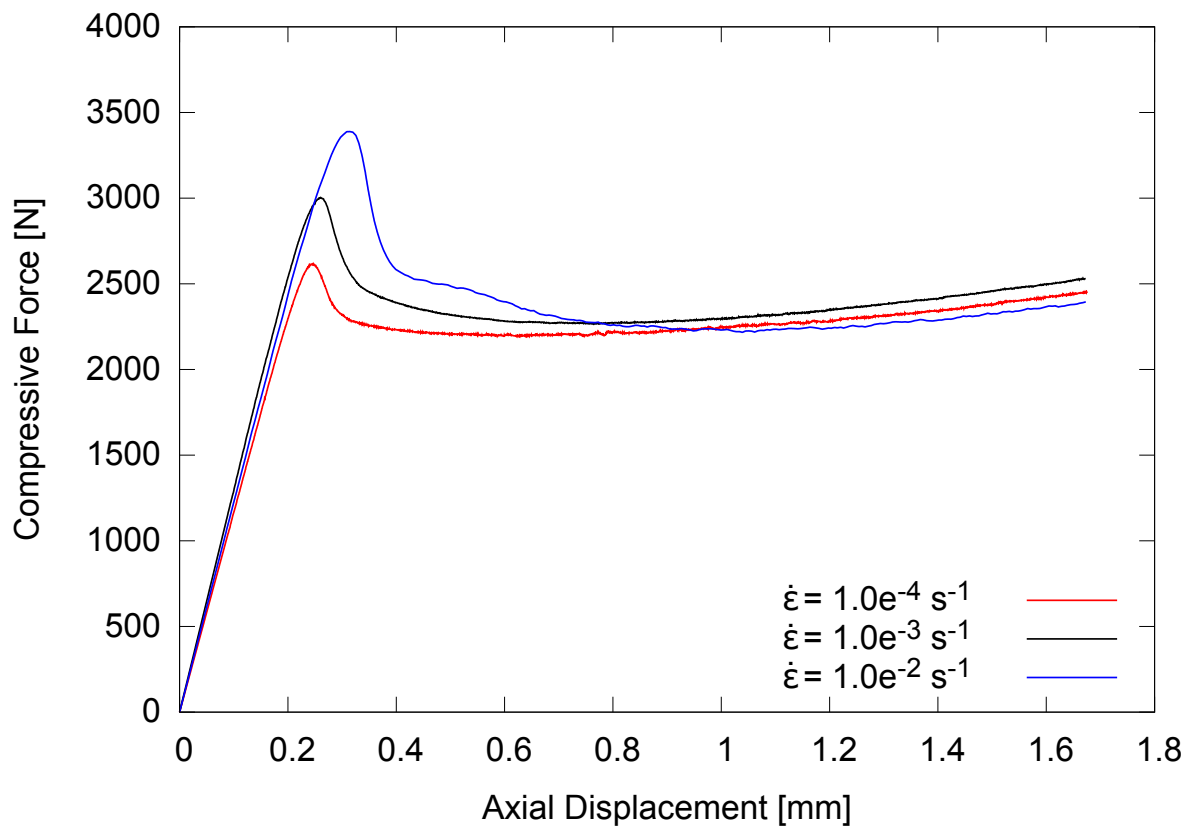


Figure 17 – Mean compressive force for each strain rate in terms of displacement.

barreling is beginning to occur. Comparing Figures 18, 19 and 20 to Figure 17, the initiation of barreling seems to be related to yielding of the material.

3.3.3 Volume change

Figure 21 shows the volumetric ratio, instantaneous volume by initial volume, calculated as explained in Section 3.2.1.1. A linear loss in volume occurs in the small displacement region. This trend is changed in the same region where softening is present (see Figure 17), and larger axial displacements are accompanied by a volume recovery. A similar behavior has been reported in Jerabek, Major, and Lang (2010), where a volume decrease was observed in the pre-yield regime, whereas a volume increase was found in the high strains regime. The author hypothesizes that this effect from the micro-structural point of view might be due to destruction of crystallites leading to a decrease in density.

Once again, the curve for the highest strain rate shows different behavior in comparison to the others, possibly due to the secondary resistance loss. The relation between volumetric ratio and rate sensitivity is unclear: One might expect that the volumetric ratio would vary monotonically with increasing strain rates. However, that does not hold true since the slow strain rate displays a behavior between the medium and fast strain rates. The reasoning behind this are in need of further investigation.

3.3.4 Homogeneous range

Barreling induces a complex distribution on the stress and strain fields. It is reasonable, however, to define a range where the effects of an heterogeneous field is not so prominent. Based on Figures 18, 19 and 20 no significant barreling occurs in the region between 0 to 0.2mm of compressive displacement. Up until 0.35 mm, the difference between the transversal displacement of the markers is lower than 2%. Based on this small difference, in this work, it is defined that up until 0.35mm in axial displacement the test specimens are assumed to have an homogeneous stress/strain field. Although this is not objectively true and some level of barreling does occur and some level of strain localization is expected, for the purpose of constitutive parameters identification this simplifying hypothesis is adopted. The region from 0 to 0.35mm of axial strain is henceforth denoted as the homogeneous region.

3.3.5 Elastic constants

The shear modulus μ and bulk modulus K used in the CF model (or G and K for FSF model) can be estimated from experimental results directly. Assuming that the material behaves as a linear elastic with a homogeneous stress/strain distribution, the elastic modulus E is recovered by transforming the force-displacement curve to a true stress-strain curve. A linear regression was performed to the data from 0 to 0.02 of axial strain and the elastic modulus is taken as the slope of that line. The Poisson ratio ν can be estimated from the

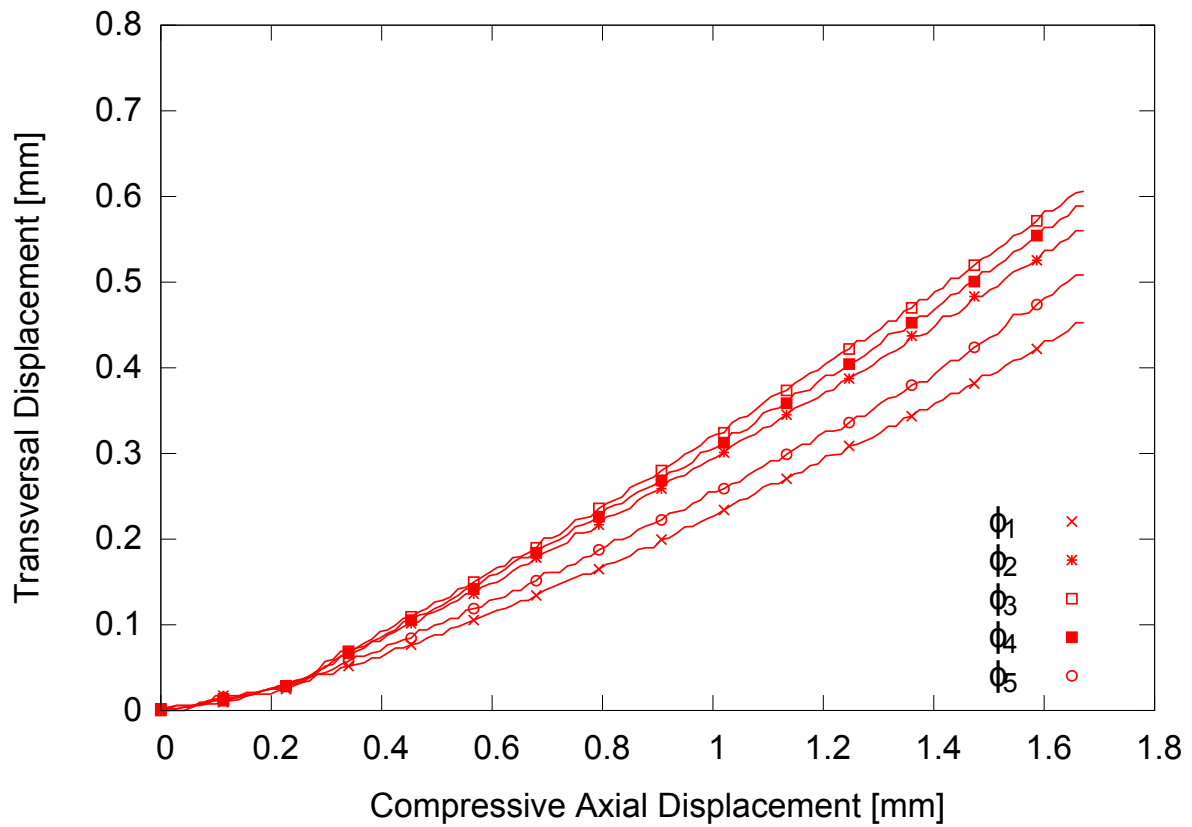


Figure 18 – Transversal displacements at each marker.

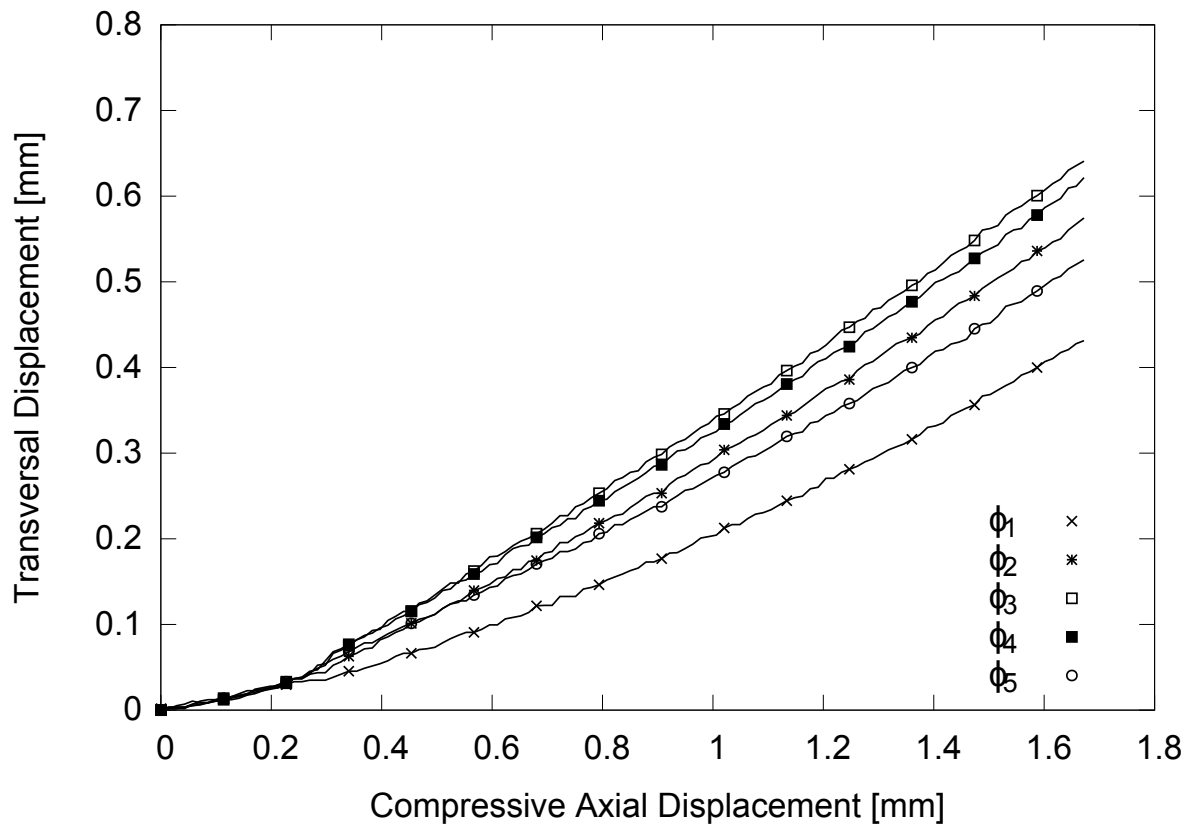


Figure 19 – Transversal displacements at each marker.

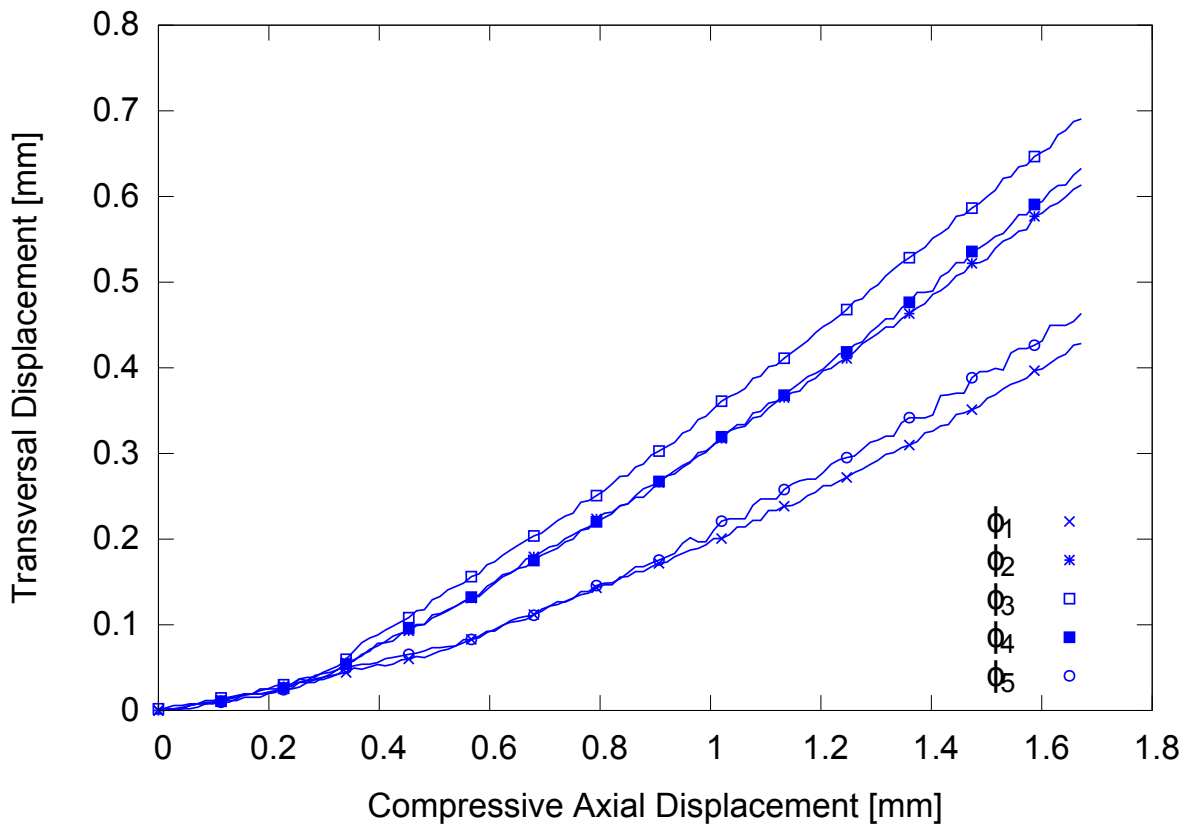


Figure 20 – Transversal displacements at each marker.

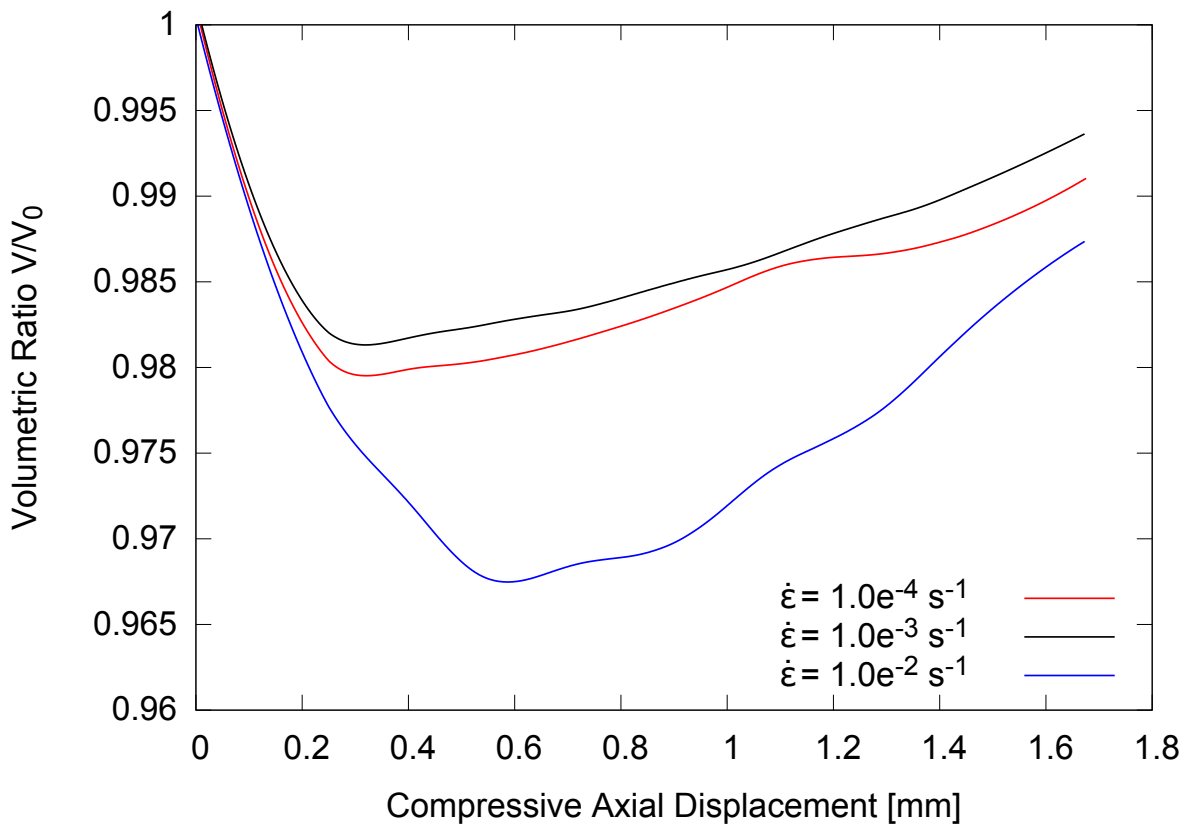


Figure 21 – Volumetric ratio.

	E	ν	μ	K
Slow	2420.0	0.2786	946.32	1822.0
Medium	2685.3	0.1997	1119.1	1490.5
Fast	2539.2	0.3105	968.79	2233.3
Mean	2548.2	0.2630	1011.4	1848.6

Table 4 – Elastic constants for each strain rate

transversal displacement data. A linear regression was once again performed on the same range of axial strain for the same region by

$$\nu = -\frac{\epsilon_T}{\epsilon_A} \quad (58)$$

value from 0.19 to 0.31 were found, depending on test specimen and strain rate, resulting in a mean value of 0.263. This indicates a significant loss in volume before barreling occurs. The shear modulus μ and bulk modulus K are calculated using the relationships between elastic constants presented in equations 59 and 60 :

$$\mu = \frac{E}{2(1 + \nu)}, \quad (59)$$

$$K = \frac{E}{3(1 - 2\nu)}. \quad (60)$$

The resulting values for μ and K are 1011.4 MPa and 1848.6 MPa, respectively. Values for all strain rates are displayed in Table 4. Although these parameters could be utilized in the models directly, they will be used as data to validate whether or not the identification procedures proposed in the next section are able to correctly identify these parameters.

4 IDENTIFICATION PROCEDURES

Based on the experimental results displayed in Section 3.3, it is now possible to identify constitutive parameters for PLGA. The set \mathbf{x} of constitutive parameters required for the CF model is:

$$\mathbf{x}_{CFM}=[\mu,K,H,n,c,\eta,S0,Scv,Sb,Sz,Sg], \quad (61)$$

and the set of constitutive parameters required for the Farias model is

$$\mathbf{x}_{FSFM}=[G,K,\mu,\lambda,m,S0,Scv,Sb,Sz,Sg]. \quad (62)$$

In this chapter the procedures for identification are explained.

4.1 OBJECTIVE FUNCTION

In parameter identification procedures the objective is to find the set \mathbf{x} of constitutive parameters that minimizes the error between experiment (EXP) and simulated response (SIM) of a system. In the present work, the error function $e(\mathbf{x})$ is calculated using the root-mean-square equation:

$$e(\mathbf{x}) = \sqrt{\frac{1}{n} \sum_{i=1}^p (R(\mathbf{x})_i^{EXP} - R(\mathbf{x})_i^{SIM})^2}, \quad (63)$$

where R is the response curve of a system, R_i its i -th point and p the total number of points. In this work, two responses for each strain rate are considered: the compressive force $F(\mathbf{x})$ and the transversal displacement $U(\mathbf{x})_T$ at the mid-section. One way to find the optimal set of parameters for more than one response simultaneously is through the weighted sum method, and the fitness $f(\mathbf{x})$ of the parameters

$$f(\mathbf{x}) = \sum_{j=1}^m \omega_j e_j(\mathbf{x}), \quad (64)$$

where m is the number of response sources and ω_j the weights associated with the j -th response source. More explicitly, the fitness is given by:

$$f(\mathbf{x}) = \omega_u \sqrt{\frac{1}{n} \sum_{i=1}^p (U(\mathbf{x})_{T,i}^{EXP} - U(\mathbf{x})_{T,i}^{SIM})^2} + \omega_F \sqrt{\frac{1}{n} \sum_{i=1}^p (F(\mathbf{x})_i^{EXP} - F(\mathbf{x})_i^{SIM})^2} \quad (65)$$

To account for all strain rates simultaneously, the weighted sum method is used:

$$M(\mathbf{x}) = \sum_{k=1}^l \omega_k f_k(\mathbf{x}), \quad (66)$$

where $M(\mathbf{x})$ is the resulting objective function, ω_k the k -th weight and l the total number of strain rates. The optimization problem is formally presented as:

$$\mathbf{x}^{opt} = \arg \min M(\mathbf{x}). \quad (67)$$

A schematic representation of the evaluation of objective function is shown in Figure 22.

4.2 IDENTIFICATION PROCEDURES

A hybrid approach was implemented using the PSO algorithm in an initial stage for global search and the NM algorithm for local search. Additionally to a hybrid optimization procedure, it could be valuable to analyze different procedures of identification. The main goal of testing different identification procedures is to investigate if is possible to reduce computational time to identify parameters when a large number of constitutive parameters are needed and a non-trivial simulation is necessary.

Taking into consideration that non-homogeneous fields develop during the specimen compression, the identification procedure was further subdivided into where homogeneity is admissible and where it is not. Assuming homogeneity allows evaluating only the material constitutive model (the equivalent of a single integration point in FEM) while the non-homogeneous test was performed using a Finite Element simulation. Both simulations are explained in detail in Section 4.3.

Four identification procedures were tested: FEM-based identification, constitutive-based identification and two mixed approaches based on the former procedures, namely mixed-1 and mixed-2 identification procedure. These procedures are described in the following sections.

4.2.1 FEM-based identification procedure

The FEM-based identification procedure is the most commonly used in the researched literature when considering non-homogeneous compression test. The simulated results are obtained through a FEA of the uniaxial compression test, as shows Figure 23. Conceptually, this procedure is the most straightforward because the comparison is direct. The experimental results are a relationship between intrinsic material response and specimen geometry, the FE simulation produces exactly that, and no hypothesis on the stress or strain fields needs to be made. However this type of simulation is time consuming so the evaluation of one objective function becomes burdensome.

4.2.2 Constitutive-based identification procedure

The constitutive-based identification procedure is the most commonly used procedure for the identification of constitutive parameters. Such a procedure considers an homogeneous

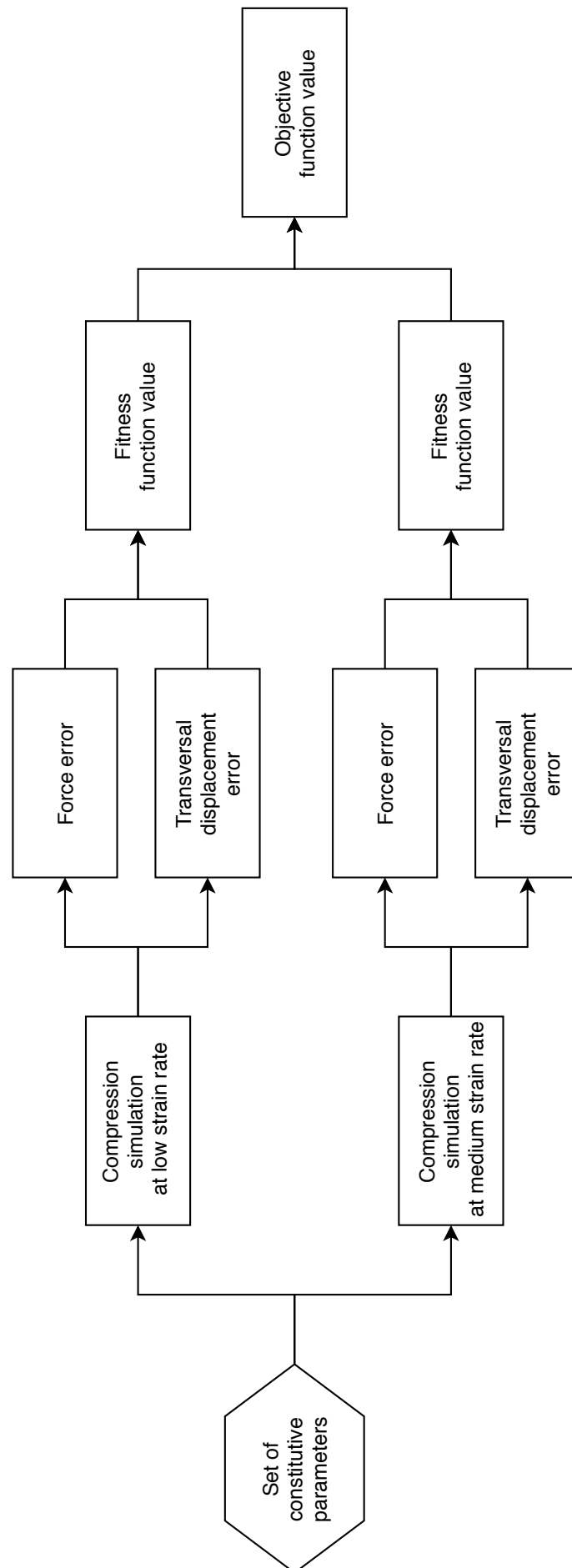


Figure 22 – Schematic representation of objective function evaluation

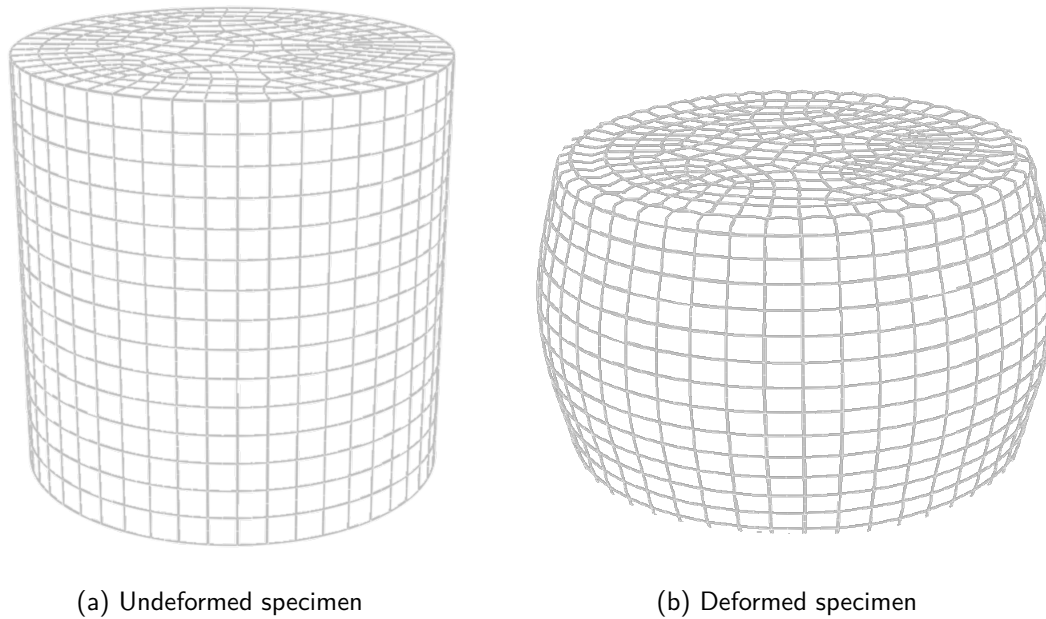


Figure 23 – Non-homogeneous compression - Finite Element Analysis.

stress/strain field during testing, as shown in Figure 24. Considering homogeneity means that the response is equal across the homogeneous region, so that evaluating the constitutive model (CM) once is enough to represent all the region. This makes the constitutive-based identification procedure much less time consuming than the FEM-based. It is conceptually false to consider a homogeneous identification approach to a non-homogeneous test, yet, this procedure was performed in order to understand how much the identified parameters are affected by this false hypothesis and to see whether or not it could be a cost-effective solution.

4.2.3 Mixed-1 identification procedure

The Mixed-1 identification procedure divides the identification procedure in two stages. In the first the compression simulation consists in evaluating the constitutive model, and afterwards a new optimization stage is performed using the NM algorithm and FEA. The Mixed-1 approach can be seen as the constitutive-based procedure with a tuning stage at the end, to mitigate the effects of the homogeneous hypothesis on the parameters.

4.2.3.1 Mixed-2 identification procedure

The Mixed-2 is also a two-stage approach. The stages are divided by the considerations made to the stress/strain field. The first stage is defined when assuming homogeneity is a reasonable hypothesis, i.e. a homogeneous range, in the small strains region. The hybrid PSO-NM is used to obtain a first estimation of the constitutive parameters and the resulting parameters are the basis for a second identification stage. The search space is reduced to a small region centered on the resulting parameters from the earlier stage. In the second stage

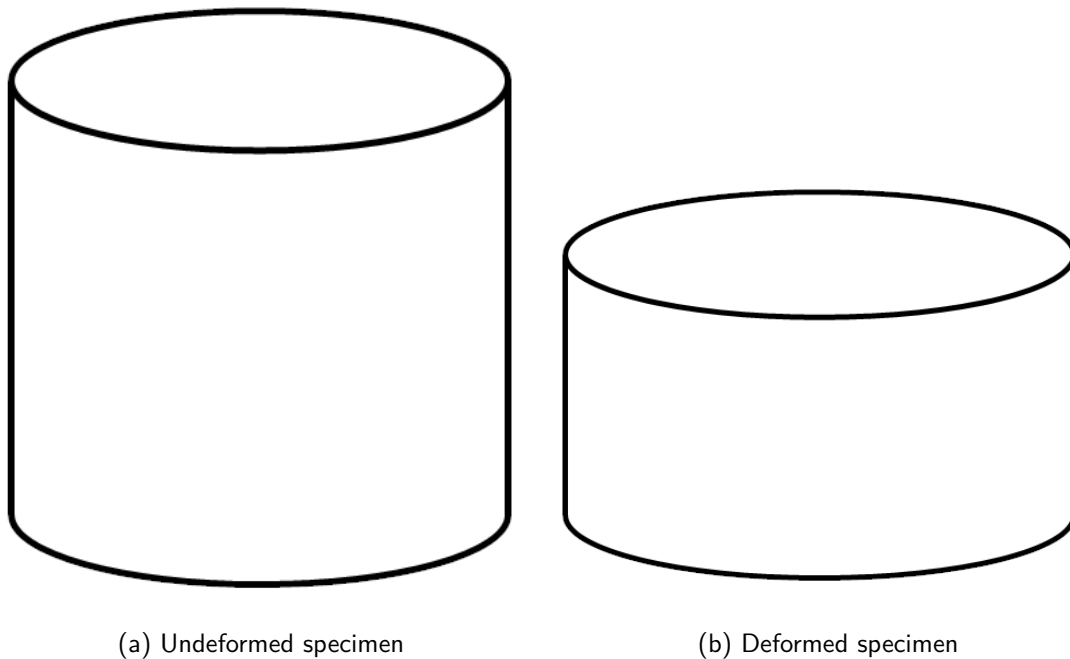


Figure 24 – Homogeneous compression - Constitutive Model Analysis.

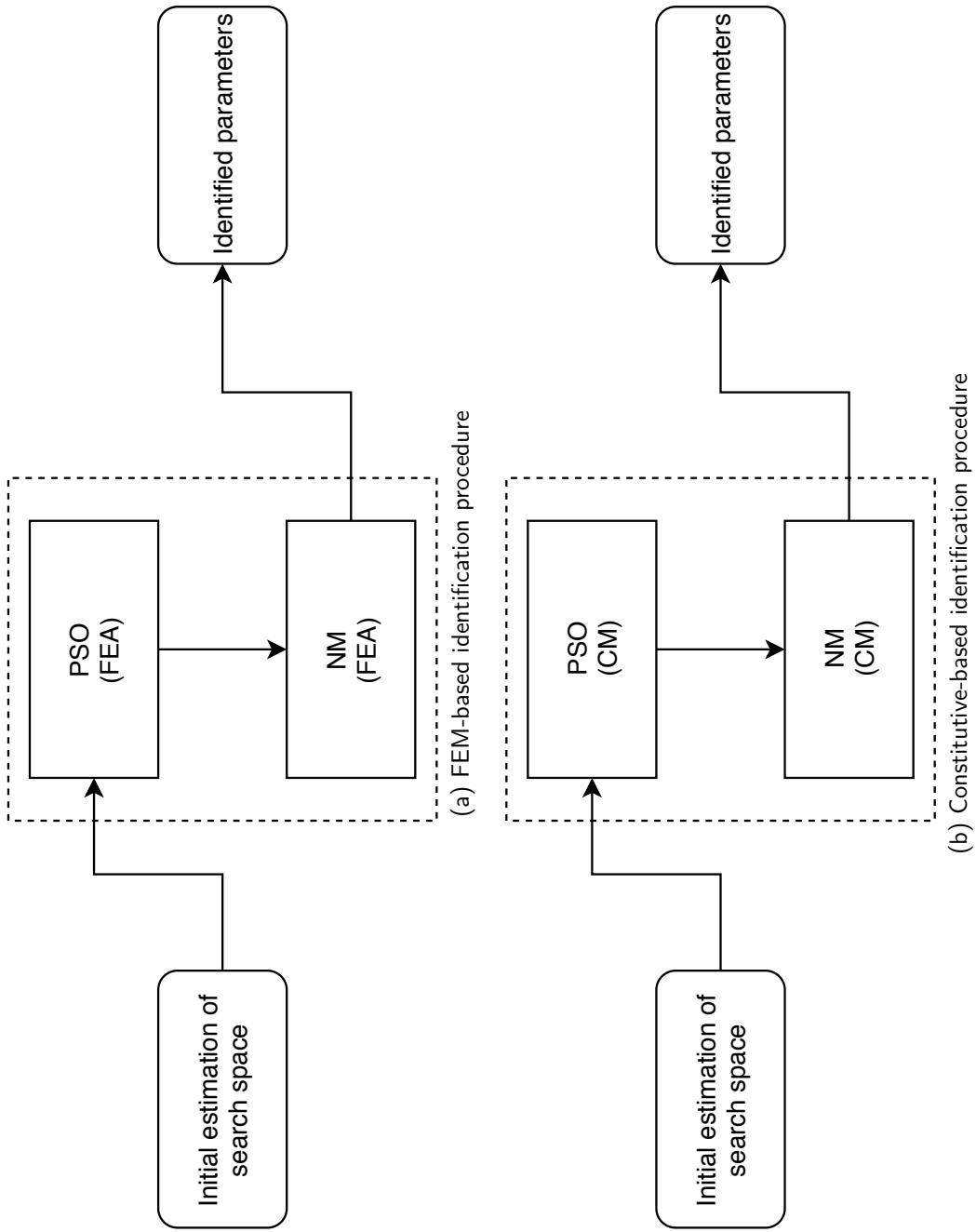
the hybrid PSO-NM is now performed using FEA, considering the whole compression test, including the non-homogeneous range.

This first stage can be seen as an exploration stage of the search space, checking feasible regions and quickly discarding unfeasible parameter sets. When the optimization algorithm defines a favorable region, the initial search space is reduced to this region and the second stage of the identification procedure starts. One of the goals of this approach is to approximate the elastic and softening parameters in the initial stage and identify all parameters, including hardening, on the latter stage. The identification procedures can be visualized in the schematics presented in Figure 24.

4.2.4 Defining an initial search space

Facing a new model and new material data, it can be troublesome to define where the optimum solution lies, thus, the initial step is to define the search range. Defining a narrow search space can bias to a local minimum and obliterate the optimization algorithm from better solutions. On the other side, a wide search space might be costly to evaluate. Where to define upper and lower limits, for the PSO algorithm for example, remains in the realm of educated guesses from the decision makers.

In the present work upper and lower limits were delimited by *a priori* sensibility analysis. From an initial set of promising parameters, one-by-one they were varied while maintaining the others constant. Attention must be given so that the parameters remain thermodynamically feasible. The upper and lower search limits are presented in Tables 5 and 6 for the CF model and FSF model, respectively.



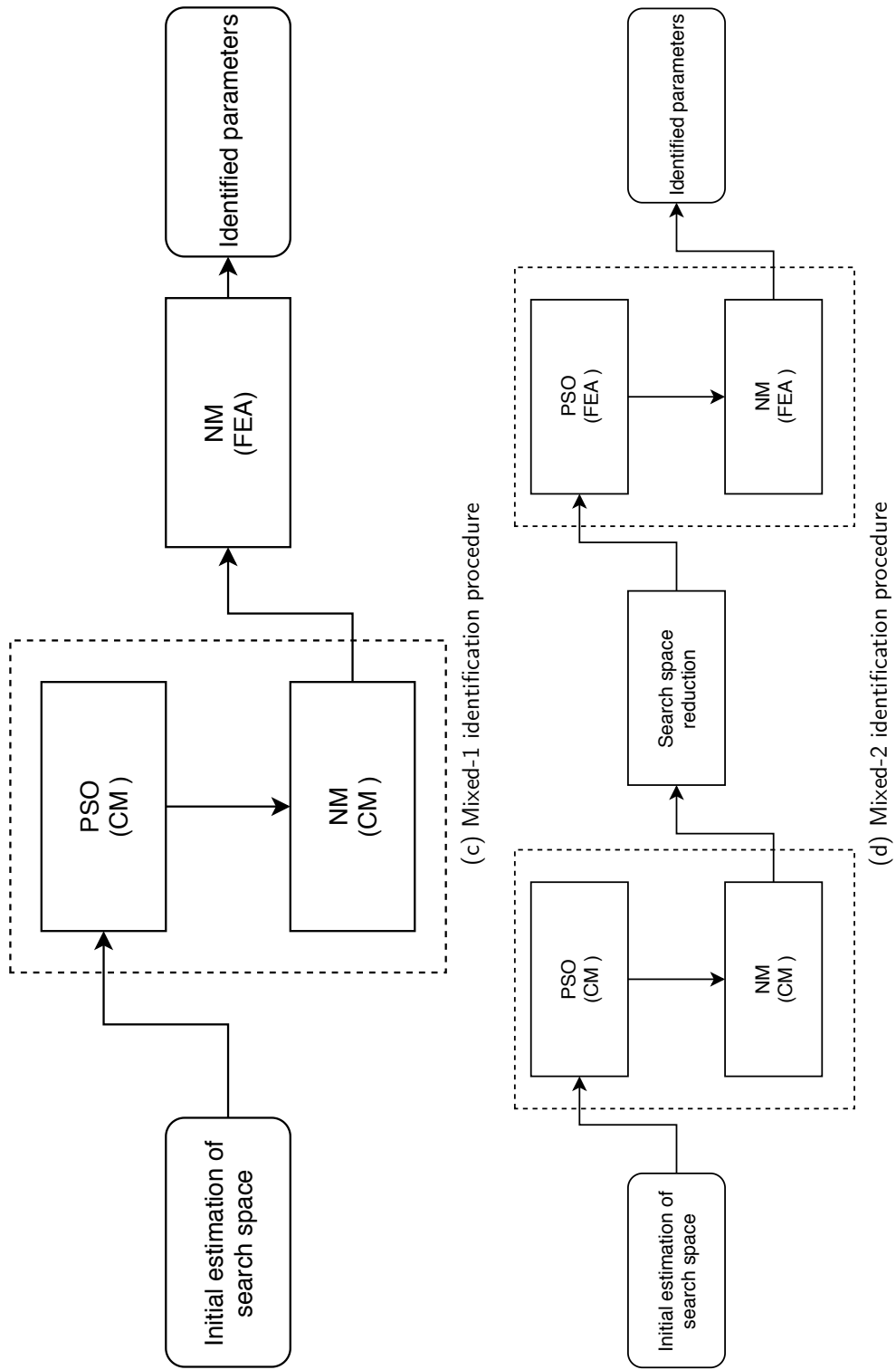


Figure 24 – Schematics the identification identification procedures.

	Lower limit	Upper limit
μ	800.00	1200.00
K	1500.00	2000.00
c	0.00	100.00
η	0.01	0.3
n	0.0	2.0
Hiso	0.001	0.500
S0	20.01	100.00
Scv	0.01	50.00
Sg	10.00	200.00
Sz	0.50	200.00
Sb	0.05	200.00

Table 5 – PSO variable limits for the de CF model.

	Lower limit	Upper limit
G	800.00	1200.00
K	1500.00	2000.00
μ	0.01	100.00
λ	0.01	50.00
m	0.01	0.10
S0	50.01	100.00
Scv	0.01	50.00
Sg	10.00	20.00
Sz	10.50	20.00
Sb	10.05	20.00

Table 6 – PSO variable limits for the FSF model.

4.2.5 Sampling the search space

The PSO population was set to 30 times de number of constitutive parameters. An optimal population size is problem dependent. This number comes from a priori testing, much lower sizes led to solution divergence, where higher populations were excessively time consuming with no noticeable improvement on the solution. The initial position of the PSO particles are usually started at random positions. Since one of the main goals of this work is to compare identification procedures, to start each procedure at random position is another source of uncertainty. In order to better compare the procedures the same initial positions were used across all identification procedures. To place the particles in the search space a Latin hypercube sampling procedure was used. Latin hypercube sampling is not a true random sampling, instead it takes into account the previously placed points and iteratively generates samples that maximizes the minimum distance between points. The goal is to have a good sample of the search space with the minimum number of points while aiming to not ignore any region of the search space.

4.3 NUMERICAL SIMULATION

To reproduce the force response and transversal displacement of the specimen profile two types of simulations were performed: a homogeneous compression and a Finite Element simulation. The homogeneous compression is the computation of the constitutive model in a uniaxial compression condition considering no-friction between specimen and the compression plates. For the FE simulation preliminary studies were performed on the effects of analysis type, mesh size, time discretization and influence of friction.

The resulting FE model is an axisymmetric 2D model also using the mid section as a second axis of symmetry, thus representing one-fourth of the longitudinal area. Instead of using a contact formulation, the top-most nodes were assigned a prescribed displacement in the axial direction while no transversal displacement was allowed, a situation analogous to a infinite friction coefficient.

The mesh consists of equally spaced 8-node quadrilateral elements. The mesh is a relatively coarse mesh with 64 elements and element size of 0.2. This is a compromise solution since further mesh refinement would not bring much difference to the measured responses, but would increase computational time significantly. Although each simulation would require its own mesh convergence tests, for practical reason the same mesh is used for all tested sets of parameters in the optimization process.

4.3.1 Algorithm

The optimization algorithms and identification procedures were implemented in a FORTRAN code. A pre-existing Finite Element solver was used. The solver utilized was an in-house project developed for non-linear and multi-scale applications. The code was extensively tested and compared with analytic examples and commercial softwares.

To reduce time in the PSO-FE stage, a parallel process was implemented and a network structure was utilized so that several particles (set of constitutive parameters) could be evaluated simultaneously. Each particle position is sent to a computer to be evaluated and, after the simulation is finished, the objective function value is sent back to the main process. This parallelization was implement in an asynchronous manner, i.e., each computer does not have to wait for the others. Once ones process ends another process request is received. This becomes important when using computers with vastly different processing power in order to make most use of the network structure. This implementation was responsible for an approximate 53% reduction in processing time in regard to a sequential evaluation procedure.

4.3.1.1 Handling simulation failure

Even though admissible limits for each parameter can be defined some set of parameter values might cause the simulation of a system to fail. It is not obvious how to predict that a set either exists in the search space and to recognize it *a priori*, before a simulation even

starts. Acknowledging this possibility, an identification procedure should be robust in handling this difficulty. Here, the algorithm handles this by assigning an infinity value to the objective function when a set of parameters produces a simulation that does not converge to a result. Due to the nature of the PSO and how each particle behaves semi-independently, this optimization algorithm was able to successfully overcome this difficulty. Other deterministic or heuristic approaches might fail if the search space contains such set.

4.3.2 Validation

The implementation of the optimization algorithms were validated using two test functions where the global minimum is known. The convex form of the Rosenbrock function was utilized to validate the Nelder-Mead algorithm, whereas the multimodal Rastrigin function was utilized to validate the PSO algorithm. Both algorithms were successful in finding the global minimum with the correct precision and convergence rate.

In order to validate the identification algorithm, stress-strain curves of PMMA and PETg were obtained from the works of Ames et al. (2009) and Dupaix and Boyce (2005), respectively. These materials were chosen in order to reproduce the identification procedure performed by Farias (2018), where the model presented in that work is known to successfully reproduce the mechanical behavior. In short, samples of PMMA were subjected to uniaxial compression under various strain rates (1.0×10^{-1} , 1.0×10^{-2} , 1.0×10^{-3}) at 100°C. PETg was subjected to uniaxial compression under the strain rates of 1.00, 0.10 and 0.01 at 25°C. The results are shown in Figure 25 and the identified parameters presented in Table 7. It can be observed that the algorithm was able to successfully identify constitutive parameters for these materials.

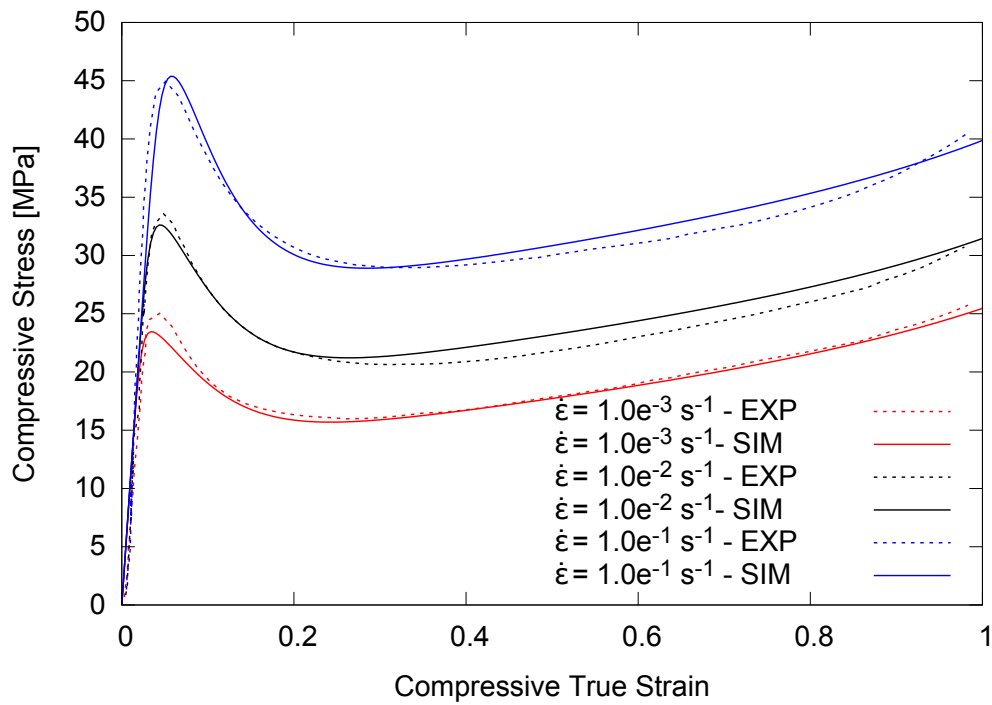
The same procedure was performed using the model proposed by de Castro (CASTRO, 2017). The model was also able to reproduce the mechanical response accurately, as it can be seen in Figure 26 and the parameters are shown in Table 8.

	PMMA	PETg
G	704.44	683.70
K	906.46	889.14
μ	03.97	11.17
λ	491.36	68.23
m	0.144	0.050
S0	36.42	40.37
Scv	20.00	21.20
Sg	66.92	48.19
Sz	17.84	09.64
Sb	03.35	01.22

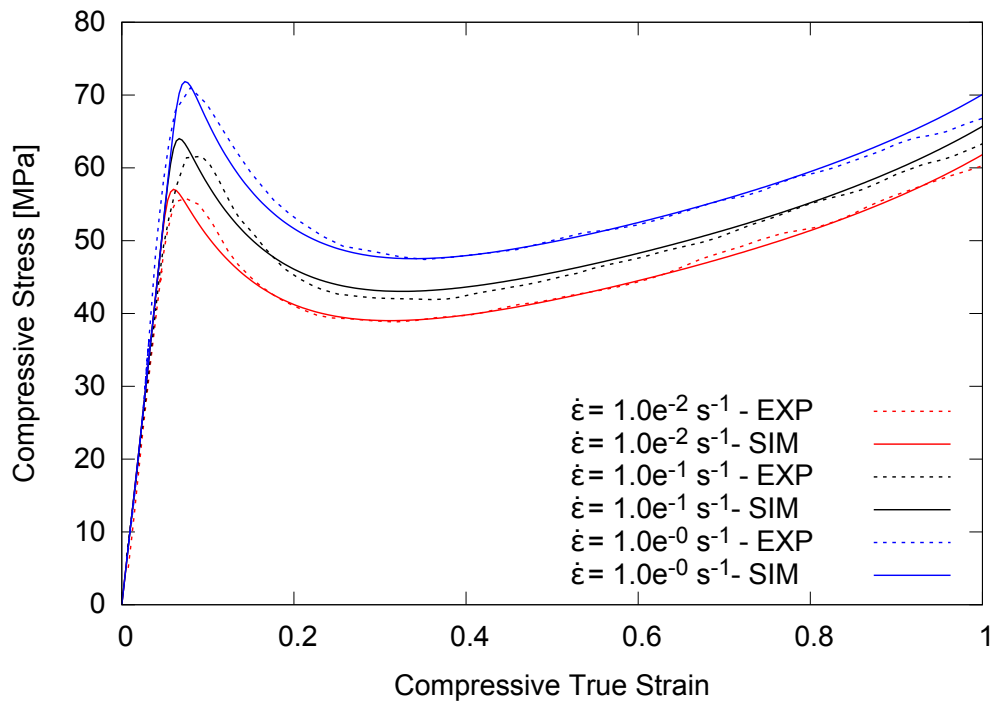
Table 7 – Identified parameters for PMMA and PETg for the FSF model

	PMMA	PETg
μ	642.31	675.08
K	1286.34	1228.49
c	0.01	0.36
η	0.140	0.230
n	2.51	2.49
Hiso	1.00	1.00
σ_{y0}	1.50	10.0
S0	36.93	60.87
Scv	19.83	25.22
Sg	26.45	74.85
Sz	20.00	19.97
Sb	0.50	0.5

Table 8 – Identified parameters for PMMA and PETg for the CF model

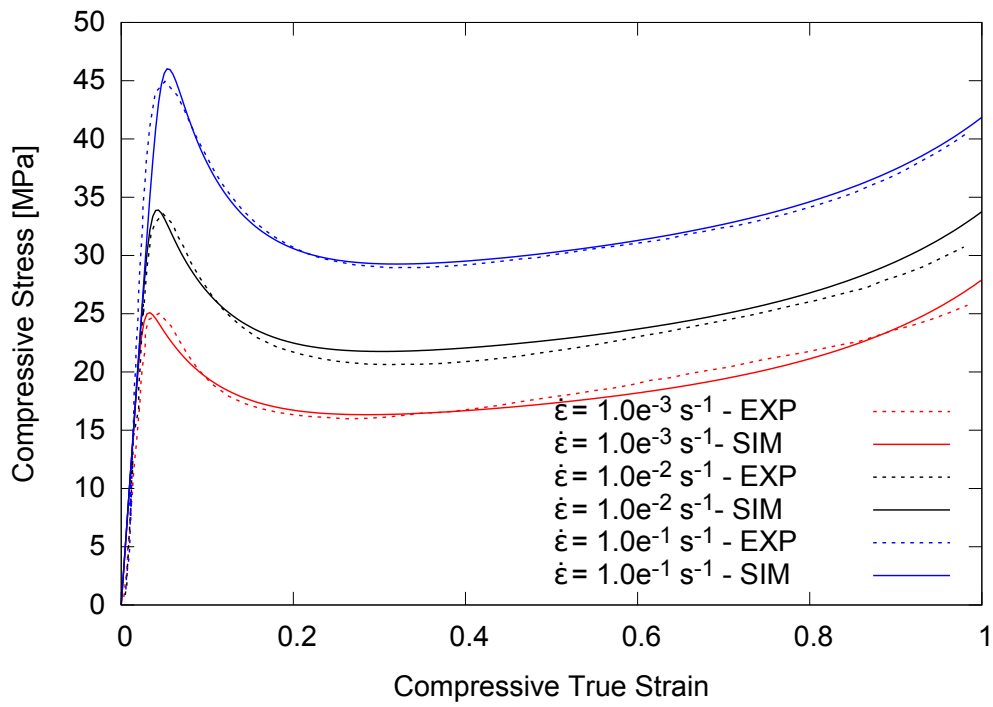


(a) parameter identification for PMMA

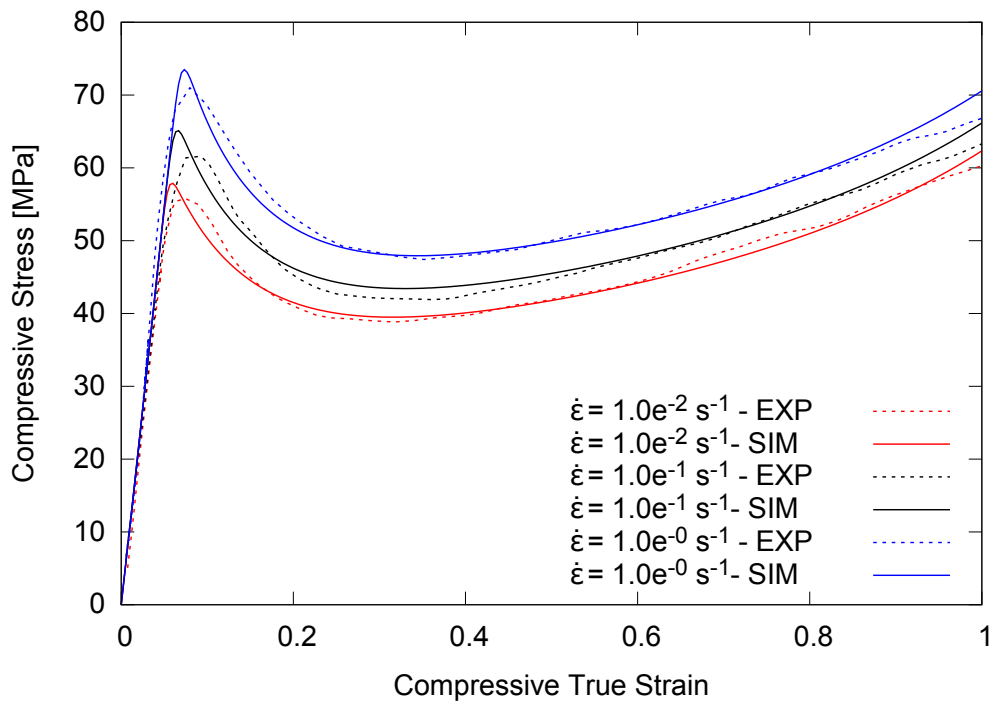


(b) parameter identification for PETg

Figure 25 – Calibrated FSF model for PMMA and PETg compression tests.



(a) parameter identification for PMMA



(b) parameter identification for PETg

Figure 26 – Calibrated CF model for PMMA and PETg compression tests.

5 IDENTIFICATION RESULTS

In this section are presented the identified parameters for the studied models and their simulated responses in terms of compressive force and transversal displacement at the mid-section. All responses shown in this chapter are the results of each identified parameter set utilized in a non-homogeneous compression test FE simulation, even for set identified through the constitutive-based identification procedure. This was done in order to compare procedures through a more egalitarian mean.

5.1 CF MODEL

Figures from 27 to 30 show the calibrated CF model to the experimental data obtained from compression test of PLGA. The calibrated model is represented by continuous lines and the experimental results by dashed lines. Table 9 presents the resulting set of identified parameters for each identification process and Table 11 presents the computing times for each identification process.

FEM-based identification

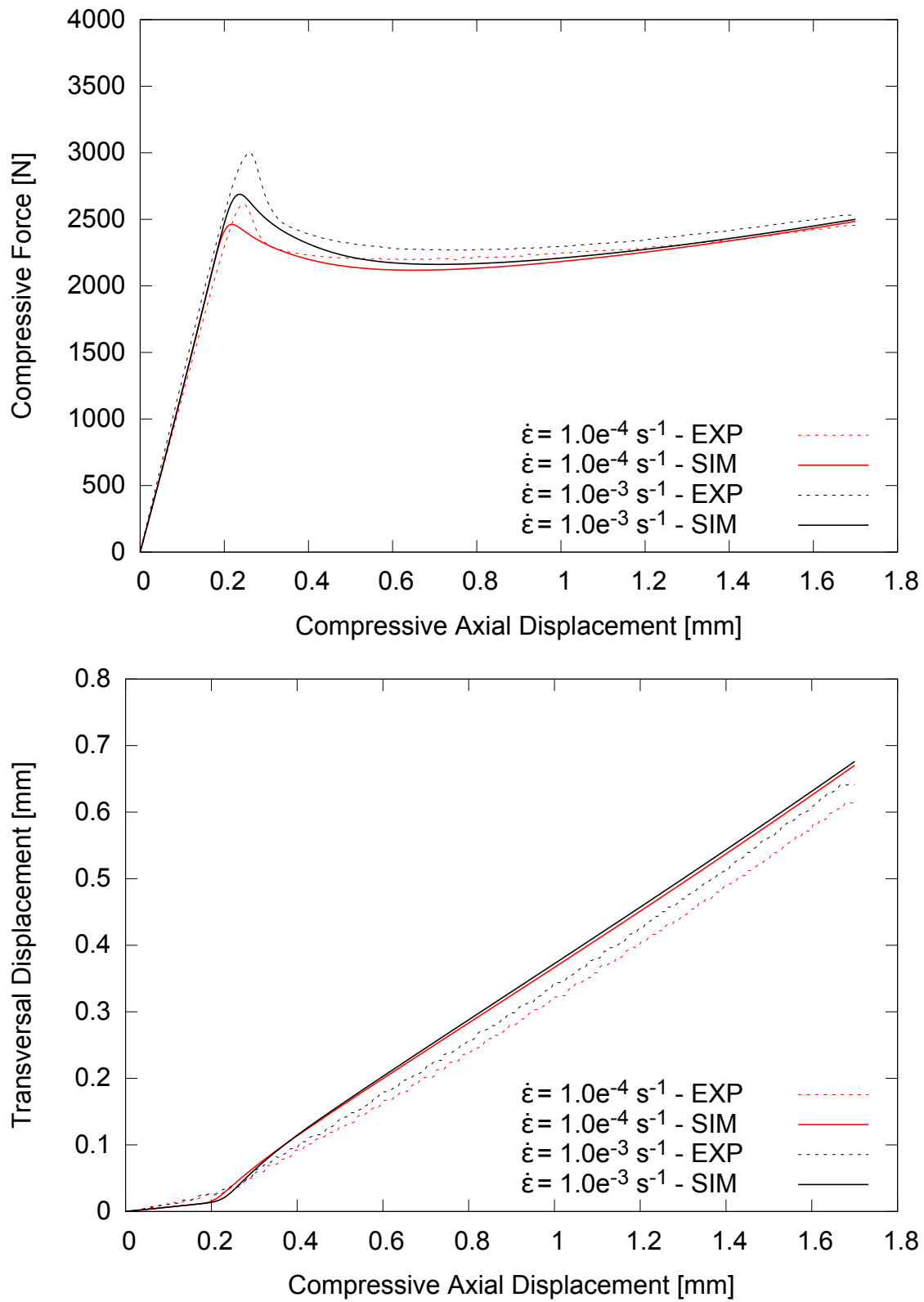


Figure 27 – FEM-based identification procedure - de Castro-Fancellò model.

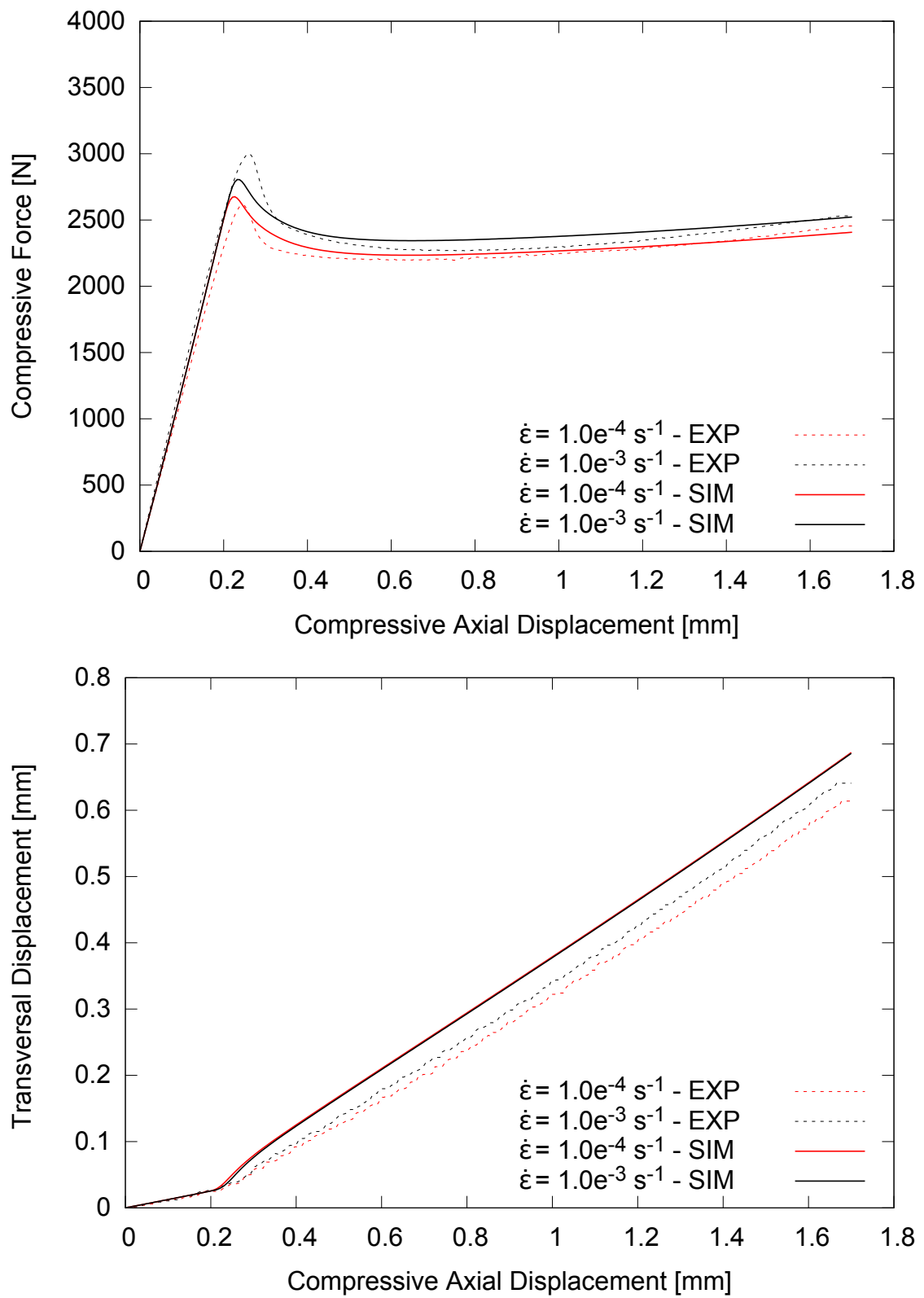
Constitutive-based identification

Figure 28 – Constitutive-based identification procedure - de Castro-Fancello model.

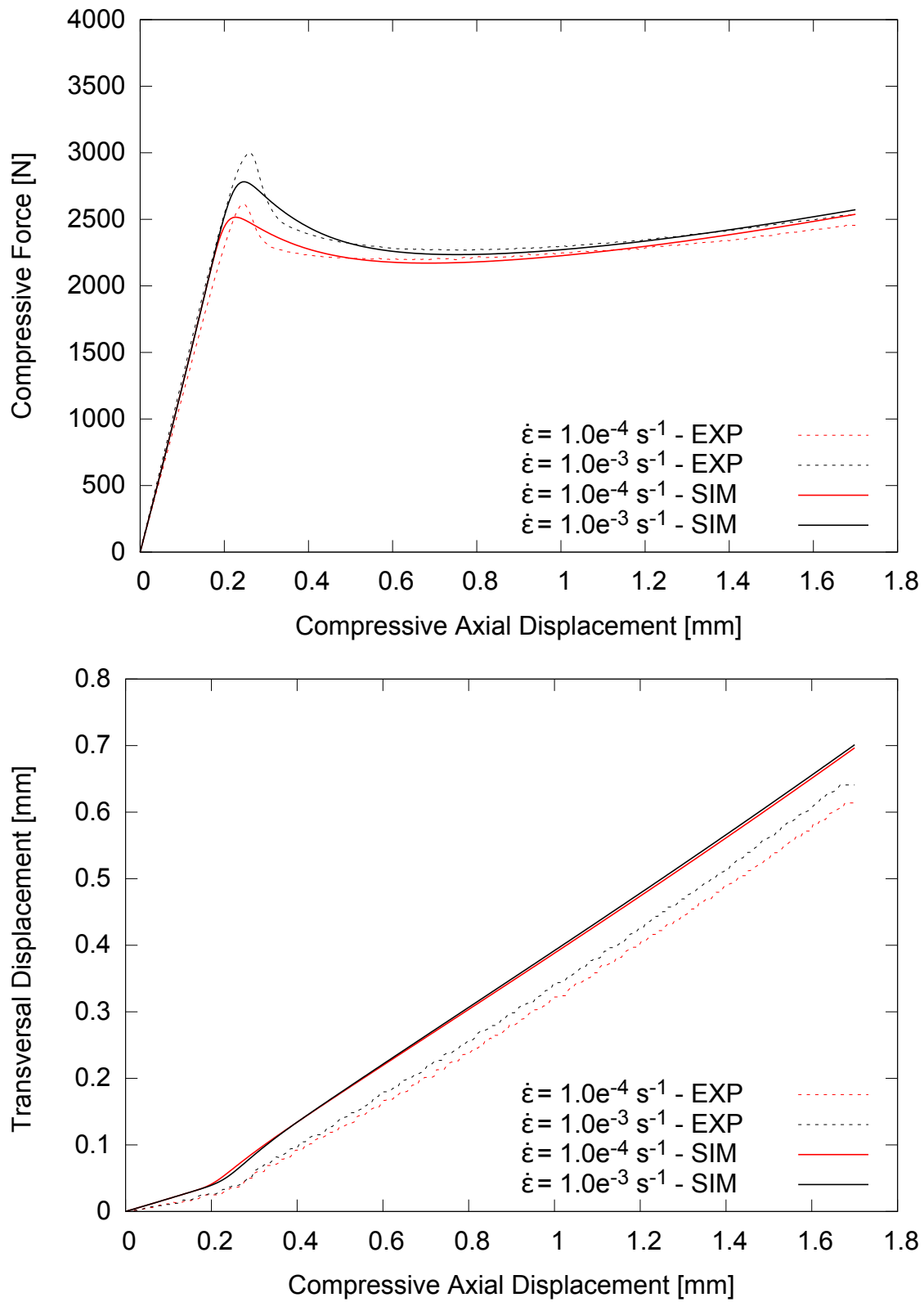
Mixed-1 identification

Figure 29 – Mixed-1 identification procedure - de Castro-Fancello model.

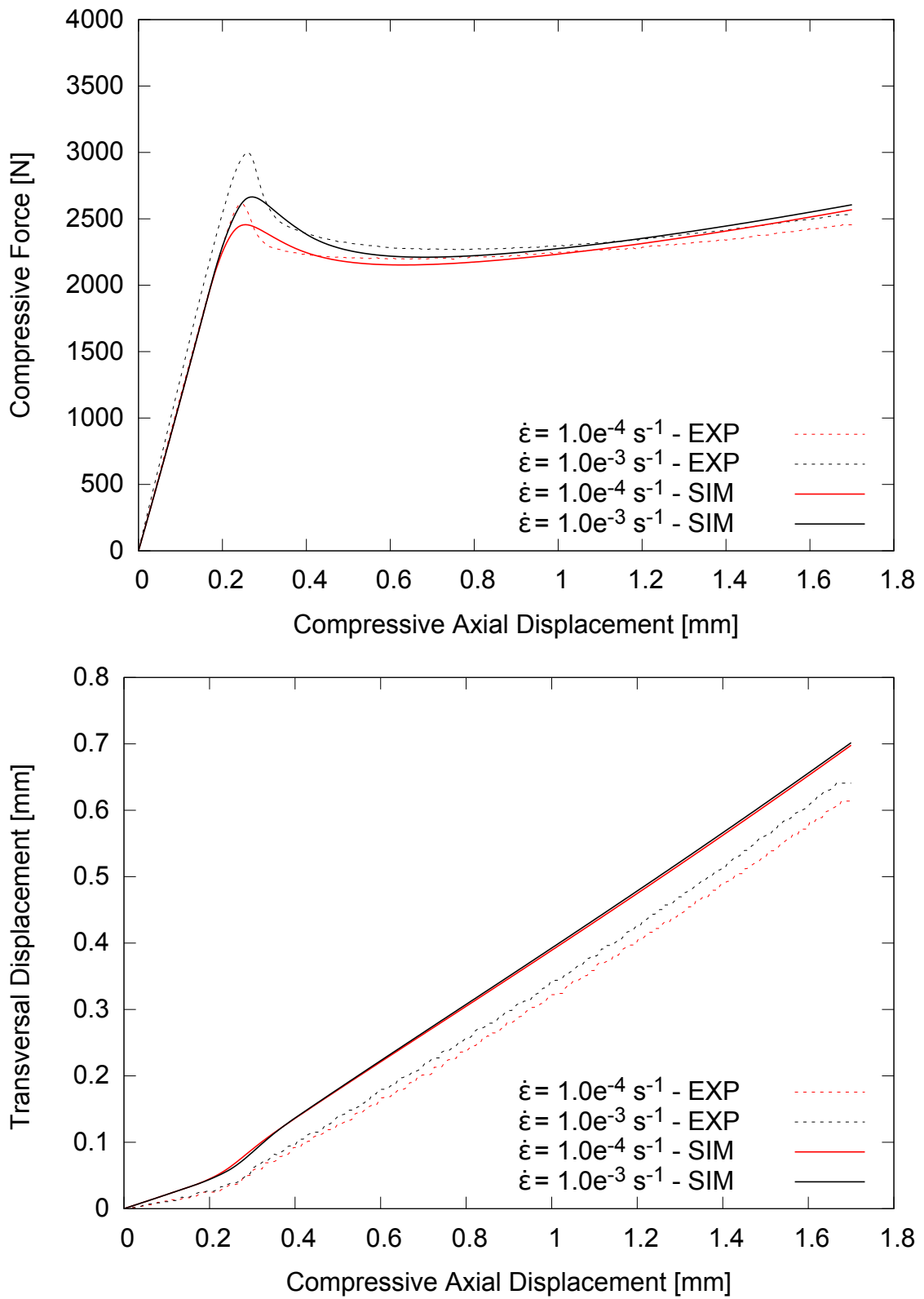
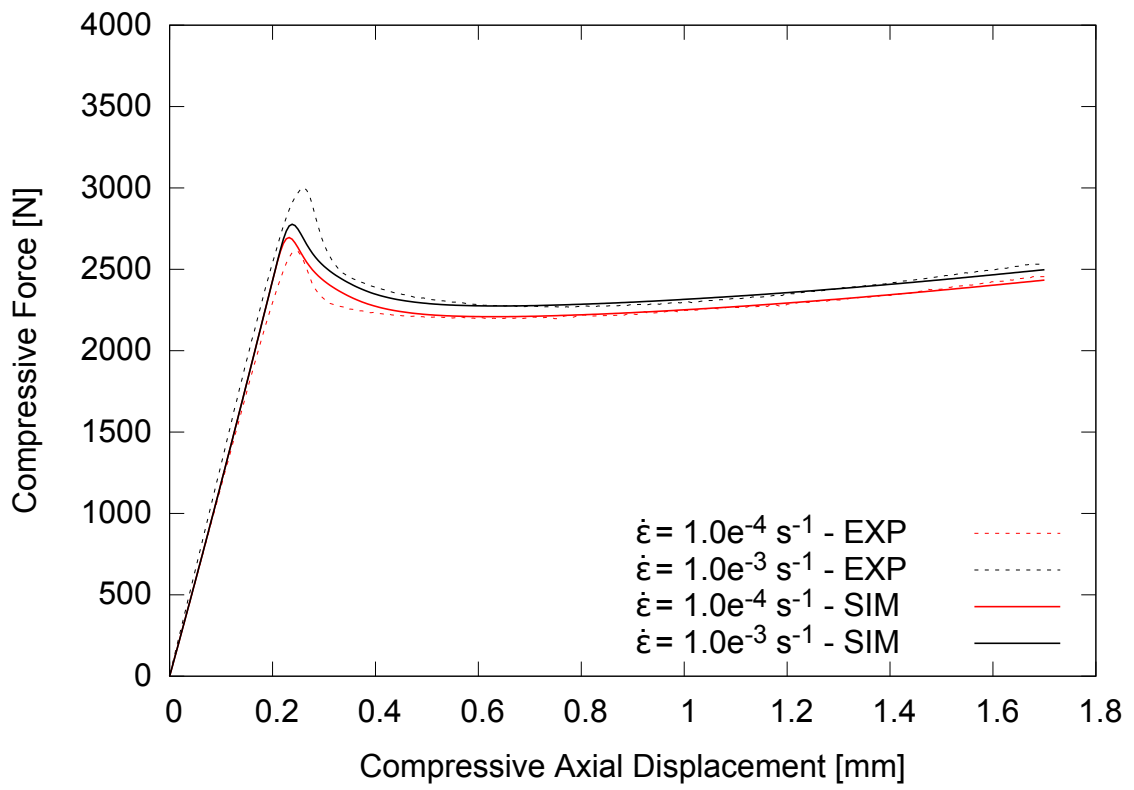
Mixed-2 identification

Figure 30 – Mixed-2 identification procedure - de Castro-Fancelllo model.

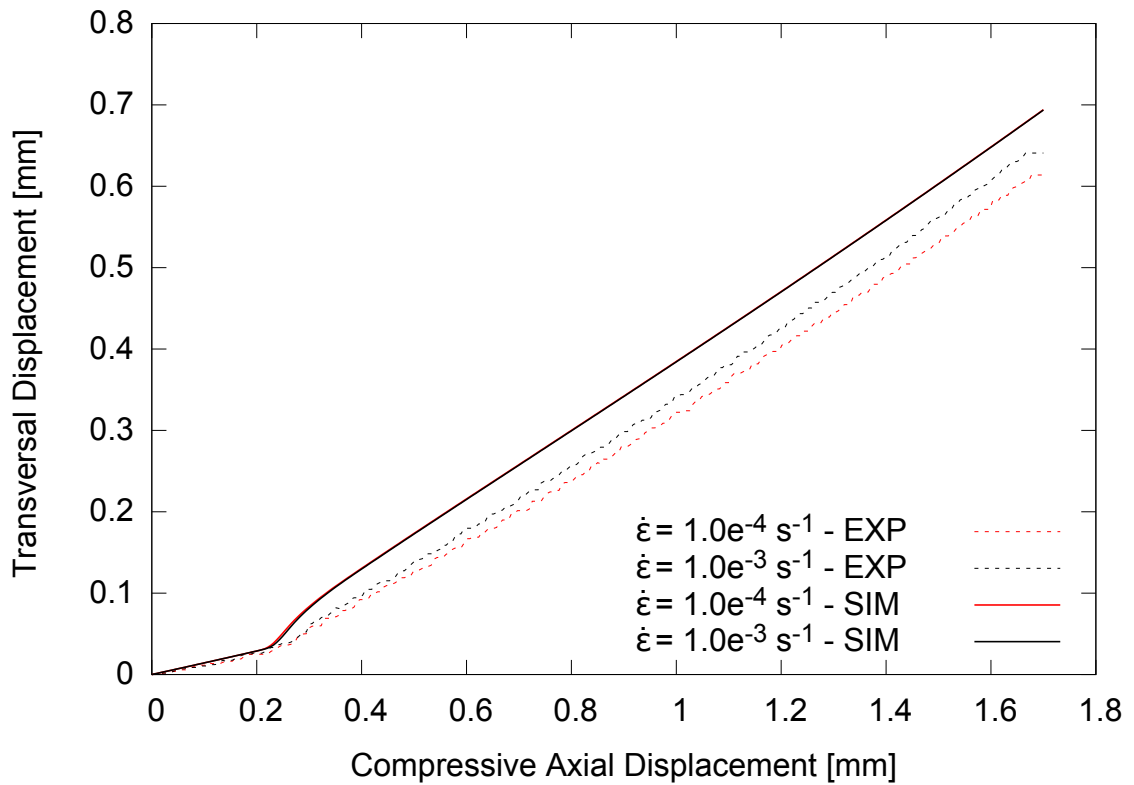
5.2 FSF MODEL

Figures from 31 to 34 show the calibrated FSF model to the experimental data obtained from compression test of PLGA. The calibrated model is represented by continuous lines and the experimental results by dashed lines. Table 10 presents the resulting set of identified parameters for each identification process and Table 12 presents the computing times for each identification process.

FEM-based identification



(a)



(b)

Figure 31 – FEM-based identification procedure - Farias model.

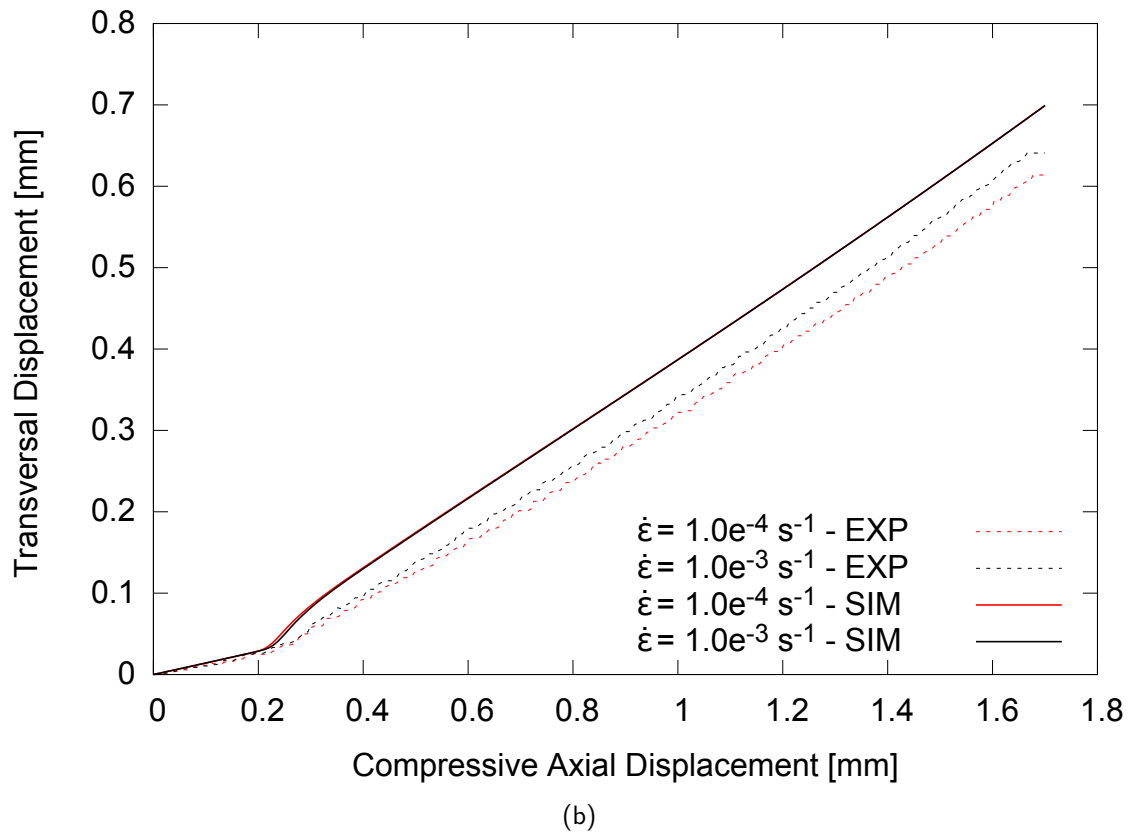
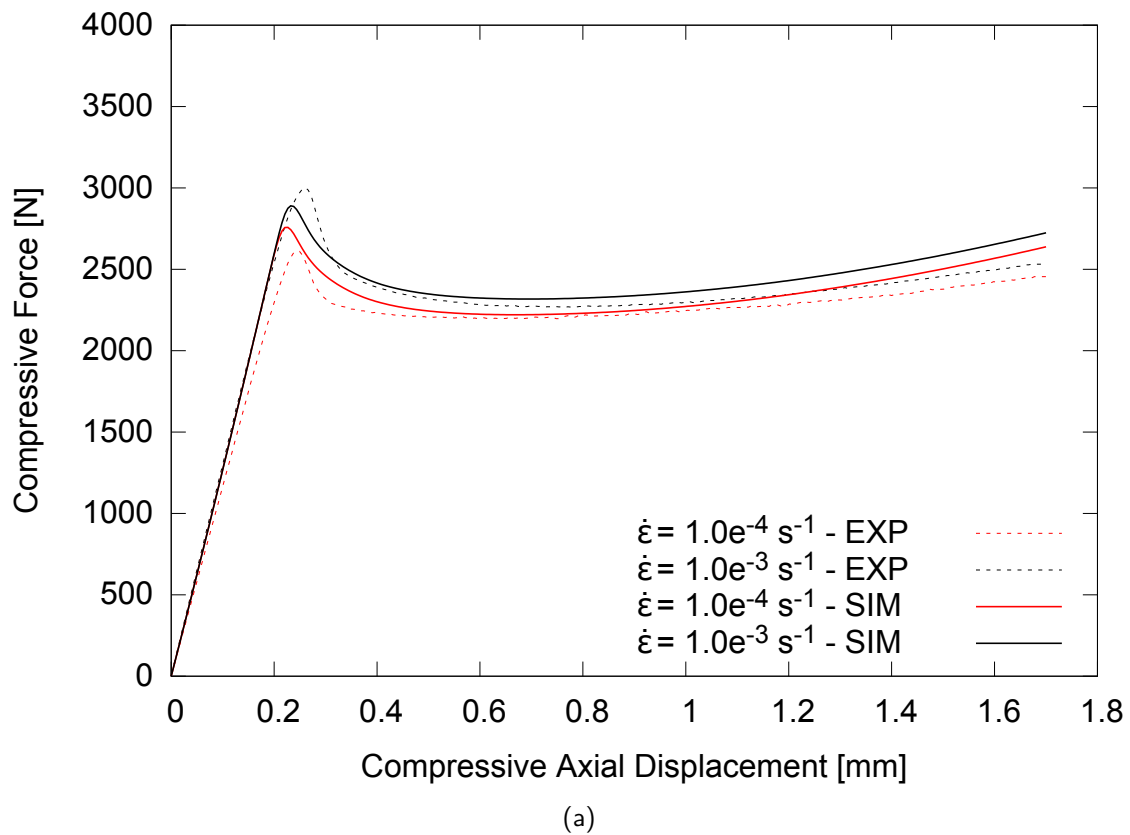
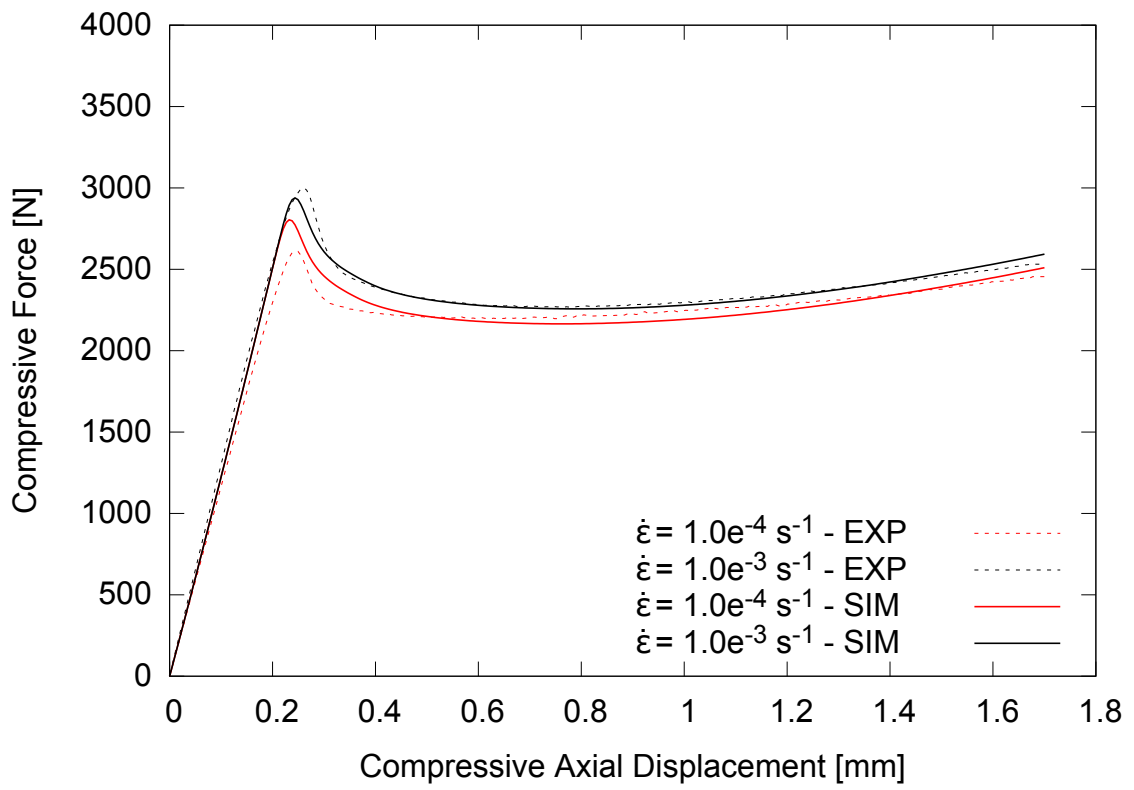
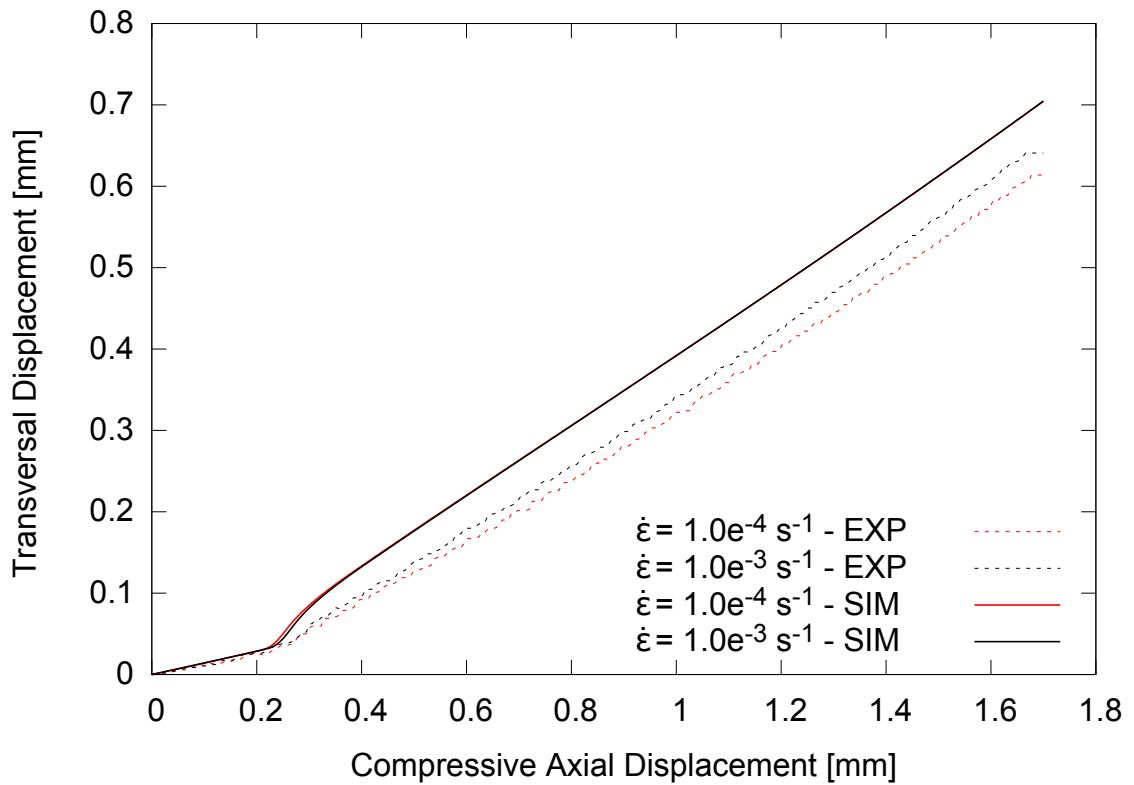
Constitutive-based identification

Figure 32 – Constitutive-based identification procedure - Farias model.

Mixed-1 identification

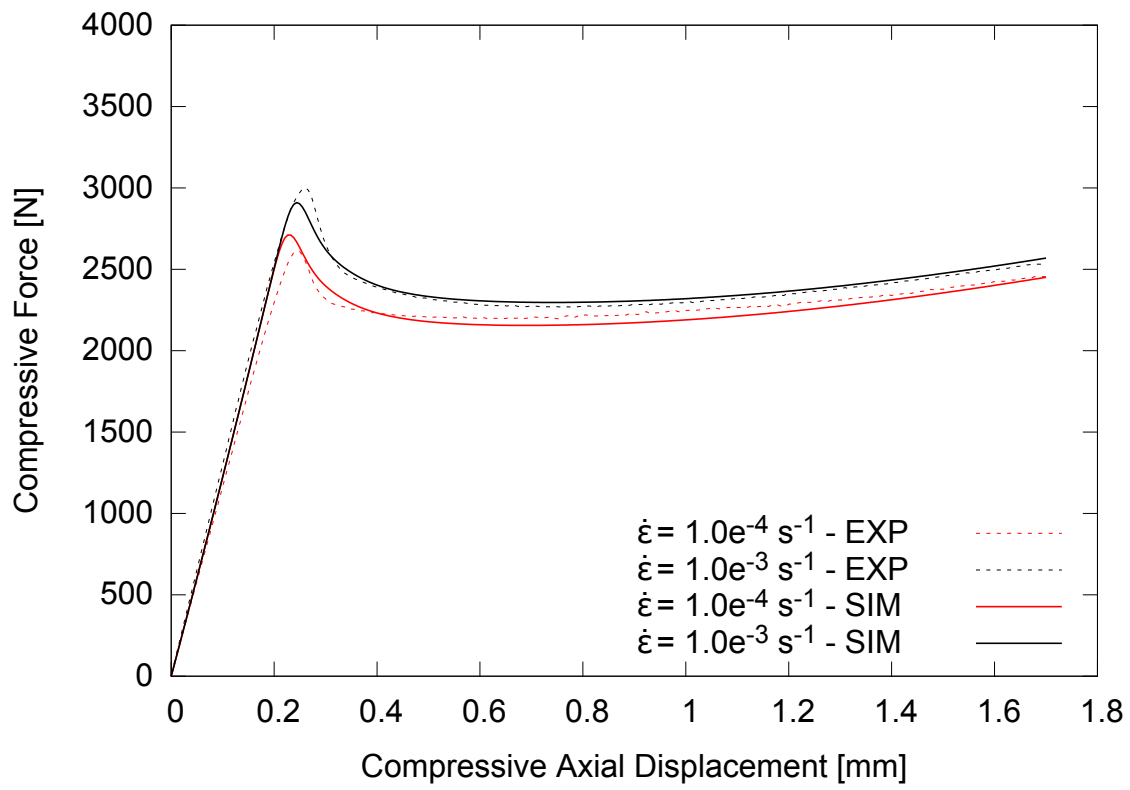
(a)



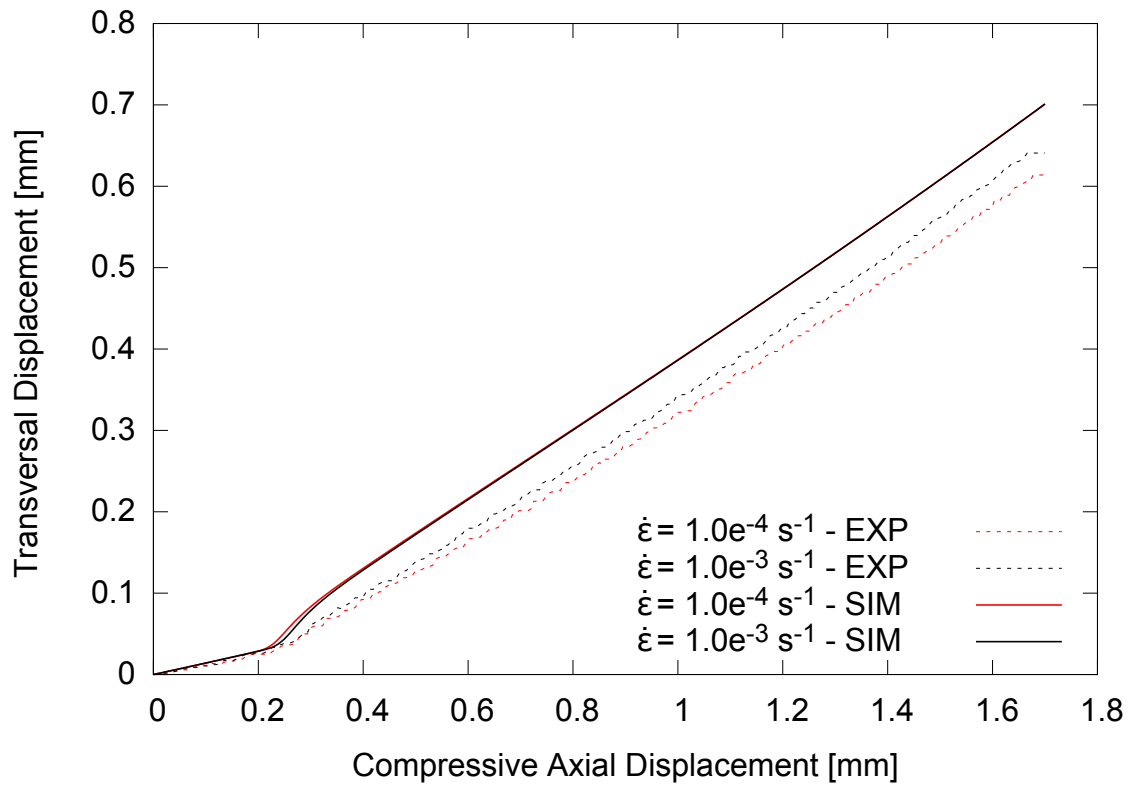
(b)

Figure 33 – Mixed-1 identification procedure - Farias model.

Mixed-2 identification



(a)



(b)

Figure 34 – Mixed-2 identification procedure - Farias model.

	FEM-based	Constitutive-based	Mixed-1	Mixed-2
μ	1098.43	948.45	886.75	779.15
K	1114.18	2459.47	2596.82	2948.76
c	0.843	36.31	42.65	69.13
η	0.148	0.118	0.136	0.122
n	2.48	10.37	6.92	0.69
Hiso	0.001	$9.60 \cdot 10^{-4}$	$9.60 \cdot 10^{-4}$	0.53
σ_{y0}	60.00	60.00	60.00	60.00
S0	66.35	113.34	134.17	61.90
Scv	3.57	18.14	10.63	13.02
Sg	106.28	140.78	178.65	236.91
Sz	200.00	185.46	173.35	125.78
Sb	187.05	164.82	155.94	102.42
M(x)	11.78	13.34	16.06	11.04

Table 9 – Identified parameters for PLGA for the CF model

	FEM-based	Constitutive-based	Mixed-1	Mixed-2
G	920.98	975.76	941.75	940.42
K	1695.14	1795.96	1733.37	1730.92
μ	6.06	17.40	17.15	18.44
λ	33.94	5.52	19.51	21.66
m	0.012	0.020	0.020	0.030
S0	59.32	63.89	65.24	68.72
Scv	8.57	18.17	22.42	12.65
Sg	20.45	15.38	13.42	21.68
Sz	10.55	11.62	15.42	12.86
Sb	10.08	10.12	13.12	11.60
M(x)	11.43	19.46	10.45	11.30

Table 10 – Identified parameters for PLGA for the FSF model

	FEM-base	Constitutive-based	Mixed-1	Mixed-2
PSO-CM	—	0536.65	536.65	00333.72
NM-CM	—	0071.46	071.46	00338.28
PSO-FEA	308649.90	—	—	03592.30
NM-FEA	278919.92	—	12991.00	07260.03
Total	897569.80	608.11	13599.11	11525.33

Table 11 – Time for each identification process (seconds)

	FEM-base	Constitutive-based	Mixed-1	Mixed-2
PSO-CM	—	18.21	018.21	17.54
NM-CM	—	03.70	003.70	03.40
PSO-FEA	216803.16	—	—	59270.20
NM-FEA	23534.23	—	3070.00	02668.43
Total	240337.40	21.91	3091.30	61938.64

Table 12 – Time for each identification process (seconds)

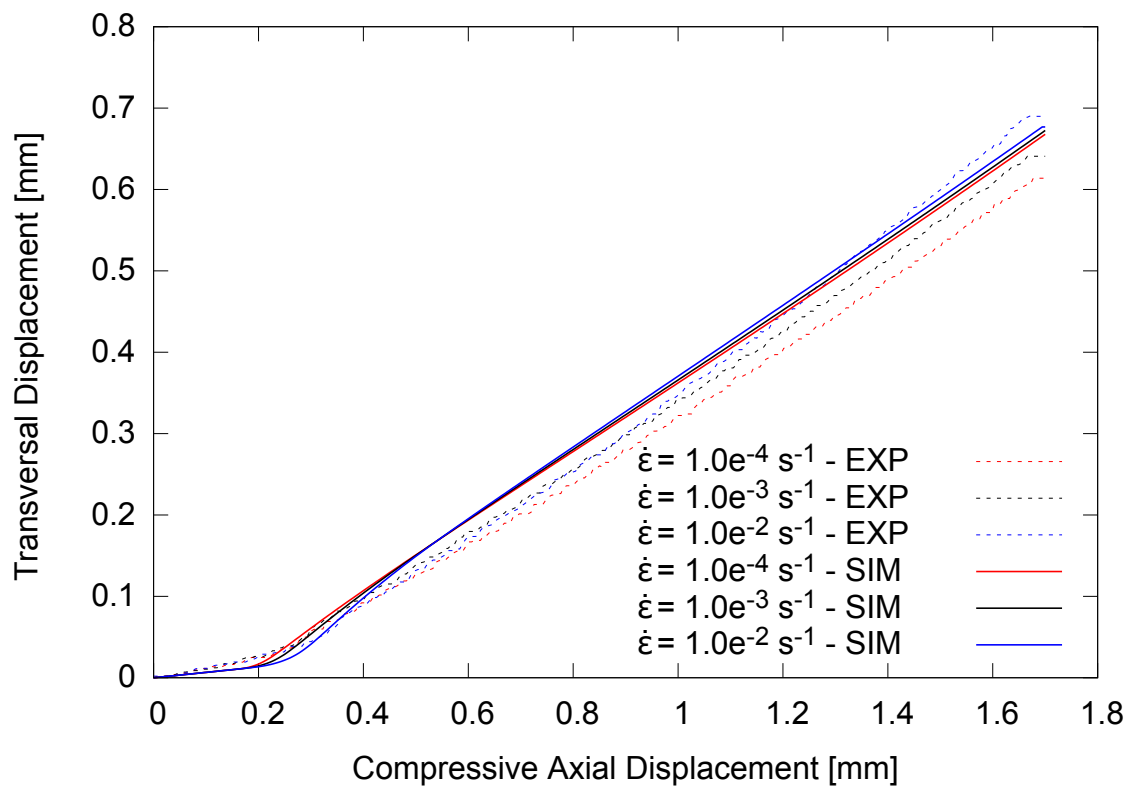
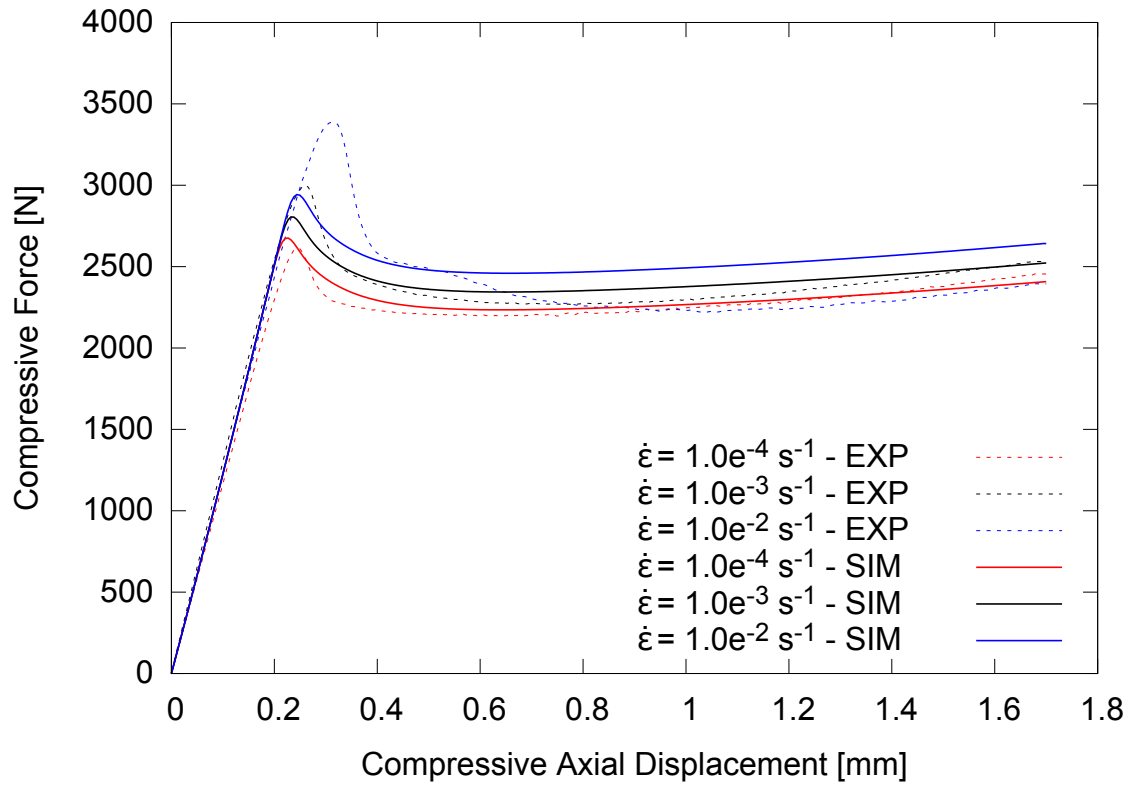
5.3 COMPLEMENTARY RESULTS

In this section it is shown the capabilities of the models and identified parameters to predict the behavior of the material under other conditions than they were identified for. The identified parameters were to simulate the non-homogeneous uniaxial compression test under the high strain rate ($1.0 \times 10^{-2}s$). Figures from 35 to 42 show the force, transversal displacement and volume responses for each set of identified parameters.

It can be observed that the high strain rate simulate curve, shown in blue, follows the trend from the other simulated strain rates responses. However, as it was expected, the high strain rate response is not capable of displaying the secondary softening nor the continuous loss in volume from 0.2 to 0.6mm. Once again, the choice of identification procedure does not seem to affect significantly the responses for the same constitutive model. These complementary results reinforce the need of even more sophisticated models to simulate these complex behaviors.

5.4 CF MODEL

FEM-based identification



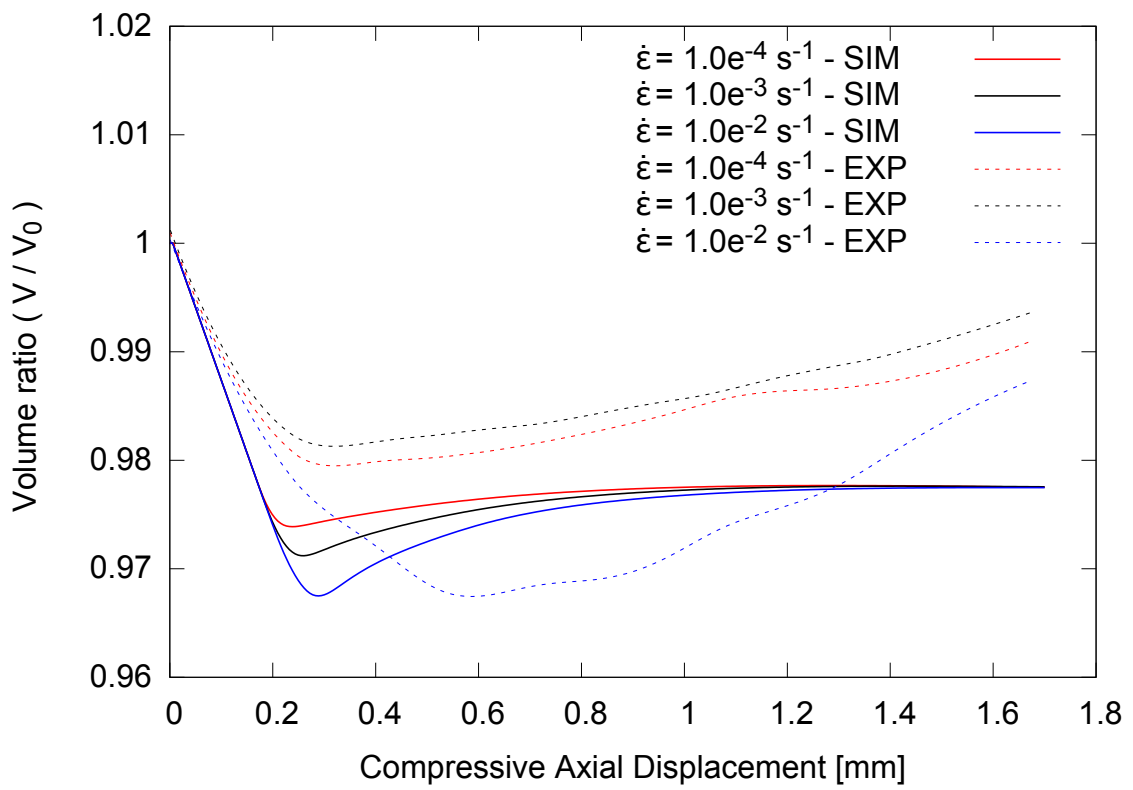
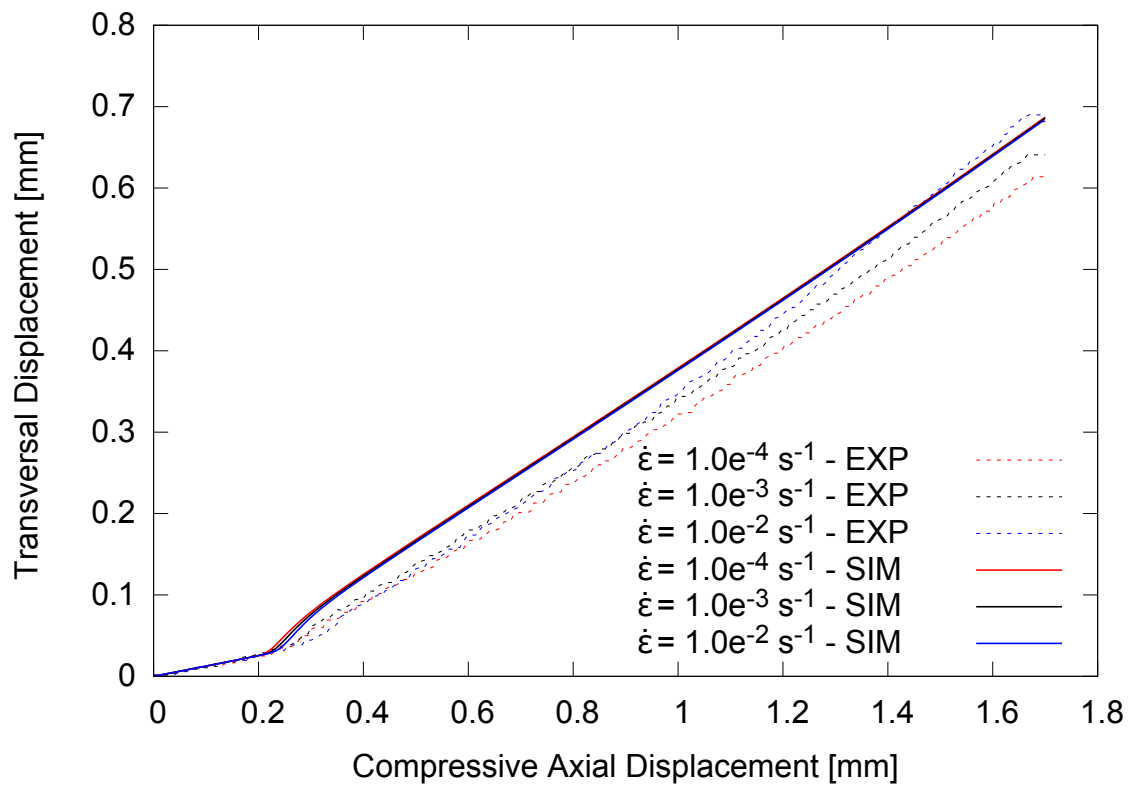
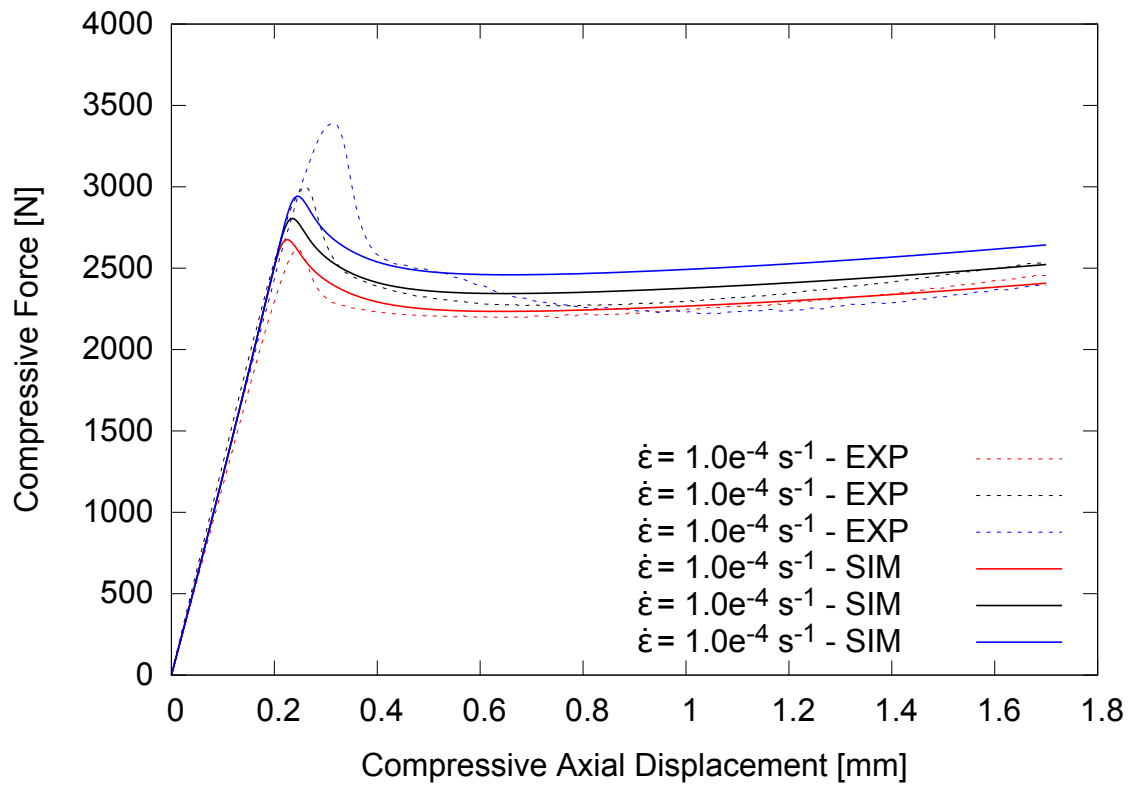


Figure 35 – FEM-based identification procedure - de Castro-Fancello model.

Constitutive-based identification

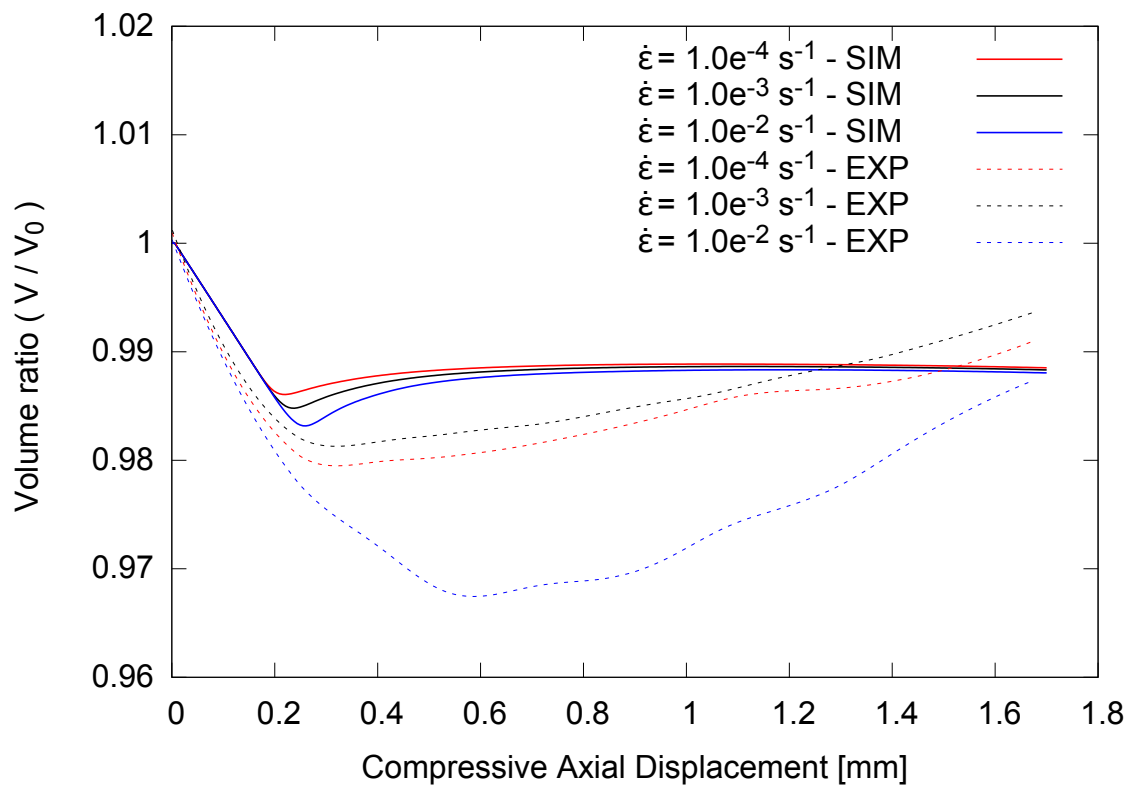
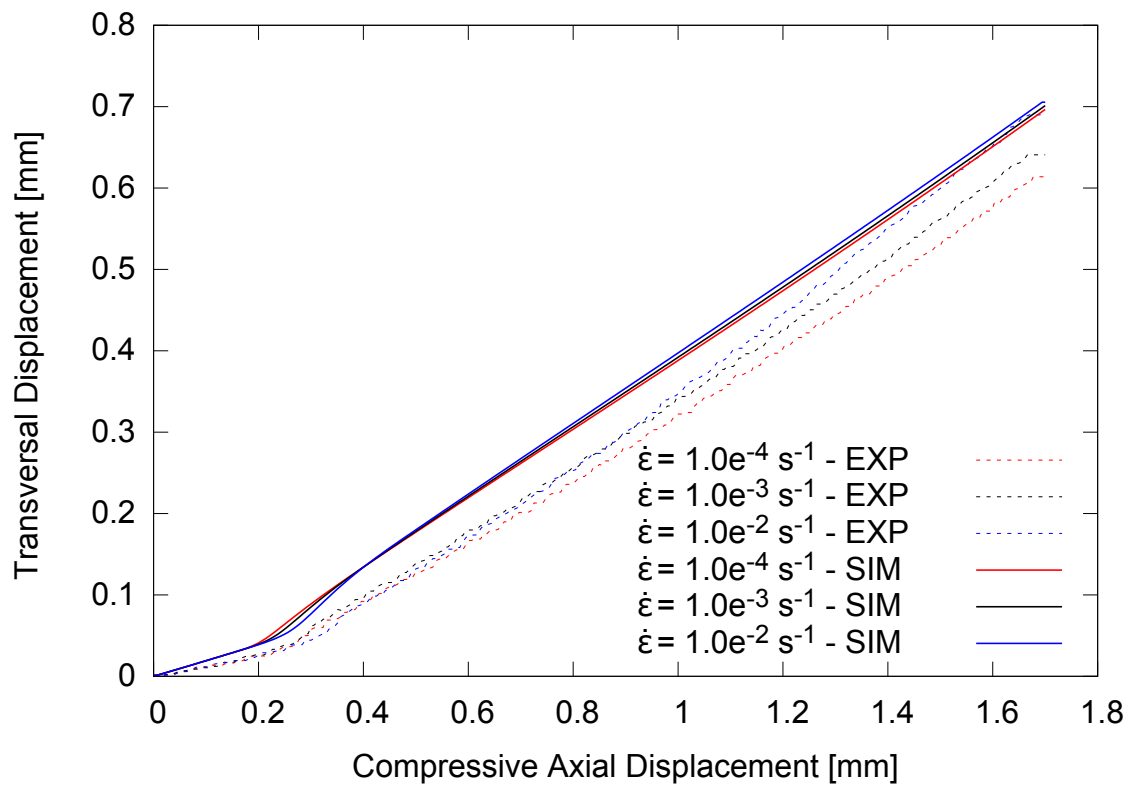
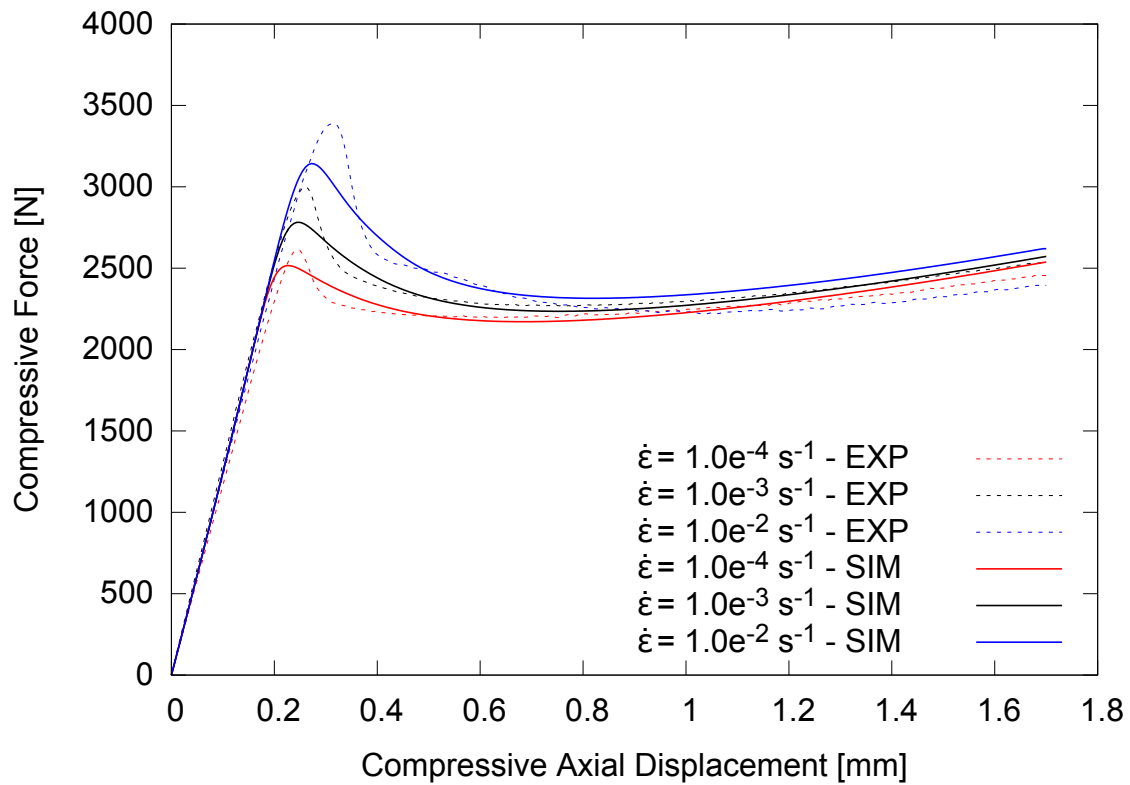


Figure 36 – Constitutive-based identification procedure - de Castro-Fancello model.

Mixed-1 identification



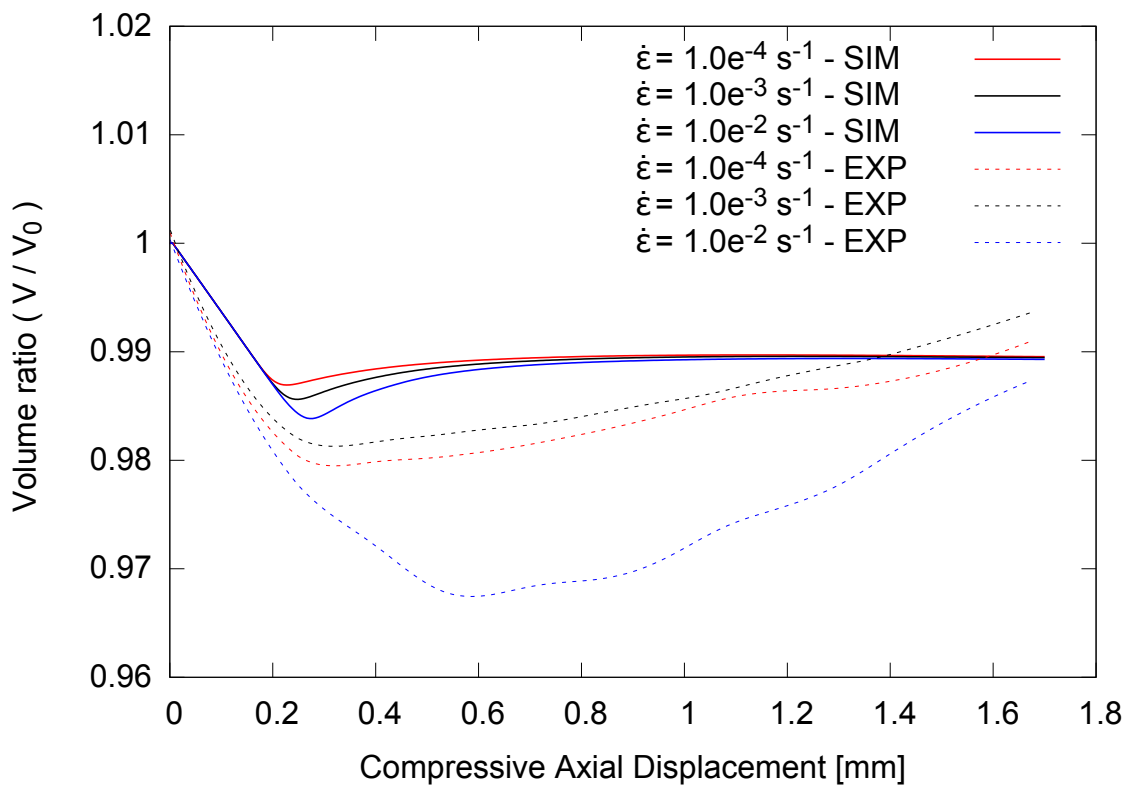
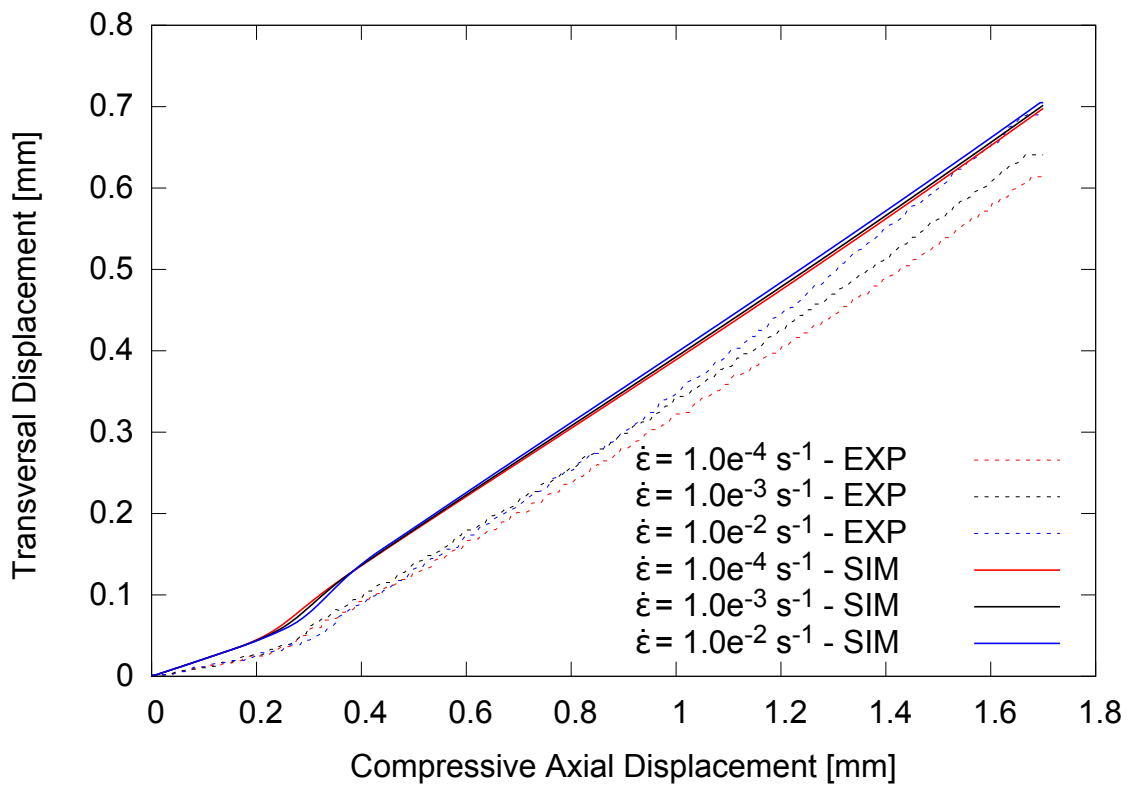
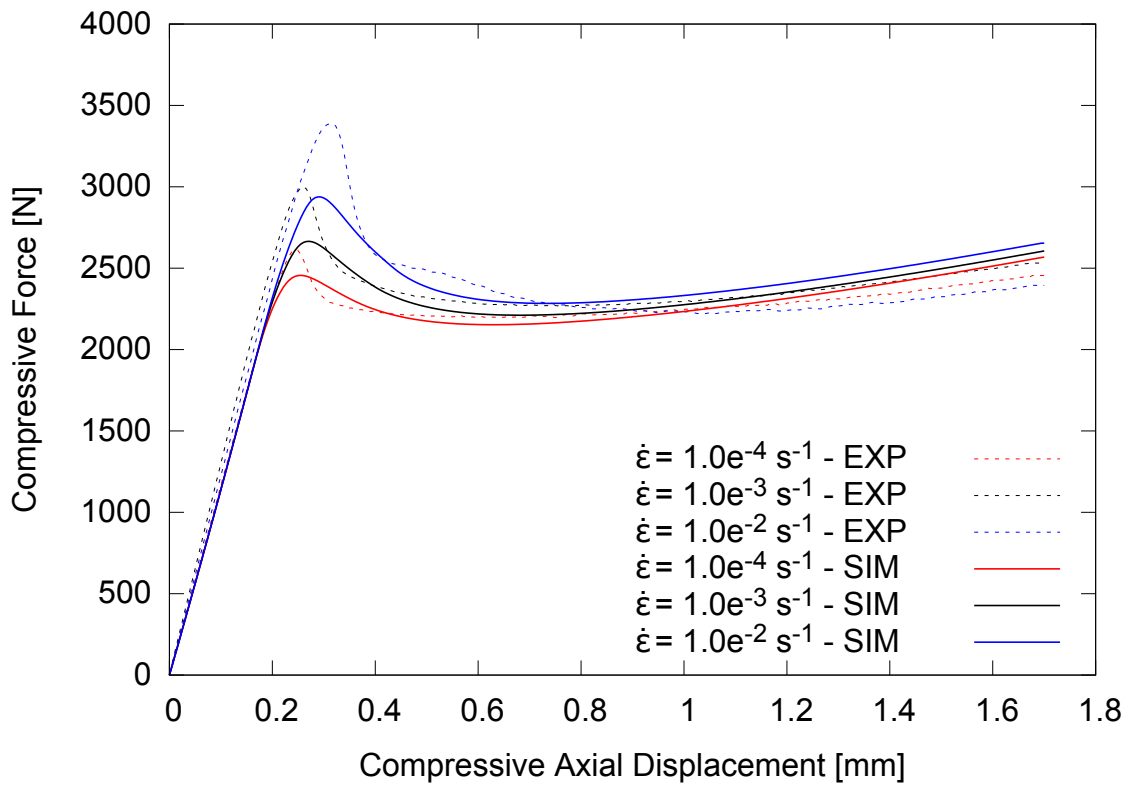


Figure 37 – Mixed-1 identification procedure - de Castro-Fancelllo model.

Mixed-2 identification



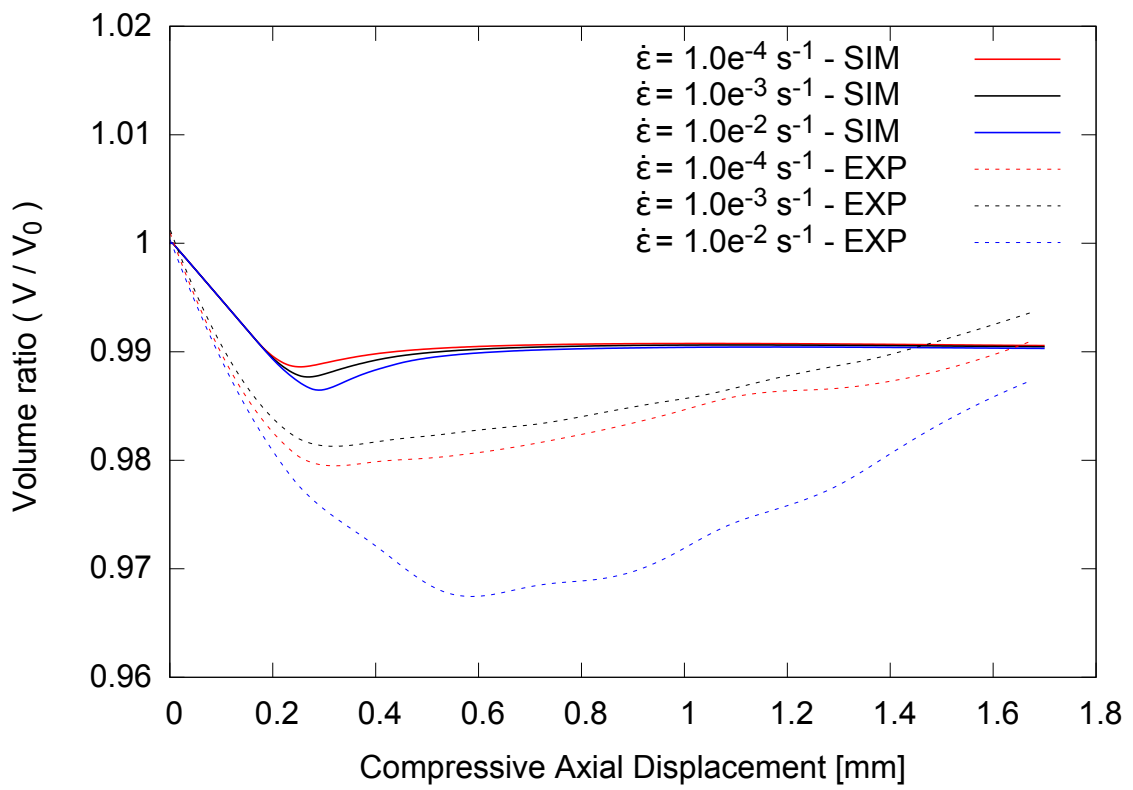
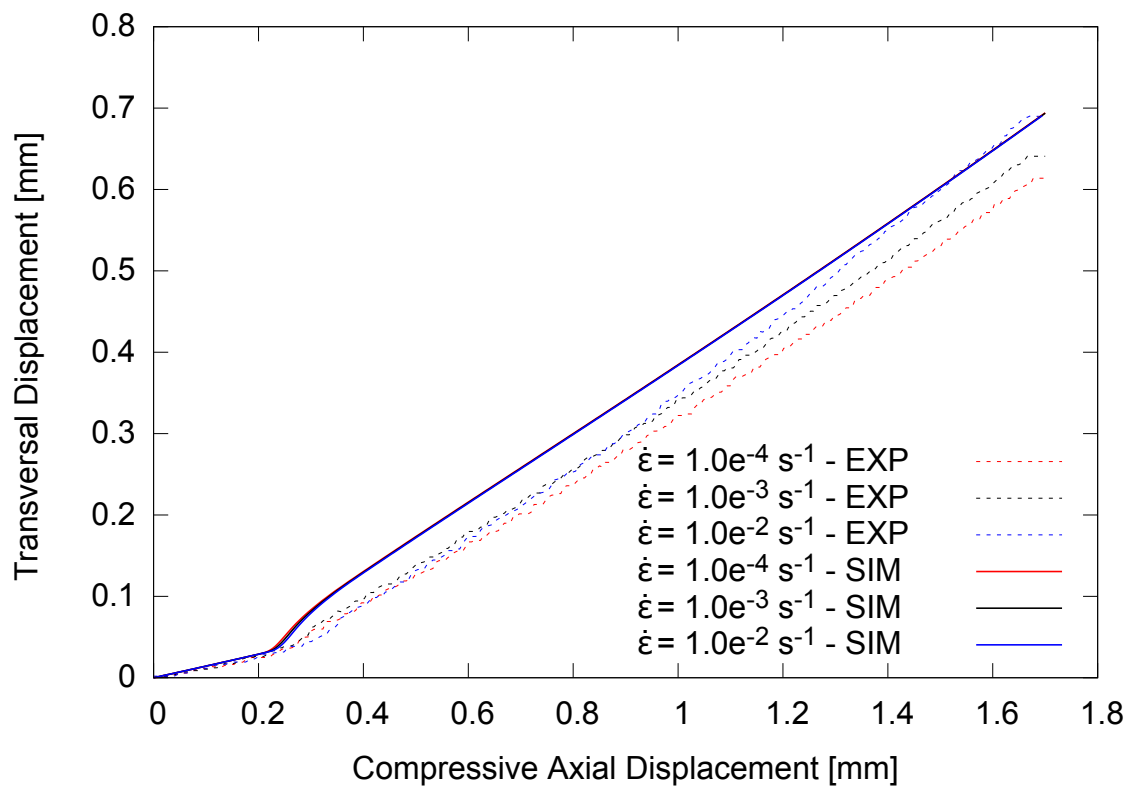
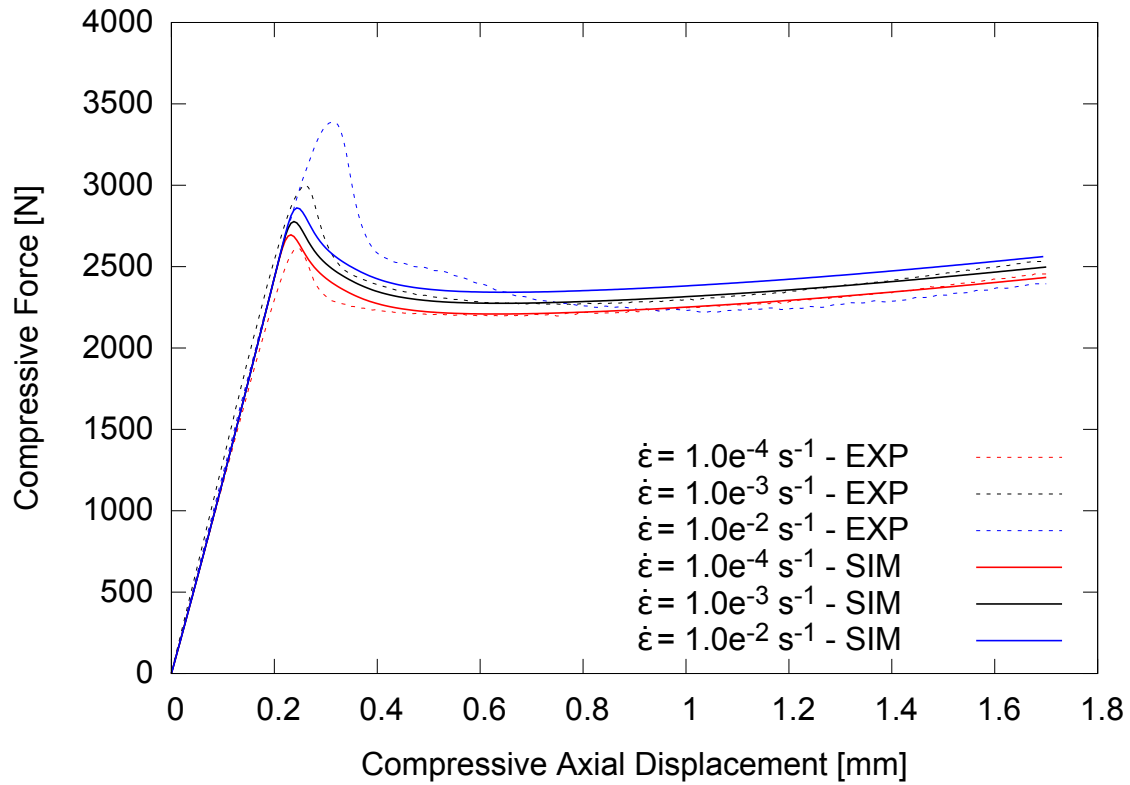


Figure 38 – Mixed-2 identification procedure - de Castro-Fancelllo model.

5.5 FSFM MODEL

FEM-based identification



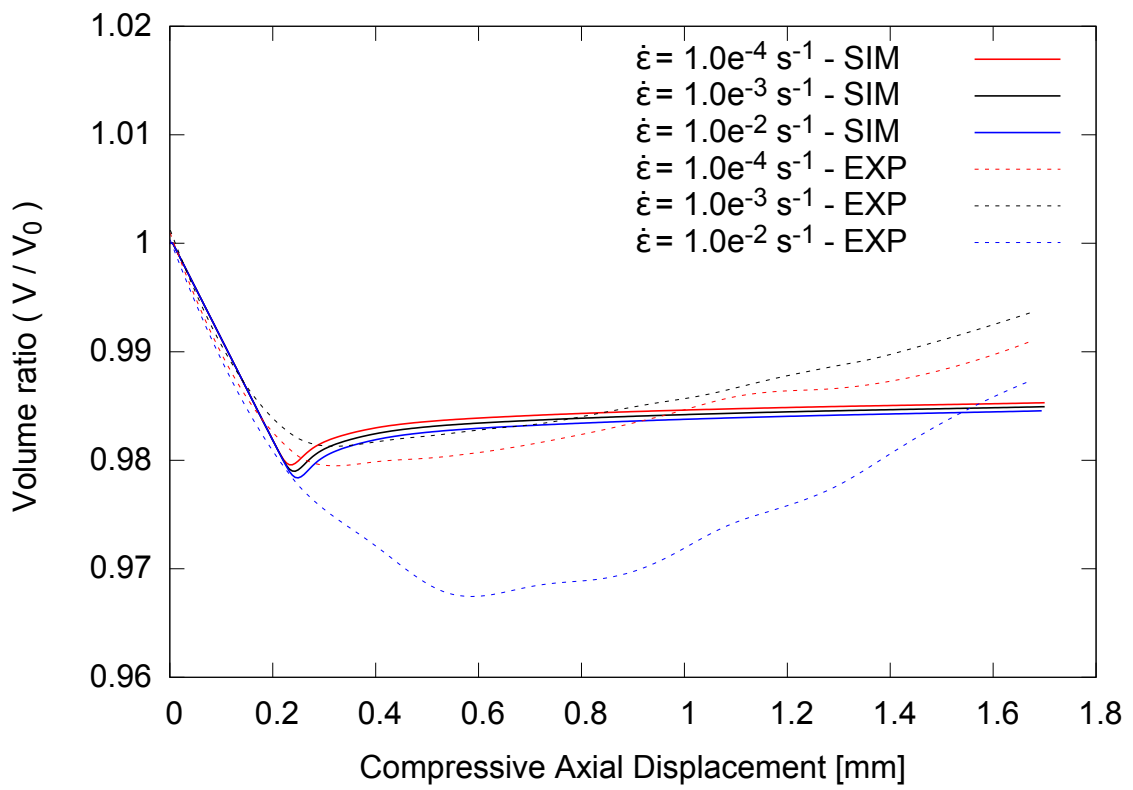
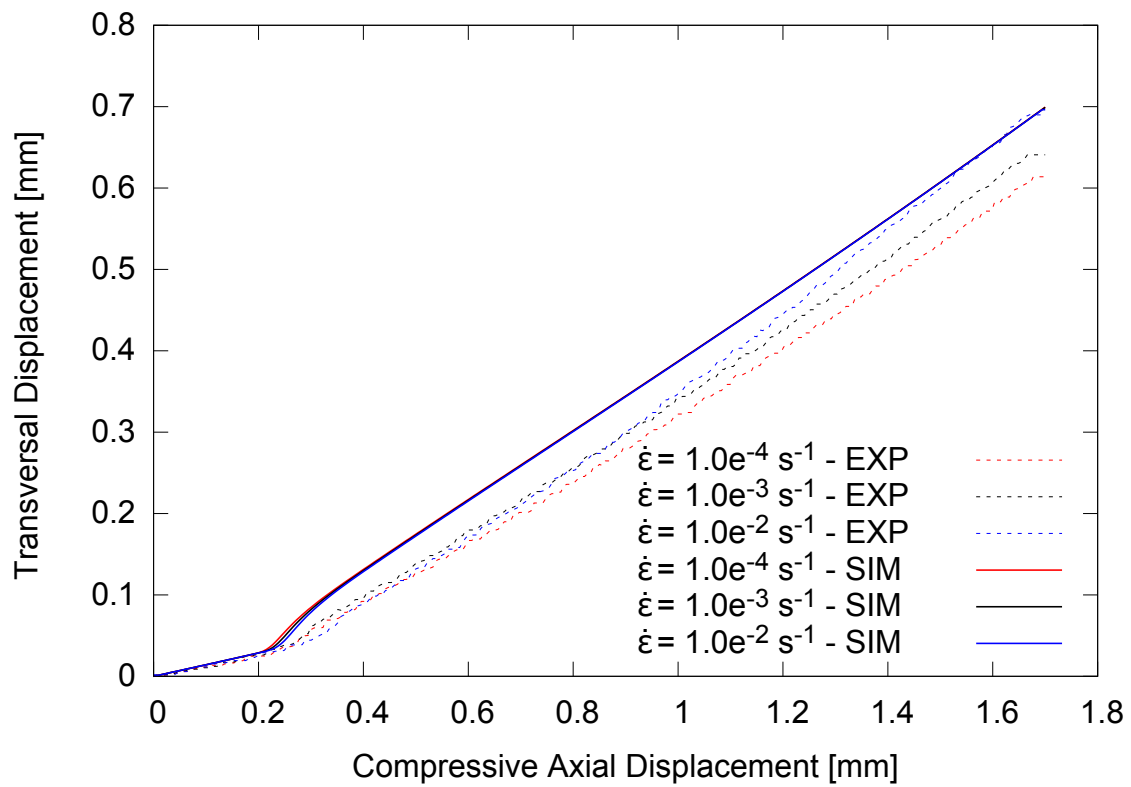
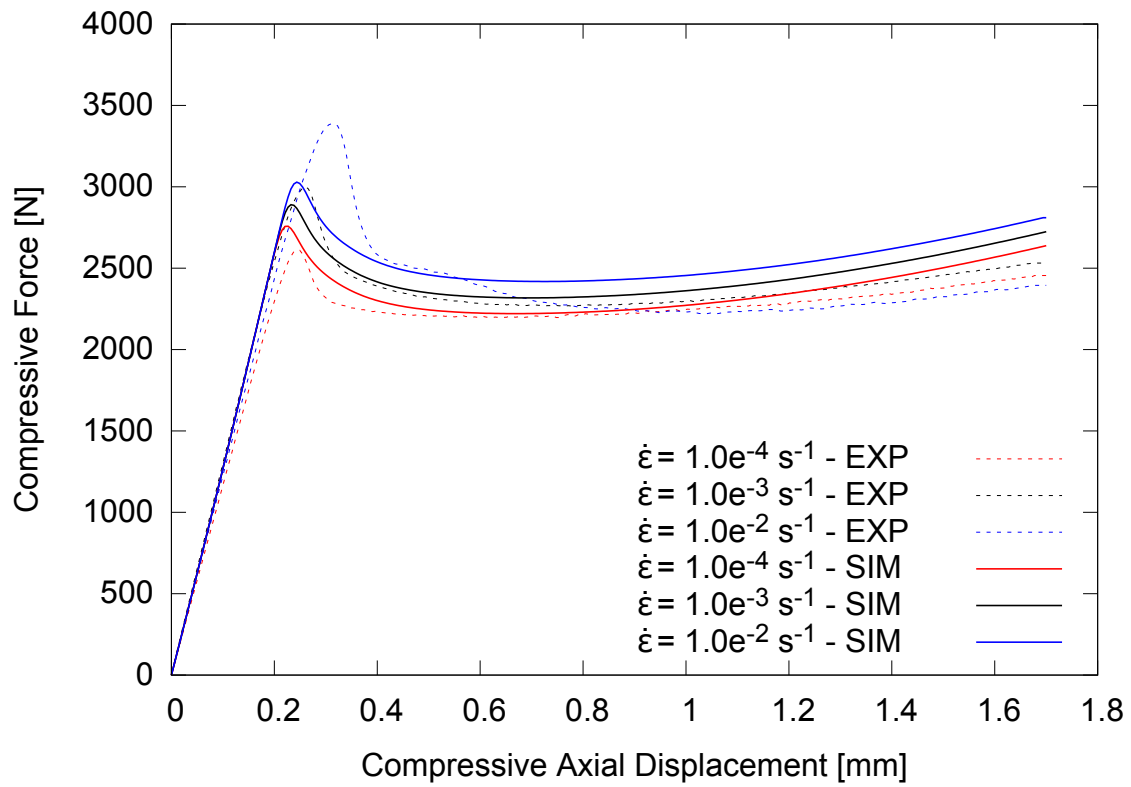


Figure 39 – FEM-based identification procedure - Farias model.

Constitutive-based identification

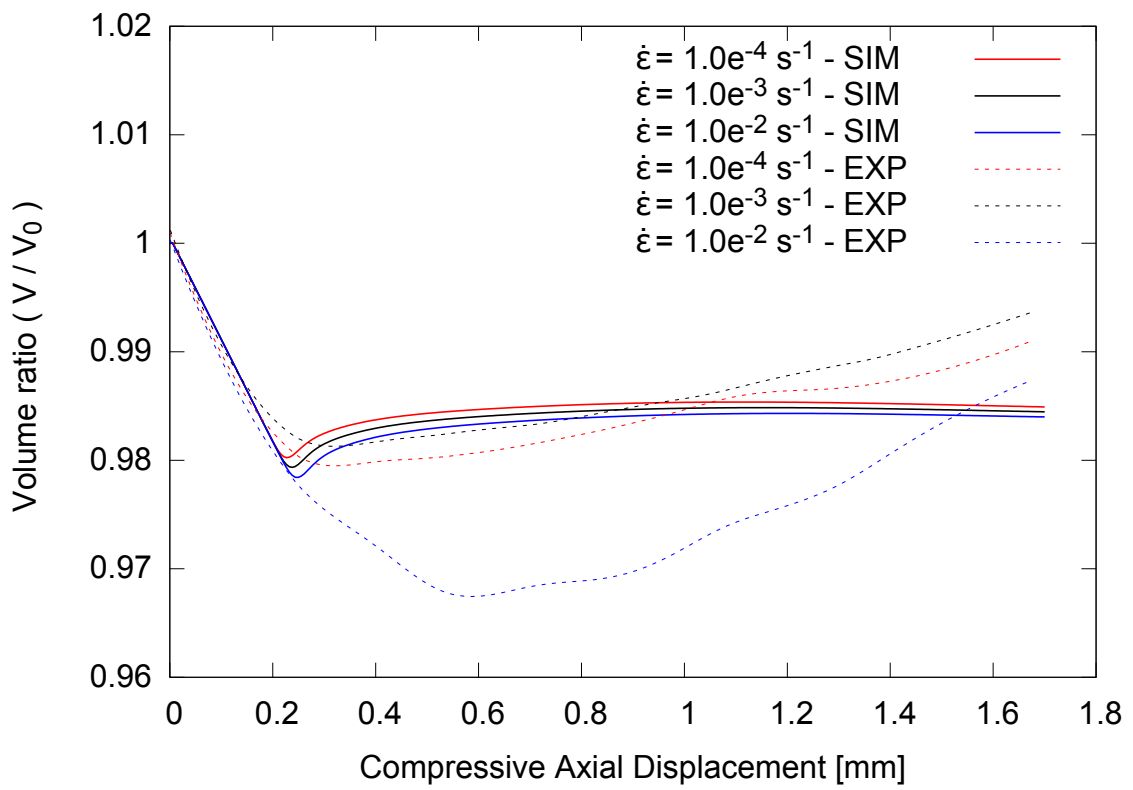
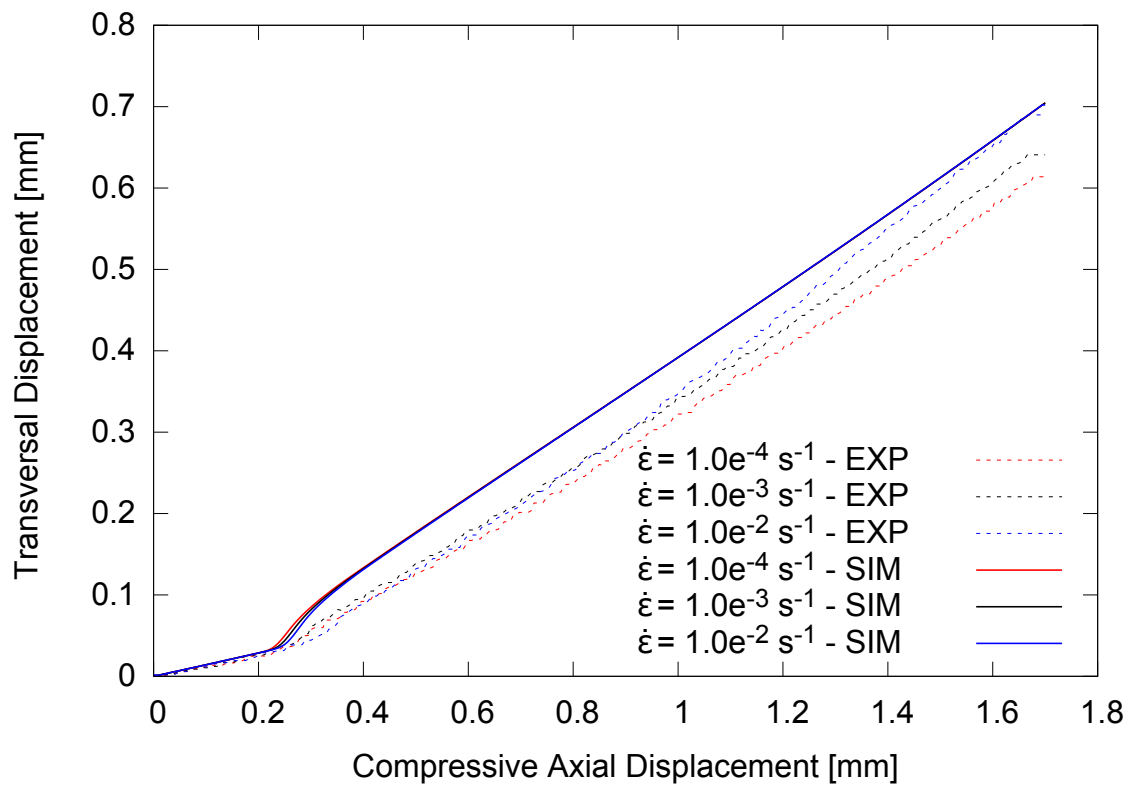
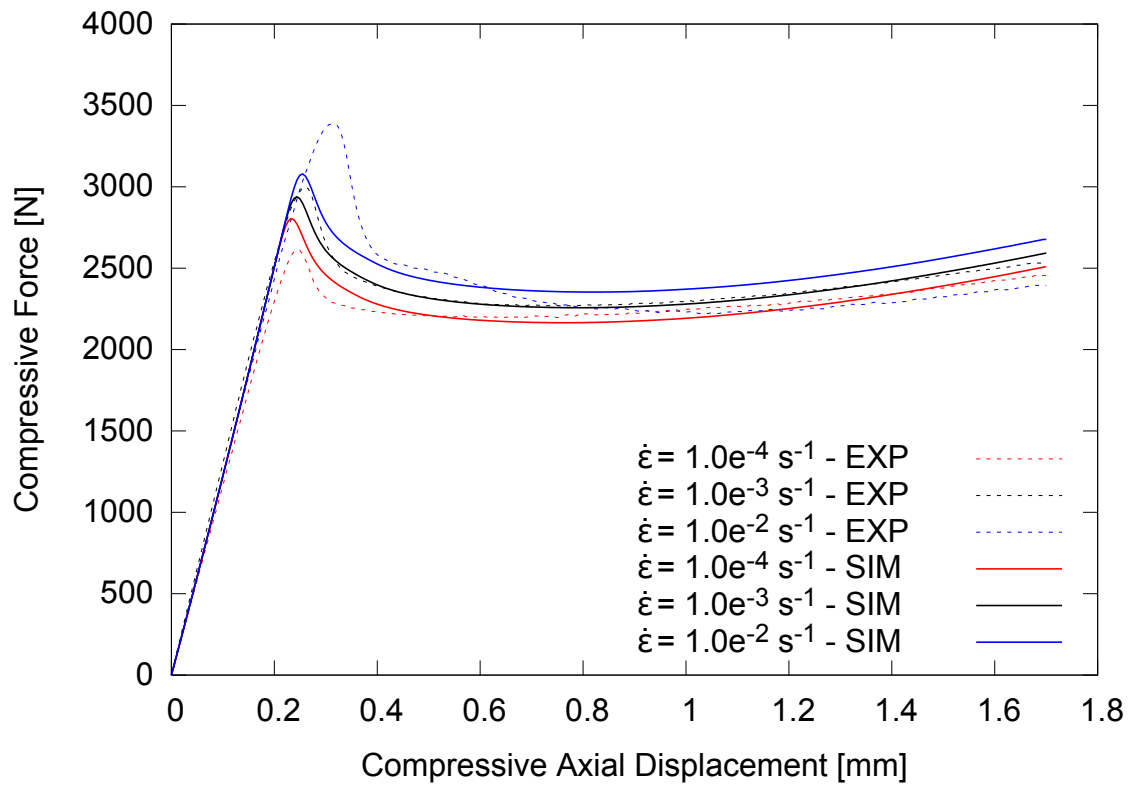


Figure 40 – Constitutive-based identification procedure - Farias model.

Mixed-1 identification



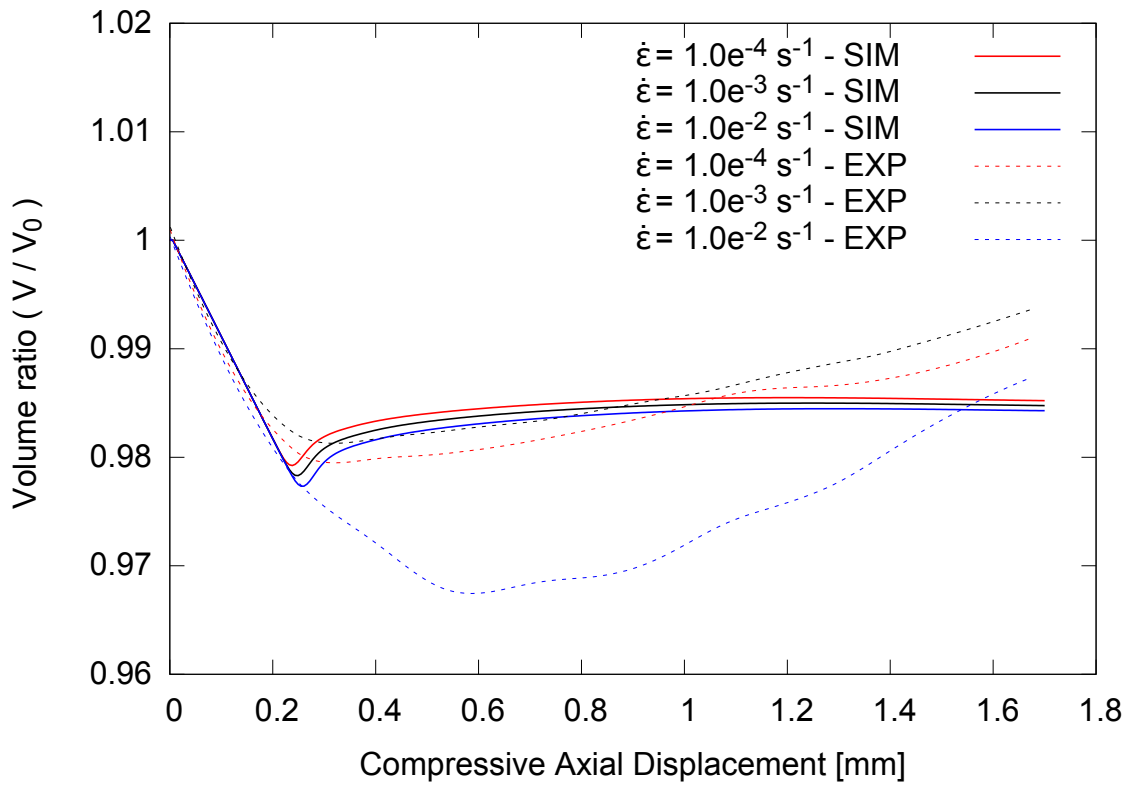
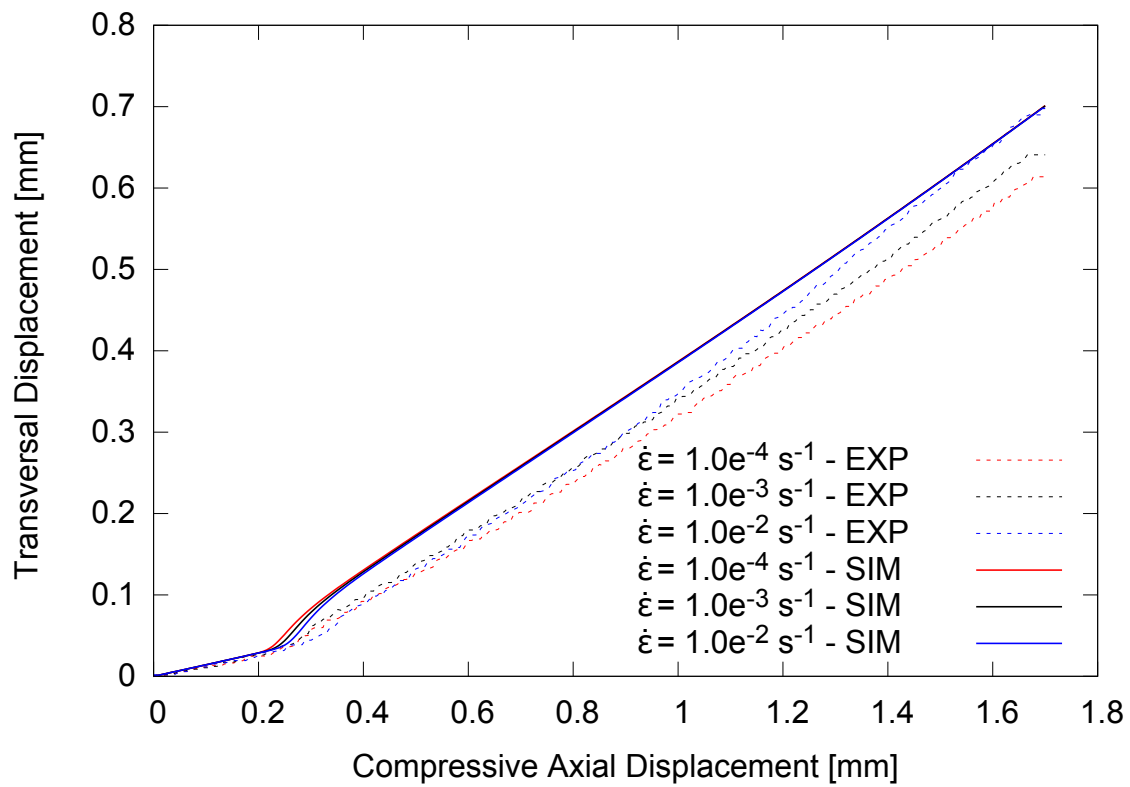
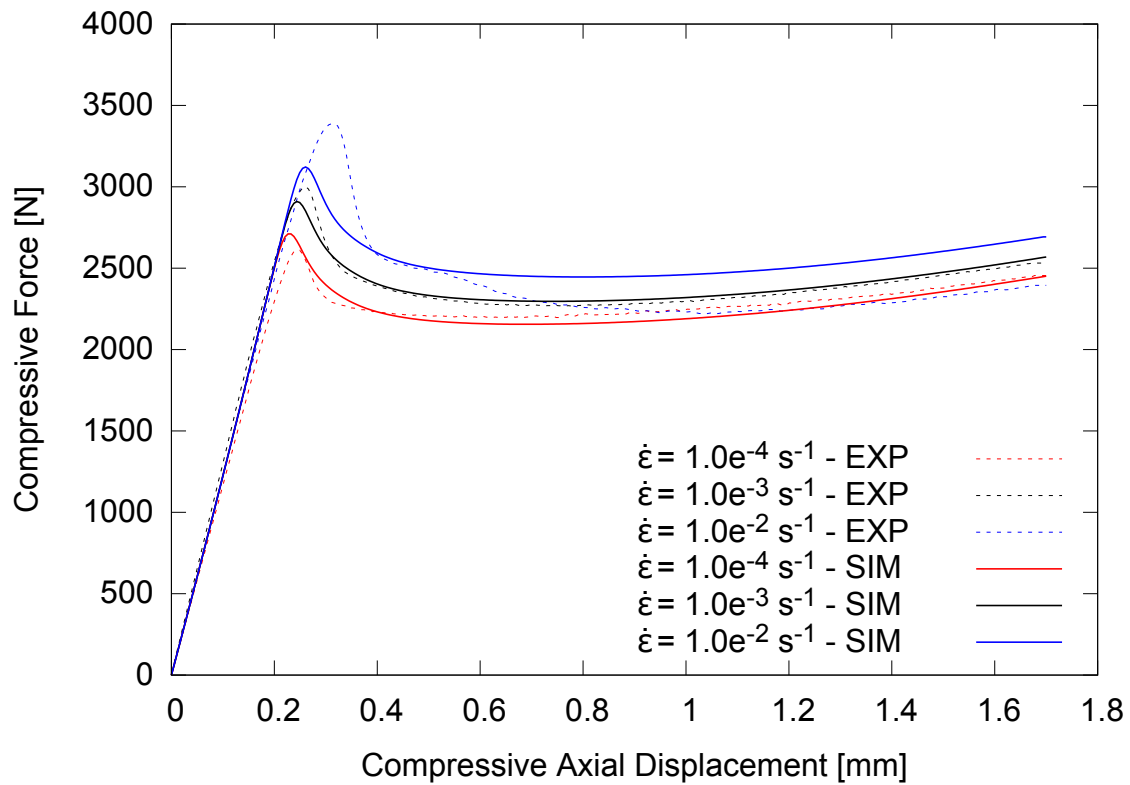


Figure 41 – Mixed-1 identification procedure - Farias model.

Mixed-2 identification



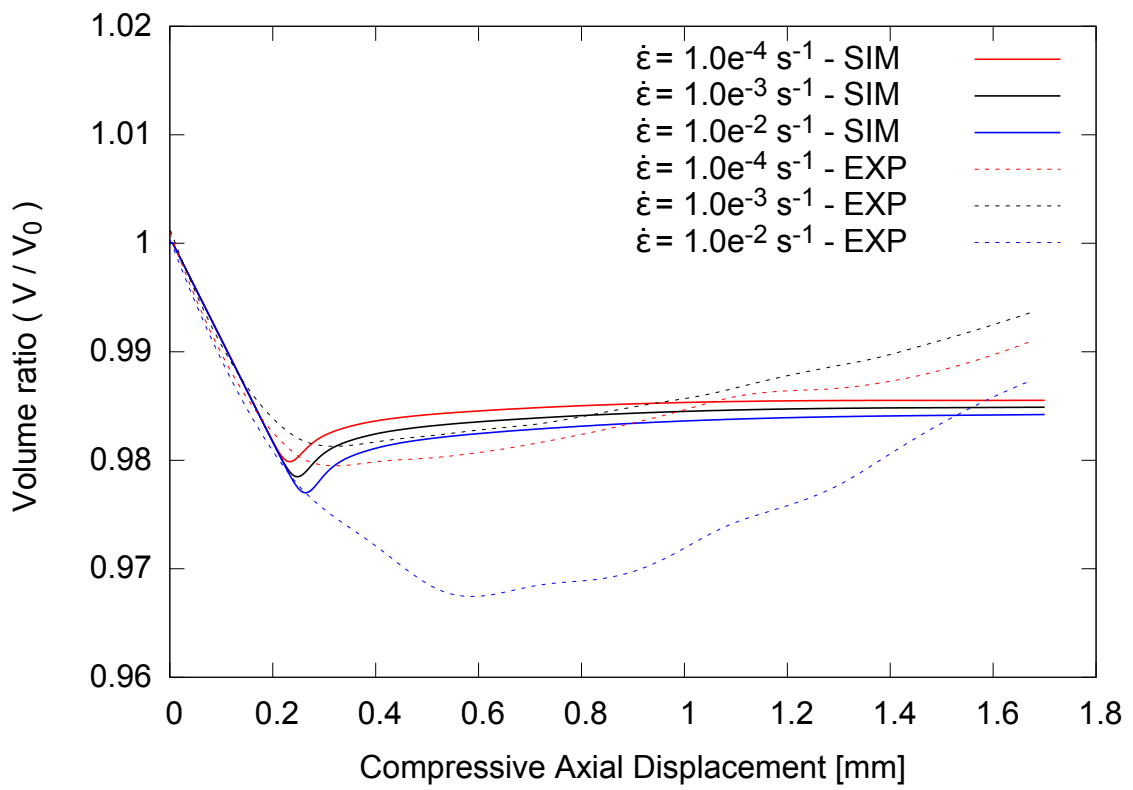


Figure 42 – Mixed-2 identification procedure - Farias model.

5.6 DISCUSSION

In regards to the obtained test data and the researched literature, it can be observed that material softening is a common behavior in polymeric materials. However, this phenomenon manifests itself with different intensities. For instance, a much more smooth softening is observed for PMMA (ARRUDA; BOYCE; JAYACHANDRAN, 1995) and EPON 862 (POULAIN; KOHLMAN, et al., 2013) under compression conditions than those found for PLGA 85:15. The continuous loss in resistance presented by the highest strain rate is not uncommon, a similar behavior can be observed for PC in high temperatures (AMES et al., 2009), which could be an indicative of thermo-mechanical effects.

The steep softening behavior is still the most troublesome to model and to perform the parameter identification procedure. The narrower the softening, the more are the numerical instabilities observed in calculating the constitutive models, leading simulations to fail prematurely. From the previous section it can be observed that the constitutive models were able to reproduce softening and hardening behavior appropriately while also following the transversal strain trend. All models slightly overestimated the transversal strain by at most 0.1 mm while showing low to no sensitivity to strain rate.

The more certainty one has on range of parameters, the narrower the search space can be, thus necessitating fewer particles on the PSO stage. A rather high number of particles was used in order to have a wide search space and to have more credibility in saying that a model can or cannot represent certain behaviors instead of just poor choice of search limits. In more practical situations, the time required to calculate the FE simulation for such a number of particles is prohibitively long. For this reason the homogeneous approach is a more reasonable approach with only marginal losses in the behavior of the final curve fitted. One major point of concern of the approach is that it tends to overestimate the hardening effects for larger strains. For materials that present higher rates of strain hardening or even for PLGA under higher levels of axial strain, where the geometric effects might play an major role, the two-stage approach would be recommended so that hardening levels could be readjusted.

FSF model presented a better agreement to experimental results while taking less time to compute and also having fewer parameters to identify. One advantage of the CF model is that in its current form the hydrolytic damage is already a part of this model, even though it was not considered here. The set of identified parameters presented here are considered a good foundation point to other experiments in order to find the degradation rate and mechanically coupled degradation rate.

The PSO-NM hybridization showed positive results, where the PSO algorithm was able to successfully escape the local minima that it encountered and handling faulty simulations whereas the NM algorithm hastened the identification process. The most reduction of the objective function value happened in the initial 4 to 5 iterations of the PSO. The reduction was low in the NM stage, possibly due to remaining in the PSO stage longer than it would be optimal. Thus, for better processing times, it is suggested that the PSO stage finishes earlier

by adopting a wider tolerance on the stopping criteria, for example.

It should be stated that better agreement to the stress curve could be found with the current models if that was the only curve being fitted, as many cases presented in the literature. It was verified that using both applied force and transversal displacement recovered the macroscopic behavior, while ignoring transversal behavior led to inconsistent macroscopic results. Yet, using only the mid-point transversal displacement was insufficient in order to retrieve the deformed volume. These two observations might indicate that the identification procedure as performed by Poulain2014 is not as applicable as previously thought. An interesting upgrade to the current procedure would be to minimize the distance of more points on the lateral surface, since they are already available, and check whether or not the models would be able to replicate the deformed surface and applied force simultaneously.

6 CONCLUSION

In this work the mechanical response of PLGA 85:15 under uniaxial non-homogeneous compression is presented. Data from samples subjected to compression under three different strain rates were employed. The compression force and the transversal strain, obtained through video monitoring were used as data source to parameter identification through an optimization framework. The FEM-based approach can be seen as the most commonly used approach in the literature for non-homogeneous identification conditions. However, this may not be very practical due to time costly simulations. Materials that display more complex behavior and have more parameters to identify might require even more time, thus the need for better identification approaches. Different assumptions on the stress field of the test specimens (homogeneous and non-homogeneous) led to four different identification approaches: FEM-based, Constitutive-based, Mixed-1 and Mixed-2 approaches. These approaches were tested using the CF model and FSF model, where sets of parameters are presented for the two models for each identification approach.

All identification approaches provided similar results with differences on where was the best fitted region (small strains region, softening region, large strains region), but in overall it is concluded that for the macroscopic behavior there is a low dependency on the choice of identification approach, even when significant barreling is present. The main difference between approaches lies on the time required to identify, where the constitutive-based and Mixed-1 showed to be the more efficient of the approaches.

Propositions for future works

As mentioned in the introduction, this work is part of first steps in characterizing PLGA 85:15, as well as other materials for medical applications. To continue this line of research the following works are proposed:

- Validate the identified parameters, considering different mechanical tests and applications.
- Verify the applicability of the constitutive-based and Mixed-1 approaches for other materials under non-homogeneous compression and under higher strains.
- Study the source of the secondary softening and verify whether or not this effect is due to heat generation in higher strain rates.
- Enhance the current material models to account for thermal effects.
- Test the material under other types of mechanical testings and use the results in the optimization procedure.
- Verify the impact on the set of identified parameters. How much do they differ from the results presented here?

- Test the hydrolytic degradation with and without loading and identify constitutive parameters for hydrolytic damage for PLGA 85:15.

REFERENCES

- ABDEL-WAHAB, Adel A.; ATAYA, Sabbah; SILBERSCHMIDT, Vadim V. Temperature-dependent mechanical behaviour of PMMA: Experimental analysis and modelling. **Polymer Testing**, Elsevier Ltd., n. 58, p. 86–95, 2016. DOI: 10.1016/j.energy.2017.02.174.
- AMES, Nicoli M. et al. A thermo-mechanically coupled theory for large deformations of amorphous polymers. Part II: Applications. **International Journal of Plasticity**, Elsevier, v. 25, n. 8, p. 1495–1539, 2009.
- ANAND, L.; AMES, N. M. On modeling the micro-indentation response of an amorphous polymer. **International Journal of Plasticity**, v. 22, n. 6, p. 1123–1170, 2006. ISSN 07496419. DOI: 10.1016/j.ijplas.2005.07.006.
- ARORA, Jasbir S. **Introduction to Optimum Design**. [S.l.]: Elsevier Science, 2004. ISBN 9780120641550. DOI: 10.1016/B978-0-12-064155-0.X5000-9.
- ARRUDA, Ellen M.; BOYCE, Mary C.; JAYACHANDRAN, R. Effects of strain rate, temperature and thermomechanical coupling on the finite strain deformation of glassy polymers. **Mechanics of Materials**, 1995. DOI: 10.1016/0167-6636(94)00034-E.
- ASTM INTERNATIONAL. **ASTM D695-15 - Standard Test Method for Compressive Properties of Rigid Plastics**. [S.l.], 2015.
- AVGOUSTAKIS, Konstantinos. Polylactic-co-glycolic acid (PLGA). **Encyclopedia of biomaterials and biomedical engineering**. Taylor & Francis, p. 1–11, 2005.
- CASTRO, Paulo Bastos de. **Modelo de dano dúctil-hidrolítico acoplado para materiais elasto-viscoplasticos baseado em atualizações constitutivas variacionais**. 2017. Tese de doutorado – POSMEC - Engenharia Mecânica, Universidade Federal de Santa Catarina, Brasil.
- CASTRO, Paulo Bastos de; FANCELLO, Eduardo Alberto. Coupled ductile–hydrolytic damage model based on variational constitutive updates. **Computer Methods in Applied Mechanics and Engineering**, Elsevier BV, v. 323, p. 202–229, Aug. 2017. DOI: 10.1016/j.cma.2017.05.023.

CASTRO, Paulo Bastos de; SALMORIA, Gean Vitor, et al. A study on the response of PLGA 85/15 under compression and heat treatment testing cycles. Unpublished. [S.l.], 2019.

ČERNÝ, V. Thermodynamical approach to the traveling salesman problem: An efficient simulation algorithm. **Journal of Optimization Theory and Applications**, v. 45, n. 1, p. 41–51, 1985. DOI: 10.1007/BF00940812.

DUPAIX, Rebecca B.; BOYCE, Mary C. Finite strain behavior of poly(ethylene terephthalate) (PET) and poly(ethylene terephthalate)-glycol (PETG). **Polymer**, 2005. ISSN 00323861. DOI: 10.1016/j.polymer.2005.03.083.

EBERHART, Russell; KENNEDY, James. New optimizer using particle swarm theory. In: PROCEEDINGS of the International Symposium on Micro Machine and Human Science. [S.l.: s.n.], 1995. p. 39–43. DOI: 10.1109/MHS.1995.494215.

FARIAS, Jan-Michel C.; STAINIER, Laurent; FANCELLO, Eduardo Alberto. A variational framework for the modeling of glassy polymers under finite strains. **Continuum Mechanics and Thermodynamics**, 2019. ISSN 0935-1175. DOI: 10.1007/s00161-019-00809-8.

FARIAS, Jan-Michel Colombo. **Resistência ao fluxo inelástico na modelagem de polímeros amorfos - Uma abordagem termodinâmica variacional**. 2018. Tese de doutorado – POSMEC - Engenharia Mecânica, Universidade Federal de Santa Catarina, Brasil.

FUCK, Vinicius Rios. **Modelo constitutivo de viscoelasticidade e dano aplicado a polímeros termoplásticos**. 2018. Master Dissertation – POSMEC - Engenharia Mecânica.

GENTILE, Piergiorgio et al. An Overview of Poly(lactic-co-glycolic) Acid (PLGA)-Based Biomaterials for Bone Tissue Engineering. **International Journal of Molecular Sciences**, 2014. ISSN 1422-0067. DOI: 10.3390/ijms15033640.

GSELL, C. et al. Video-controlled tensile testing of polymers and metals beyond the necking point. **Journal of Materials Science**, Springer, v. 27, n. 18, p. 5031–5039, 1992. DOI: 10.1007/bf01105270.

HANSEN, Nikolaus et al. Comparing Results of 31 Algorithms from the Black-box Optimization Benchmarking BBOB-2009. In: PROCEEDINGS of the 12th Annual Conference Companion on Genetic and Evolutionary Computation. Portland, Oregon, USA: ACM, 2010. (GECCO '10), p. 1689–1696. DOI: 10.1145/1830761.1830790.

HOLLAND, John H. **Adaptation in Natural and Artificial Systems: An Introductory Analysis with Applications to Biology, Control and Artificial Intelligence**. Cambridge, MA, USA: MIT Press, 1992. ISBN 0262082136.

JERABEK, M.; MAJOR, Z.; LANG, R. W. Uniaxial compression testing of polymeric materials. **Polymer Testing**, 2010. ISSN 01429418. DOI: 10.1016/j.polymertesting.2009.12.003.

KENNEDY, J.; EBERHART, R. Particle swarm optimization. In: PROCEEDINGS of ICNN'95 - International Conference on Neural Networks. [S.l.: s.n.], 1995. 1942–1948 vol.4. DOI: 10.1109/ICNN.1995.488968.

KIRKPATRICK, Scott; GELATT JR, D; P. VECCHI, Mario. Optimization by Simulated Annealing. **Science**, v. 220, p. 671–680, Jan. 1983. DOI: 10.1142/9789812799371_0035.

LI, Han et al. Identification of material properties using nanoindentation and surrogate modeling. **International Journal of Solids and Structures**, 2016. ISSN 00207683. DOI: 10.1016/j.ijsolstr.2015.11.022.

MELICK, H.G.H. van; GOVAERT, L.E.; MEIJER, H.E.H. Localisation phenomena in glassy polymers: influence of thermal and mechanical history. **Polymer - The International Journal for the Science and Technology of Polymers**, 2003. ISSN 0032-3861. DOI: 10.1016/S0032-3861(03)00089-2.

MELICK, H.G.H. van; GOVAERT, L.E.; MEIJER, H.E.H. On the origin of strain hardening in glassy polymers. **Polymer - The International Journal for the Science and Technology of Polymers**, 2003. ISSN 0032-3861. DOI: 10.1016/S0032-3861(03)00112-5.

MELICK, H.G.H. van; GOVAERT, L.E.; RASS, B., et al. Kinetics of ageing and re-embrittlement of mechanically rejuvenated polystyrene. **Polymer - The International Journal for the Science and Technology of Polymers**, 2003. ISSN 0032-3861. DOI: 10.1016/S0032-3861(03)00112-5.

MELO, Liliane Pimenta de et al. Effect of Injection Molding Melt Temperatures on PLGA Craniofacial Plate Properties during In Vitro Degradation. **International Journal of Biomaterials**, 2017. ISSN 1687-8787. DOI: 10.1155/2017/1256537.

MILLER, N D; WILLIAMS, D F. The in vivo and in vitro degradation of poly(glycolic acid) suture material as a function of applied strain. **Biomaterials**, v. 5, n. 6, p. 365–368, 1984. DOI: [http://dx.doi.org/10.1016/0142-9612\(84\)90037-1](http://dx.doi.org/10.1016/0142-9612(84)90037-1).

NELDER, J.A; MEAD, R. A simplex method for function minimization. **Computer Journal**, n. 7, p. 308–313, 1965.

ONG, Kevin L.; YUN, Brian Min; WHITE, Joshua B. New biomaterials for orthopedic implants. **Dove Press Journal: Orthopedic Research and Reviews**, 2015. DOI: ORR.S63437.

ORTIZ, M.; STAINIER, L. The variational formulation of viscoplastic constitutive updates. **Computer Methods in Applied Mechanics and Engineering**, 1999. ISSN 00457825. DOI: 10.1016/S0045-7825(98)00219-9.

POULAIN, X.; BENZERGA, A. A.; GOLDBERG, R. K. Finite-strain elasto-viscoplastic behavior of an epoxy resin: Experiments and modeling in the glassy regime. **International Journal of Plasticity**, 2014. DOI: 10.1016/j.ijplas.2014.07.002.

POULAIN, X.; KOHLMAN, L. W., et al. Determination of the intrinsic behavior of polymers using digital image correlation combined with video-monitored testing. **International Journal of Solids and Structures**, 2013. DOI: 10.1016/j.ijsolstr.2013.01.041.

REYNOLDS, Robert G. An introduction to cultural algorithms. In: WORLD SCIENTIFIC. PROCEEDINGS of the third annual conference on evolutionary programming. [S.l.: s.n.], 1994. p. 131–139.

SONNENHOHL, Armin. **Desenvolvimento e implementação de procedimentos experimentais para caracterização mecânica de polímeros termoplásticos. Estudo de Caso: UHMWPE**. 2015. Master Thesis – Universidade Federal de Santa Catarina. <https://repositorio.ufsc.br/xmlui/handle/123456789/169332>.

TARANTOLA, A. **Inverse Problem Theory and Methods for Model Parameter Estimation**. [S.l.]: Society for Industrial and Applied Mathematics, 2005. (Other titles in applied mathematics). ISBN 9780898715729.

VAZ JR., M. et al. Identification of constitutive parameters - optimization strategies and applications. **Materialwissenschaft und Werkstofftechnik**, Wiley-VCH Verlag GmbH, n. 46, p. 4–5, 2015. DOI: 10.1002/maWe.201500423.

WANG, X. et al. Inverse finite element modeling of the barreling effect on experimental stress-strain curve for high temperature steel compression test. **Journal of Materials Processing Technology**, 2017. DOI: 10.1016/j.jmatprotec.2017.01.012.

ZHOU, Aimin et al. Multiobjective evolutionary algorithms: A survey of the state of the art. **Swarm and Evolutionary Computation**, Elsevier B.V., n. 1, p. 32–49, 2015. DOI: 10.1016/j.swevo.2011.03.001.